

NATIONAL UNIVERSITY OF IRELAND MAYNOOTH



Machine Learning for the Automatic Classification of Radio Spectra

Author: Elizabeth O'Dwyer

*A thesis submitted in fulfillment of the requirements
for the degree of Research Masters
in the*

Department of Mathematics and Statistics

*Carried out in coordination with the
School of Cosmic Physics,
Dublin Institute of Advanced Studies.*

October 2023

Head of Department

Prof. Stephen Buckley

Supervisor:

Dr. Katarina Domijan

External Supervisor:

Prof. Caitriona Jackman

This thesis has been prepared in accordance with the PhD regulations of Maynooth University and is subject to copyright.
For more information see PhD Regulations (December 2022).

Acknowledgements

I would like to thank my supervisors, Caitriona and Katarina. You were an amazing support throughout the project and I surprised myself with how much I could achieve in the last two years, largely in thanks to your expertise and guidance. It's been a great pleasure to work with you both. I'd like to thank the Planetary Magnetospheres group in DIAS, it's been wonderful to work with a group so talented and knowledgeable, as well as kind and full of good humour. I would like to acknowledge how important my friends and family have been during this time, thank you for all of the support, advice and a well needed respite from the hard work. I'd also like to thank my partner Conor for bringing me so much joy and encouragement in both the happier and more difficult periods over the last few years.

Contents

Acknowledgements	iii
Abstract	vii
List of Publications	viii
0.1 Introduction	1
0.2 Chapter I	4
0.3 Chapter II	21
0.4 Chapter III	40
0.5 Chapter IV	55
0.6 Chapter V	66
0.7 Code	75
0.8 Datasets	76
0.9 Conclusion	77
Bibliography	81

Abstract

Department of Mathematics and Statistics

Research Masters

Machine Learning for the Automatic Classification of Radio Spectra

by Elizabeth O'DWYER

SKR is a non-thermal, auroral emission with peak emission occurring at 100-400 kHz. Its properties have been extensively studied since Cassini's arrival at Saturn until mission end with its Radio and Plasma Wave Science (RPWS) experiment. Low Frequency Extensions (LFEs) of SKR, which consist of global intensifications of SKR accompanied by extensions of the main SKR band down to lower frequencies have been studied in particular. LFEs result from internally-driven tail reconnection and from solar wind compressions of the magnetosphere, which also trigger tail reconnection. They have been previously identified with two approaches: through visual inspection and using an intensity threshold for LFEs occurring in 2006 (Reed et al., 2018). In this work, we describe the method used to develop a visual criterion for LFE selection, and use this method to select a sample of LFEs detected by Cassini/RPWS by fitting their exact frequency-time coordinates with polygons. We use this sample of LFEs as a training set for an image-based machine learning algorithm to classify all LFEs detected by Cassini/RPWS. The inputs to the model are multi-channel images consisting of spectrogram images in flux density and degree of circular polarisation. The outputs of the model are binary masks showing the exact location of the LFE in frequency-time space. The median IoU (Intersection Over Union) across the testing and training set were calculated to be 0.97 and 0.98 respectively. 4874 LFEs were detected using this method and the catalogue in the form of frequency-time coordinates is available for use amongst the scientific community.

List of Publications

1. O'Dwyer, E. P., Jackman, C. M., Domijan, K., Lamy, L., & Louis, C. K. (2023). A Selection of Low Frequency Extensions of Saturn Kilometric Radiation., In C. K. Louis, C. M. Jackman, G. Fischer, A. H. Sulaiman, P. Zucca, Dublin Institute for Advanced Studies (Eds.), *Planetary, Solar and Heliospheric Radio Emissions IX*.
doi: <https://doi.org/10.25546/103103>
2. O'Dwyer, E. P., Jackman, C. M., Domijan, K. & Lamy, L. (2023). Image-Based Classification of Intense Radio Bursts from Spectrograms: An Application to Saturn Kilometric Radiation., *Journal of Geophysical Research: Space Physics*, 128, e2023JA031926.
<https://doi.org/10.1029/2023JA031926>
3. Jackman, C. M., O'Dwyer, E. P., Louis, C. K., Fogg, A. R., Waters, J. E., Lamy, L., Using crossings of Saturn's magnetospheric boundaries to explore the link between upstream conditions and radio emission., In C. K. Louis, C. M. Jackman, G. Fischer, A. H. Sulaiman, P. Zucca, Dublin Institute for Advanced Studies (Eds.), *Planetary, Solar and Heliospheric Radio Emissions IX, 2023*.
<https://doi.org/10.25546/103100>
4. Wu, S. Y., Ye, S. Y., Fischer, G., Taubenschuss, U., Jackman, C. M., O'Dwyer, E., et al. (2022). Saturn Anomalous Myriametric radiation, a new type of Saturn radio emission revealed by Cassini. *Geophysical Research Letters*, 49, e2022GL099237.
<https://doi.org/10.1029/2022GL099237>
5. Louis, C.K, Jackman C.M., Mangham S., Smith K., O'Dwyer, E., Empey A., Cecconi B., Boudouma A., Zarka P. & Maloney S. (2022). The "SPectrogram Analysis and Cataloguing Environment" (SPACE) Labelling Tool., *Frontiers in Astronomy and Space Science*, 9, doi: 10.3389/fspas.2022.1001166

0.1 Introduction

In this thesis, we present work carried out on the topic of ‘Machine Learning for the Automatic Classification of Radio Spectra’. The aim of this work was to develop a technique for successfully classifying specific features of radio emission that can be viewed on spectrograms, which are frequency-time plots that allow for the visual inspection of a radio signal over time. The techniques discussed in this thesis are applicable to radio emission generated by an array of sources, however we have solely focused on the application to strongest element of Saturn’s radio emission, Saturn Kilometric Radiation (SKR). SKR is a non-thermal, auroral radio emission whose properties have been extensively studied.

The major dataset employed in this study was collected by the RPWS instrument aboard the Cassini spacecraft. The Cassini mission had a range of scientific goals, one of which was to study the radio emission emitted at Saturn’s magnetosphere. The RPWS high frequency receiver measured the wave electric field along three electric monopole antennas over the frequency range of 3.5 kHz to 16 MHz. The HFR computed auto- and cross-correlations of the antenna signals, and subsequently the Stokes parameters (flux and polarization) can be calculated by performing goniopolarimetric (direction-finding) inversions (Cecconi and Zarka, 2005). The RPWS instrument detected a range of radio emissions such as SKR, Saturn’s narrowbanded emissions, radio bursts from the sun e.g. solar type III bursts and also radio frequency interference. In this thesis, we use RPWS data that has been processed to preserve only Saturn’s radio emissions according to Lamy et al. (2008b) and can be found at (Lamy, Cecconi, and Zarka, 2009).

SKR is the most powerful of Saturn’s radio emission and has been observed by numerous spacecraft since its initial observation by the Voyager Planetary Radio Astronomy (PRA) instrument in the early 1980s (Kaiser et al., 1980). Following this, the Unified Radio and Plasma Wave (URAP) instrument aboard Ulysses spacecraft made occasional observations of SKR (Galopeau and Lecacheux, 2000). With the arrival of the Cassini spacecraft to Saturn in mid-2004, the RPWS instrument was observing SKR quasi-continuously until mission end in late 2017. The properties of SKR are well known thanks to the success of the Cassini mission. SKR occurs in the range of a few kHz to 1.2 MHz (Kaiser and

Desch, 1984; Lamy, 2017, and references therein). Peak emission occurs in the range of 100-400 kHz (Lamy et al., 2008b). SKR is generated by the cyclotron maser instability (CMI) (Wu and Lee, 1979), radio waves are generated at frequencies close to the local electron gyrofrequency f_{ce} by electrons that are accelerated along field lines in auroral zones. As $f_{ce} = qB/(2\pi m)$, where q is the electron charge, B is the local magnetic field strength, and m is the electron mass, the frequency of the radio emission is directly proportional to the local magnetic field strength and inversely proportional to the distance from the planets centre. SKR is fully elliptically polarised, waves propagate mainly in the Right-handed extraordinary (R-X) mode. As a result, right-handed and left-handed emissions can be sourced back to the southern and northern hemispheres respectively. SKR is radiated along a thin, hollow cone which results in strong visibility effects (Lamy, Waters, and Louis, 2023, e.g.). On occasion, SKR intensifies and extends to upper and in particular lower frequencies. These events are termed Low Frequency Extensions (LFEs) (Bunce et al., 2005; Jackman et al., 2009; Reed et al., 2018). Equivalent radio signatures have been observed at the Earth (Morioka et al., 2008), which have been used as a diagnostic of magnetospheric dynamics, in particular linking to magnetotail reconnection and substorm activity. LFEs of SKR at Saturn have been associated with solar wind compression-induced dynamics and global reconfigurations of the magnetosphere, resulting in increased precipitation of energetic particles into auroral regions.

Previously LFEs had been selected by eye and using a numerical criterion based on an intensity threshold in distinct frequency ranges (Reed et al., 2018). Due to the reasonably large breadth of the Cassini radio dataset, we suggest using a machine learning (ML) approach based on a manually labelled training set to systematically classify the LFEs that were observed by the Cassini RPWS instrument. The visibility effects associated with SKR are further reason to employ an ML approach, it is difficult to account for visibility effects with solely a numerical criterion. An image based ML approach was employed due to the fact that SKR is typically viewed on a spectrogram, which can be considered akin to an image. Image based deep learning algorithms are typically convolutional neural networks (CNNs). CNNs are composed of convolutional layers, which consist of a collection of filters that convolve over the input and return the output feature map. CNNs have been used with great success for tasks such as instance segmentation

and semantic segmentation (Long, Shelhamer, and Darrell, 2015; Ren et al., 2015; He et al., 2017). The Unet algorithm (Ronneberger, Fischer, and Brox, 2015) is a fully convolutional neural network that applies semantic segmentation to its inputs. It was originally designed for segmenting biomedical images but it has been applied to a wide range of other tasks. It is particularly useful as it has been designed to perform classifications to a high degree of accuracy with a small training set. In this thesis, we include our contribution to scientific articles with focus on the study of SKR and other planetary radio emissions, and in particular the automatic classification of LFEs of SKR using ML methods. Chapters I and II include the major works by the author, whereas chapters III-V consist of scientific studies on the topic of planetary radio emissions that the author has contributed.

0.2 Chapter I

This chapter consists of an article published in Planetary, Solar and Heliospheric Radio Emissions IX conference proceedings. The article is titled 'Selection of Low Frequency Extensions of Saturn Kilometric Radiation'. I was the first-author of this article. My contribution was developing the visual criterion for LFE selection with the help of discussion with my co-authors, in particular my supervisors, the manual labelling of LFEs and the writing and producing of figures present in the article.

SELECTION OF LOW FREQUENCY EXTENSIONS OF SATURN KILOMETRIC RADIATION.

E.P. O'Dwyer^{1,2}, C. M. Jackman¹, K. Domijan²,
L. Lamy^{3,4} and C. K. Louis¹

Abstract

Saturn's Kilometric Radiation is an auroral emission that occurs between a few kHz to 1.2 MHz, and peaks in the frequency range 100-400 kHz (Kaiser et al., 1984). It was detected quasi-continuously by Cassini from its arrival at Saturn in 2004 until mission end in 2017 and its properties have been extensively studied. SKR bursts which are global intensifications of SKR as well as extensions of the main SKR band down to lower frequencies, known as Low Frequency Extensions (LFEs), result from internally-driven tail reconnection and from solar wind compressions of the magnetosphere, which also trigger tail reconnection. So far, LFEs had been identified by eye and also using a numerical criterion based on an intensity threshold (Reed et al., 2018). We present a sample of the LFEs detected by Cassini selected using the polygon selector tool by Louis et al. (2022a). LFEs were selected from a diverse range of spacecraft locations across the mission. 984 LFEs were selected in total and were then each categorized into 6 possible classes. The list of selected LFEs can be used for a wide range of applications, the principal one being as a training set for a machine learning approach to classify the remaining LFEs present in the Cassini/RPWS dataset. The list could also be used as a basis for case studies and as context for other activity.

1 Introduction

Saturn Kilometric Radiation is a powerful non-thermal radio emission radiated from Saturn's auroral regions at frequencies of a few kHz to 1.2 MHz, with peak emission occurring

¹*School of Cosmic Physics, DIAS Dunsink Observatory, Dublin Institute for Advanced Studies, Dublin 15, Dublin, Ireland.*

²*Department of Mathematics and Statistics, Maynooth University, Maynooth, Co Kildare, Maynooth, Ireland.*

³*LESIA, Observatoire de Paris, CNRS, Université PSL, Sorbonne Université, Université Paris Cité, CNRS, Meudon, France.*

⁴*Aix-Marseille Université, CNRS, CNES, LAM, Marseille, France.*

in the range of 100-400 kHz (Kaiser & Desch, 1984; Lamy et al., 2008). It was initially detected by the Voyager 1 mission in 1980 and has since been detected by Voyager 2, Ulysses and more recently Cassini (Kaiser et al., 1980; Galopeau & Lecacheux, 2000; Gurnett et al., 2005; Lamy, 2017). SKR draws parallels with Auroral Kilometric Radiation (AKR) generated at Earth. SKR is generated near the local electron gyrofrequency (f_c) by the Cyclotron Maser Instability (CMI), whereby electrons are accelerated along field lines in auroral zones (Wu & Lee, 1979; Lamy et al., 2018; Mutel et al., 2010; Menietti et al., 2011). Since $f_c = qB/(2\pi m)$, where q is the electron charge, B is the local magnetic field strength, and m is the electron mass, frequency is directly proportional to the local magnetic field strength and so inversely proportional to the cube of the distance of the source from the planets centre ($1/R^3$). SKR is beamed anisotropically and as a result is subject to strong visibility effects, specifically an ‘equatorial shadow zone’ predicted to occur up to $\sim 4 R_S$ for frequencies in the range of 200-400 kHz and up to $\sim 6-7 R_S$ ($R_S = 60268$ km) for frequency values of 80 and 900 kHz (Lamy et al., 2008). Lamy et al. (2008) also observed an extinction in emission detected at high latitudes as a result of a visibility effect (see figure 3 of Lamy et al. (2008)).

SKR dynamics have been shown to be governed by drivers both internal and external to the magnetosphere. Desch (1982) found that SKR activity is directly correlated with solar wind variations at Saturn. Desch & Rucker (1983) found that solar wind ram pressure variations specifically out of 13 solar wind qualities correlate the most strongly with fluctuations in SKR power. With Cassini’s arrival at Saturn in 2004, these relationships have been further explored with SKR bursts associated with solar wind compressions (Jackman et al., 2005) and compression induced tail reconnection (Bunce et al., 2005). Taubenschuss et al. (2006) used Linear Prediction Theory to investigate the impact of quantities such as solar wind bulk velocity, solar wind ram pressure, magnetic field strength of the interplanetary magnetic field (IMF) and the y-component of the IMF, with each exhibiting similarly strong effects as a driver but for different lag times.

Low Frequency Extensions (LFEs) of SKR correspond to extensions of the SKR spectrum beyond the main frequency band of SKR, with a particularly significant expansion down to lower frequencies. The main frequency band of SKR refers to the frequency range of peak emission, at 100-400 kHz. The frequency extension is associated with the extension of the radio source along field lines to higher altitudes, this results in lower frequency emission due to the direct relationship between magnetic field strength and frequency (Jackman et al., 2009). Morioka et al. (2008) has shown that low frequency extensions of AKR can be used as an indication of substorm onset at Earth. SKR LFEs have been similarly used at Saturn to diagnose tail reconnection (Jackman et al., 2009). Reed et al. (2018) used a semi-automated method for selection of LFEs detected by Cassini in 2006 based on intensity thresholds in the 40-100 kHz frequency band and the 100-600 kHz frequency band. The LFEs found were separated into long (>20 hours) and short (<20 hours). Reed et al. (2018) suggested that long LFEs result from solar wind compressions of the magnetosphere and short LFEs from internally-driven tail reconnection.

The motivation for this study is to build up a fully automated method to track all LFEs

70 present in Cassini/RPWS observations. This will allow us to perform statistical studies
71 which confirm/extend previous results obtained on a limited dataset and disentangle more
72 precisely the role of internal and external drivers: whether long LFEs are linked to solar
73 wind compressions of the magnetosphere (Bunce et al., 2005, 2010; Clarke et al., 2009;
74 Desch & Rucker, 1983; Kurth et al., 2005, 2016), are shorter LFEs driven by planetary
75 period oscillations (PPOs) (Carbary & Mitchell, 2013; Jackman et al., 2009; Lamy et al.,
76 2013) and also what is their recurrence rate and distribution of duration. This will also
77 allow us to examine the distinct shapes of each LFE in order to study the time evolution
78 from SKR burst to LFE allowing us to disentangle the physical evolution of the source.
79 The Cassini radio dataset is rich, quasi-continuous and spanning 13 years, making it un-
80 suitable for manual inspection. We thus propose the sample of LFEs selected in this study
81 as a basis for a supervised machine learning approach. In section 2 below we introduce
82 the Cassini/RPWS dataset, in section 3 we describe the methods for selecting the LFEs,
83 in section 4 we discuss the different LFE classifications and their spatial distribution, in
84 section 5 we list the possible applications and then present our conclusions in section 6.

85

86 2 Data

87 In this paper, we are using data from the Cassini Radio and Plasma Wave Science High
88 Frequency Receiver (RPWS HFR, Gurnett et al., 2004). This instrument measured the
89 wave electric field along three electric monopole antennas over the frequency range of 3.5
90 kHz to 16 MHz. The HFR computed auto- and cross-correlations of the antenna signals,
91 and subsequently the Stokes parameters (flux and polarization) can be calculated by per-
92 forming goniopolarimetric (direction-finding) inversions (Cecconi & Zarka, 2005).

93 The data was processed according to Lamy et al. (2008) resulting in a calibrated, homo-
94 geneous time series of flux density ($\text{W} \cdot \text{m}^{-2} \cdot \text{Hz}^{-1}$) normalized to 1 Astronomical Unit
95 (AU)) and degree of circular polarization for each frequency channel. There are 48 fre-
96 quency channels, sampling in the range of 3.5 kHz to 1500 kHz at a temporal resolution of
97 180 s. The first 24 frequency channels are logarithmically spaced (with $\Delta f/f=20\%$), and
98 the subsequent 24 are linearly spaced (with $\Delta f=50$ kHz). Lamy et al. (2008) processed
99 the data such that solely Saturn's emissions in the kilometer range are extracted. Solar
100 type III bursts and radio frequency interference (RFI) otherwise present in the raw data
101 was removed. The dataset can be found at Lamy et al. (2009). We have also used a list
102 containing manually selected time periods of erroneous sign of circular polarization in our
103 study, which occur when the 2-antenna plane is coming close to the wave direction of
104 arrival. We used this to note when the sign of circular polarization is unreliable. This list
105 was supplied by the Cassini/RPWS group at LESIA.

106

107 3 LFE selection methods: Polygon Selection

108 As part of our aim to label a diverse set of LFEs from across the Cassini mission, we
109 employed a manual labelling tool. This tool allowed us to interactively click and draw

polygons around the vertices of the LFE on a frequency-time spectrogram (Louis et al., 2022a; Louis et al., 2022b). This has been done for Jupiter by Marques et al. (2017) to catalog long-term observations of its decametric emissions observed by the Nançay Decameter array (Boischot et al., 1980) and by Louis et al. (2021) to catalog all Jovian radio components observed by the Waves instrument aboard Juno spacecraft in its first three years of mission (Kurth et al., 2017). Louis et al. (2023) also catalogued AKR detected by the Polar spacecraft for a portion of its mission (Gurnett et al., 1995). The polygon selector tool allows us to display flux density and degree of circular polarization at once for a given time range and frequency range allowing for polygon selection on multiple panels. The polygon selection tool is a user friendly tool and easily applicable to different radio datasets. Since the radio data used in this case has a non-monotonic bin structure, upon first use the tool will automatically rescale the frequency data to a user-defined number of bins between the minimum and maximum frequency value. The time resolution can also be rescaled to a user defined resolution. The rescaling process and henceforth loading in data and plotting previously labelled polygons takes seconds in each case. After processing is completed, the estimated time it took to complete a weeks worth of labelling would be on average 1hr. We labelled what we deemed to be a sufficient amount of data such that our list: encompasses a diverse range of spacecraft locations, includes LFEs of several different categories (see Table 1), and covers a broad time span throughout the Cassini mission.

In order to ensure stability and consistency across the LFE labels, we defined a set of visual criteria for the LFEs:

- a minimum frequency excursion down to 40 kHz, i.e. a requirement that the main band SKR extends down to values of 40 kHz or lower. We used Fig. 8a-c from a study by Lamy et al. (2008) as a justification for this choice, as they show that 40 kHz is close to the FWHM (in log-scale) frequency (for emission viewed from lower latitudes). The frequency spectrum of Saturn's radio emissions is more flat when viewed from higher latitudes but we retain this 40 kHz criterion throughout for consistency. This 40 kHz value also ensures the LFE is clearly distinct from more frequency-restricted SKR bursts, while also not extending too far down to overlap with the frequency range where caterpillars (Fischer et al., 2023) and narrowband emissions (Ye et al., 2010; Wang et al., 2010; Wu et al., 2021) are typically present.
- significant intensification above background. We achieve this parameterisation through the use of dynamic colour bars based on statistics of radio viewing, and by drawing the polygons around the upper ranges of these normalised intensities (see the paragraph below).
- LFEs are occasionally part of a broader SKR burst, where the main SKR band is intensified first, followed by an enhancement in the lower frequency bands. The LFE definition is based primarily off the excitation of emission below 100 kHz, but for examples where the 100-400 kHz range was excited first, we label the entire interval of intensified radio emission. Examples of such bursts at Earth were presented by Morioka et al. (2008).

- 153 • continuous emission with respect to frequency i.e. no frequency gaps. This corre-
154 sponds to a broad extension in altitude of the radio sources.
- 155 • focus on labelling emission above a lower limit of 10 kHz, this is a guideline rather
156 than a strict cut-off. This was to avoid erroneously including many of the complex
157 non-CMI-generated emissions at the lower part of the spectrum (such as narrow-
158 band near 5 kHz and 20 kHz (Gurnett et al., 1981; Lamy et al., 2008), or Saturn’s
159 caterpillars (Fischer et al., 2023).

160 Based on the known visibility effect of SKR in relation to the position of the observer
161 (Lamy et al., 2008), we decided to adjust the limits of the colorbar of the dynamic spec-
162 trum according to the spacecraft location. We first separated all of the radio data into two
163 latitude ranges: $\lambda_{s/c} < |5^\circ|$ and $\lambda_{s/c} > |5^\circ|$ where $\lambda_{s/c}$ is the spacecraft latitude. We then
164 further separated these two subsets of the radio data into 1 hr long local time bins. We
165 were then able to take the median spacecraft latitude in the time range of the dynamic
166 spectrum and the local time range of the spacecraft in the time range of the dynamic
167 spectrum, and found the 10th and 80th percentile of all of the data observed from this
168 latitude and local time range. We used these percentiles as the limits of the colorbar on
169 the given dynamic spectrum. This allows us to account for the intensity dependence on
170 local time and latitude. We used a time period of two days when labelling on the dynamic
171 spectrum, this was chosen by-eye as a reasonable time range for selecting the full shape
172 of LFEs of longer duration (e.g. > 30 hours) whilst conserving sufficient resolution to
173 accurately label LFEs of shorter duration (e.g. < 3 hours). Note that we neglected the
174 effect of radial distance in this study for simplicity. Polygons were drawn around patches
175 of emission where the majority of intensity values were at the upper limit of the colorbar
176 on the given dynamic spectrum. This does allow for some portion of labelled LFEs to
177 have moderate intensities (e.g. green $10^{-21} \text{Wm}^{-2} \text{Hz}^{-1}$) but the bulk of the emission must
178 be at the top of the range. We would like to note the importance of using a colorbar that
179 adheres to the guidelines defined in Cramer et al. (2020) to accurately represent data
180 visualisations and to be accessible to people with colour-vision deficiencies. We made use
181 of a sequential perceptually uniform colormap in order to do this.

182

183 We labelled a subset of the entire dataset: this included the entirety of 2006, several
184 months in 2008 and small sample of data from all years (2004-2017) with the exception
185 of 2015. In total 984 LFEs were found and labelled using the polygon selection tool.
186 2006 was chosen as it allows for blind cross comparison with the catalogue produced by
187 Reed et al. (2018). Note that in 2006 Cassini spent the majority of the time at equatorial
188 latitudes, passed through all local times and reached distances of $> 68 R_S$ down Saturn’s
189 magnetotail. In 2008, Cassini is much closer to the planet ($< 40 R_S$) but is mostly at
190 higher latitudes ($> 50^\circ$ Latitude). Orbit duration was shorter, and associated rate of
191 passage through different viewing regions was quicker than in 2006. Thus 2008 was se-
192 lected for its variation in viewing in comparison to 2006, with respect to radial distance
193 and latitude. We also include a sample of LFEs from all years of the mission (with the
194 exception of 2015) which were selected for the purpose of other studies (Wu et al., 2022;
195 Jackman et al., 2023). An example of several labelled polygons are shown in figure 1,

196 a two panel plot showing flux density normalised to 1 AU in $\text{Wm}^{-2}\text{Hz}^{-1}$ and degree of
 197 circular polarization with labelled polygons indicated in orange. We used the sections of
 198 fully labelled data (in 2006 and 2008) to note the periods of time where it is confirmed
 199 that we do not see an LFE. We noted 980 five hour time periods of the data in 2006 and
 200 2008 where we do not see an LFE. These 5 hour periods could consist of SKR without a
 201 LFE, narrowband near 5 kHz and 20 kHz or no emission at all.

202

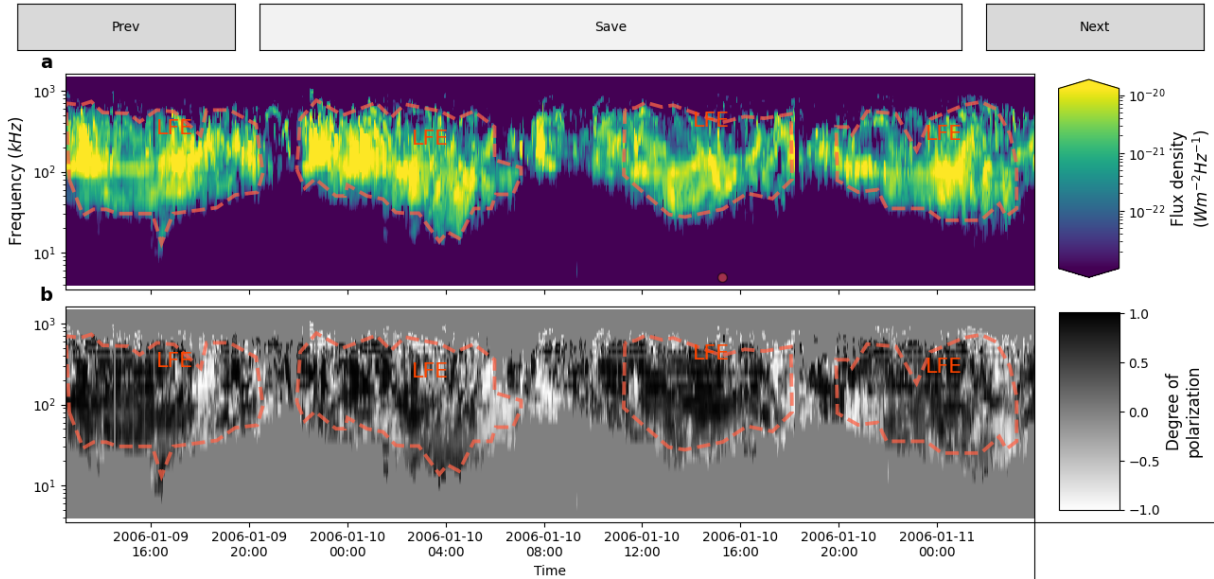


Figure 1: Two panel plot showing an example of the selection of four LFEs using the polygon selector tool (Louis et al., 2022a). In panel (a), we see Cassini RPWS dynamic spectrum with a colorbar showing flux density normalised to 1 AU and panel (b) is showing another Cassini RPWS dynamic spectrum for the same time period with a colorbar showing degree of circular polarization. LFEs are indicated by polygons drawn with a dotted orange line.

203 4 Results

204 4.1 LFE labelled examples: Statistics and Classes

205 The varied appearance of LFEs quickly became evident throughout the labelling process.
 206 It was useful to further divide the LFEs into subcategories. This allows for a diverse sam-
 207 ple that is more representative of the full dataset. As mentioned above, SKR visibility is
 208 strongly dependent on spacecraft location and depending on Cassini's location, the LFE
 209 appearance is variable. In table 1, a description of each class is listed along with their total
 210 count. 6 different classes were identified. The first class 'LFE', is defined as the typical
 211 appearance of an LFE i.e. a continuous extension of intensified emission from the main
 212 band SKR down to at least 40 kHz or lower. Examples of such events have been discussed
 213 in e.g. Jackman et al. (2009). 'LFE_m' (for 'massive') differs from 'LFE' in the fact that
 214 its duration consists of a single planetary period (~ 11 hours) or longer. The subscript 'm'

215 comes from ‘massive’ due to its increased time duration. Reed et al. (2018); Bradley et al.
 216 (2020) discuss these events as seen during periods of intense magnetospheric disturbance.
 217 ‘LFE_{sp}’ (for ‘sparse’) is defined as an extension of intensified emission from the main band
 218 SKR down to at least 40 kHz or lower. However the intensity may vary throughout the
 219 frequency excursion, i.e. some frequency channels do not display intensified emission. The
 220 emission has a sparse appearance, although most of the emission occurring throughout
 221 the LFE is intensified. ‘LFE_{sm}’ (for ‘small’) is defined as a continuous extension of inten-
 222 sified emission from the main band SKR down to frequencies below the main band but
 223 greater than 40 kHz. The ‘LFE_{sm}’ class is not any strong emission below 100kHz, it is
 224 an intermediate extension between the main band and the minimum threshold of 40kHz.
 225 It has intense emission down to at least ~ 70 kHz but not as low as 40kHz. We use the
 226 subscript ‘sm’ coming from ‘small’ due to its reduced extension in frequency. ‘LFE_{dg}’ (for
 227 ‘datagap’) is defined as an LFE with a datagap during its occurrence (defining a datagap
 228 as a full gap in emission over multiple consecutive time steps). The datagap may cut short
 229 the LFE, i.e. occurring at the beginning or end. ‘LFE_{ext}’ (for ‘extinction’) is defined as a
 230 continuous extension of intensified SKR down to frequencies of 40 kHz or lower, however
 231 there is an extinction of the main band of SKR. This could be a complete or partial lack
 232 of emission of the main band of SKR. It differs from the ‘LFE_{sp}’ class in the fact that it
 233 is a lack of emission solely in the higher frequency portion, rather than sparse emission
 234 throughout the whole LFE. This occurs due to a viewing effect as mentioned by Lamy
 235 et al. (2008) when the observer is at high latitudes. In figure 2, an example of each LFE
 236 class is shown with 2-panel plots displaying dynamic spectra of flux density normalised
 237 to 1 AU and degree of circular polarization with the labelled LFE indicated by black and
 238 blue polygons respectively. In table 2, the yearly number of labelled LFEs and periods
 239 confirmed to not have an LFE are shown.

240

Type	Count	Description
LFE	479	Standard appearance
LFE _m	96	LFEs longer than a single planetary rotation
LFE _{sp}	99	LFE with sparse emission
LFE _{sm}	164	LFE that is of intermediate extension, excursion to > 40 kHz but < 100 kHz.
LFE _{dg}	111	LFE with a datagap
LFE _{ext}	35	LFE with extinction at high frequencies

Table 1: Distribution of LFE categories within labelled data.

Year	LFE	LFE _{dg}	LFE _{ext}	LFE _m	LFE _{sm}	LFE _{sp}	NoLFE
2004	9	0	0	5	6	0	-
2005	1	4	0	5	0	1	-
2006	277	65	4	44	94	46	766
2007	44	9	4	5	24	1	-
2008	46	22	13	19	16	25	214
2009	6	4	3	2	0	4	-
2010	2	0	0	0	2	0	-
2011	22	1	0	1	2	2	-
2012	14	1	0	3	2	2	-
2013	19	2	2	5	4	4	-
2014	2	0	2	4	7	4	-
2015	-	-	-	-	-	-	-
2016	23	1	3	1	7	9	-
2017	14	2	4	2	0	1	-
Total	479	111	35	96	164	99	980

Table 2: Labelled data by year. The LFE category is further split into different classes.

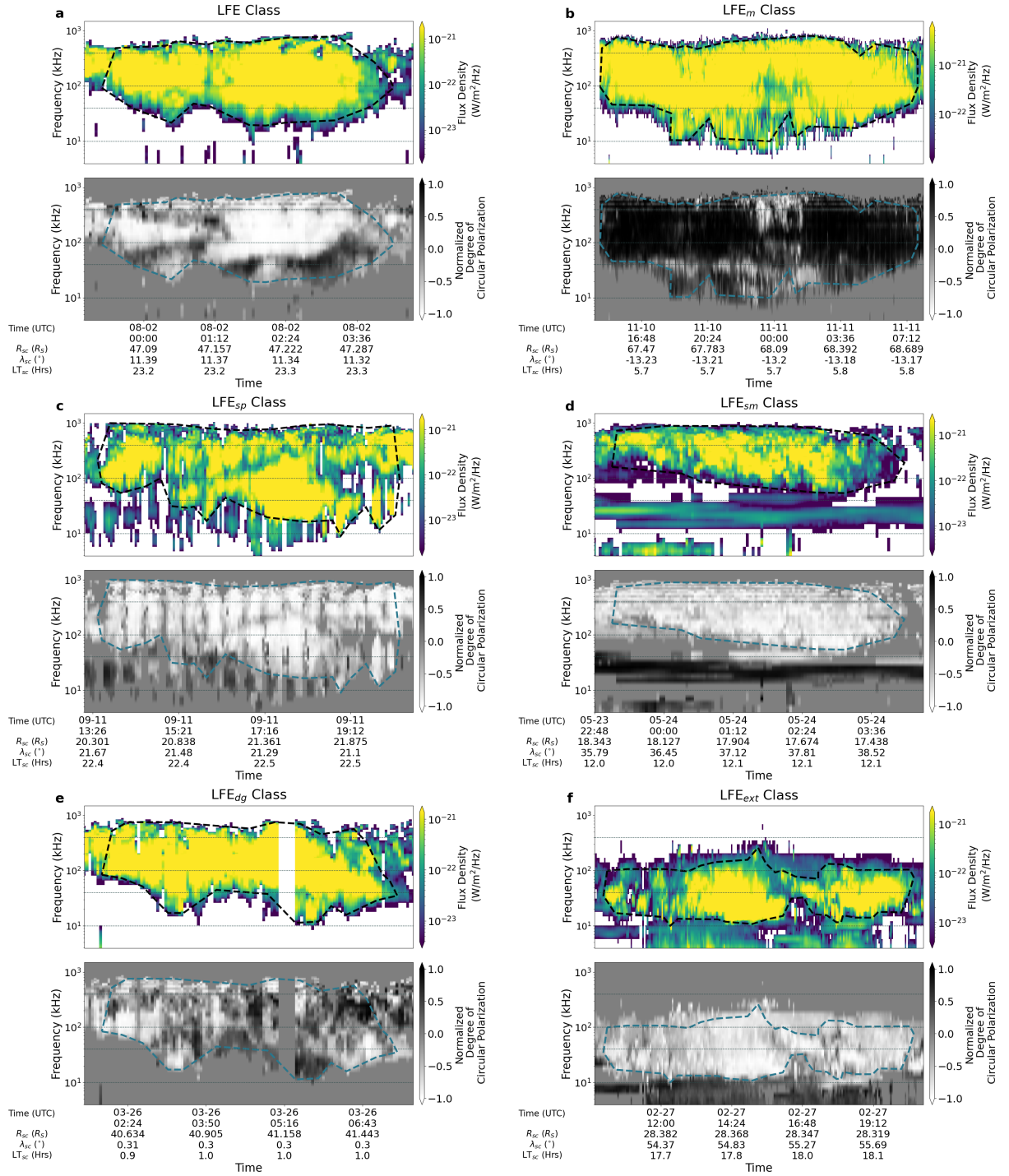


Figure 2: Examples of each class of LFE shown on 6 2-panel Cassini RPWS dynamic spectra with flux density normalised to 1 AU shown on the upper panel and degree of circular polarization on the lower panel. Polygon selection of LFEs are indicated in black and blue respectively for each panel.

241 4.2 Spatial distribution

242 Figure 3 is a 5-panel plot describing Cassini's trajectory and the location of labelled peri-
 243 ods of emission. The spacecraft ephemeris data originated from the Cassini Magnetometer
 244 instrument, which was calibrated and averaged to a resolution of 1 minute (Dougherty
 245 et al., 2004, 2019). Panels (a) and (b) show the spacecraft coverage (grey trace) in the
 246 X-Y plane and X-Z plane in Kronocentric Solar Magnetospheric (KSM) co-ordinates. The
 247 KSM coordinate system consists of Saturn at the origin, the x-axis directed towards the
 248 sun, the z-axis existing in the plane made by x and Saturn's dipole axis, and y completes
 249 the system. As detailed in Section 3, we manually examined portions of this dataset and
 250 applied LFE and non-LFE labels to specific intervals. The locations where LFEs (blue)
 251 and non-LFEs (orange) were labelled have also been overplotted. The panels (c-e) of
 252 figure 3 show histograms of normalised counts vs Range (R_S), Latitude ($^\circ$) and Local
 253 Time (hours) for Cassini's total time at Saturn (grey dotted line), the periods of labelled
 254 LFEs (blue) and the periods of labelled non-LFE (orange). The LFE counts at each bin
 255 are normalised by the total number of LFE counts. The total number of LFE-counts are
 256 defined as the sum of 180 sec intervals during all LFE events. The non-LFE counts and
 257 total Cassini counts are calculated in this way also. Cassini spent most of its time inside
 258 $\sim 50 R_S$ (the further radial distances were mostly during two distinct intervals: the first
 259 capture orbit in 2004 and the deepest magnetotail sampling in 2006). The vast majority
 260 of coverage was within $\sim 10^\circ$ either side of the equatorial plane, and there was a local time
 261 asymmetry in Cassini's exploration with more time spent at dawn (6 hours LT) than dusk
 262 (18 hours LT). We can see that for both Range and Latitude in particular, the labelled
 263 sections of LFE/Non-LFE mirror the spread of Cassini's trajectory closely. It is clear
 264 that the locations sampled are representative of the data in this plot. For the histogram
 265 of Local Time, the areas sampled in the labelled data do not correspond as closely to the
 266 range and latitude plots. For the LFEs, we see a peak in the early morning local time,
 267 a wide peak between 10-15 hours LT, and a deep trough at ~ 18 hours, followed by an
 268 increase again. The non-LFE curve has two peaks at approximately 11 and 24 hours. We
 269 see significantly lower values in between these peaks.

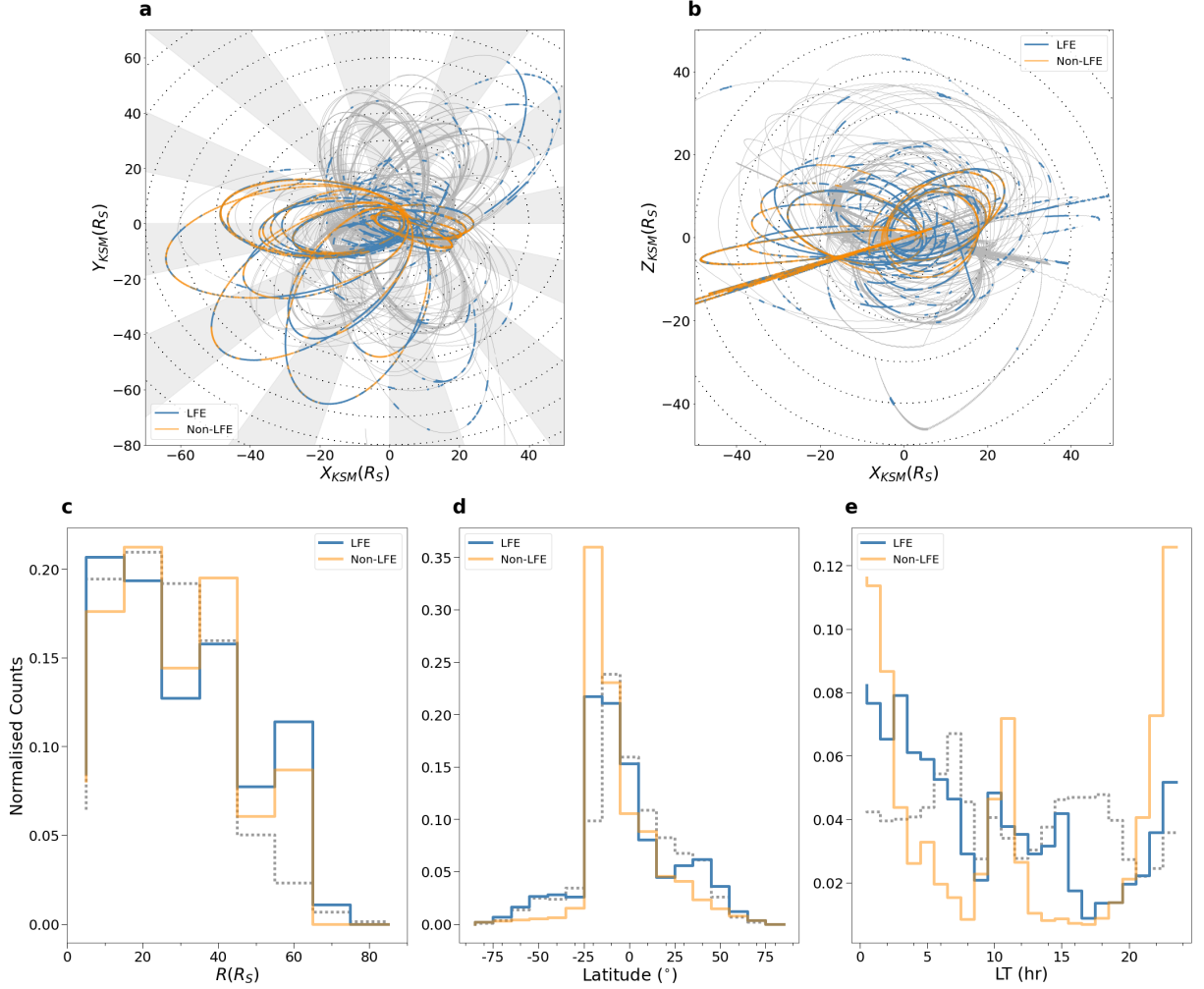


Figure 3: (a,b) Two panels showing Cassini’s trajectory, $Y(KSM)$ vs $X(KSM)$ and $Z(KSM)$ vs $X(KSM)$. Intervals where LFEs were found are indicated in blue and intervals confirmed to be without an LFE are marked in orange. In the background, hour long local time bins are indicated by alternately shading in grey. Successive concentric circles each increasing in radius by $10 R_S$ are indicated with dotted lines. Three panels showing histograms of (c) counts vs Range (R_S), (d) Latitude ($^\circ$) and (e) Local Time (hours) for Cassini’s trajectory (grey dotted), total LFEs labelled (blue) and non-LFEs labelled (orange).

270 5 Applications

271 The list of LFEs is curated at O’Dwyer et al. (2023) and we encourage the community to
 272 use it for a variety of purposes. Some examples of how we are currently employing this
 273 valuable dataset include:

- 274 • A training set for a supervised machine learning model. The authors of this paper
 275 are currently using it as a training set for a U-Net style architecture for semantic
 276 segmentation of LFEs.

- 277 • As a basis for case studies and statistical examination of the link between LFEs and
278 extreme magnetospheric events, including: large solar wind compressions (Ceconi
279 et al., 2022; Jackman et al., 2023) and magnetotail collapse (Bunce et al., 2005;
280 Jackman et al., 2009).
- 281 • Context for other activity, for example Wu et al. (2022) compared LFEs to a list
282 of Saturn Anomalous Myriametric radiation (SAM) events. They found there to be
283 a high occurrence rate of SAM events following LFEs suggesting they are possibly
284 associated with solar wind compressions of the magnetosphere. Fischer et al. (2023)
285 compared a list of ‘caterpillars, a special form of low frequency cutoff of SKR, to
286 LFEs occurring in 2006 and has linked their occurrence to LFEs associated with
287 solar wind compressions of the magnetosphere.
- 288 • As a basis for studying the mode of propagation (X-mode or O-mode) for lower fre-
289 quency emission. By looking at the polarization sense of LFEs observed at latitudes
290 $> 20^\circ$, we can determine their hemisphere of origin and their mode of propagation.
291 We could use this to investigate the conditions under which the CMI operates inside
292 the corresponding high altitude source regions.

293 6 Conclusions

294 In this paper we have outlined the necessity for the polygon selection of a subset of the
295 LFEs present in the Cassini/RPWS dataset. We built a visual criteria for the selection
296 of the LFEs based on literature and domain knowledge. It was then possible to develop
297 different classes of LFEs based on their appearance, which can be attributed to different
298 factors. The classes defined were as follows ‘LFE’, ‘LFE_{sm}’, ‘LFE_{sp}’, ‘LFE_{ext}’, ‘LFE_m’
299 and ‘LFE_{dg}’. The selection of LFEs was predominantly carried out in 2006 and 2008,
300 but also a small sample from other years of the mission. We were then able to use the
301 fully labelled periods of time in the Cassini mission to extract ‘NoLFE’ periods of the
302 mission, this ‘NoLFE’ label is taken to mean periods of time where we observe normal
303 SKR, narrowband emission or in fact no emission at all. These periods of time with
304 ‘NoLFE’ emission were separated into 980 five hour chunks of time. We then looked at
305 the distribution of the labelled periods of the 6 LFE classes and the ‘NoLFE’ class with
306 respect to location. The distribution of both LFE and non-LFE data mirror the spread of
307 Cassini’s trajectory closely, in respect to latitude and range. However, the distribution of
308 local time for the LFE and non-LFE data is contrasting to Cassini’s total coverage. We
309 have also outlined the possible applications of this list, which was in particular intended
310 for a machine learning application.

311 7 Acknowledgements

312 E.P. O’Dwyer’s, C. K. Louis’ and C. M. Jackman’s work at the Dublin Institute for Ad-
313 vanced Studies was funded by the Science Foundation Ireland Grant 18/FRL/6199. L.

314 Lamy acknowledges support from CNES and CNRS/INSU national programs of plane-
315 tology (PNP) and heliophysics (PNST).

316 **References**

317 Boischot A., et al., 1980, A new high-grain, broadband, steerable array to study Jovian
318 decametric emission, *Icarus*, *43*, 399

319 Bradley T. J., et al., 2020, Saturn's nightside dynamics during Cassini's f ring and proxi-
320 mal orbits: Response to solar wind and planetary period oscillation modulations, *Jour-
321 nal of Geophysical Research: Space Physics*, *125*, e2020JA027907

322 Bunce E. J., Cowley S. W. H., Wright D. M., Coates A. J., Dougherty M. K., Krupp N.,
323 Kurth W. S., Rymer A. M., 2005, In situ observations of a solar wind compression-
324 induced hot plasma injection in saturn's tail, *Geophysical Research Letters*, *32*

325 Bunce E. J., et al., 2010, Extraordinary field-aligned current signatures in Saturn's high-
326 latitude magnetosphere: Analysis of Cassini data during revolution 89, *Journal of Geo-
327 physical Research: Space Physics*, *115*

328 Carbary J. F., Mitchell D. G., 2013, Periodicities in Saturn's magnetosphere, *Reviews of
329 Geophysics*, *51*, 1

330 Cecconi B., Zarka P., 2005, Direction finding and antenna calibration through analytical
331 inversion of radio measurements performed using a system of two or three electric dipole
332 antennas on a three-axis stabilized spacecraft, *Radio Science*, *40*, RS3003

333 Cecconi B., Witasse O., Jackman C. M., Sánchez-Cano B., Mays M. L., 2022, Effect of an
334 interplanetary coronal mass ejection on Saturn's radio emission, *Frontiers in Astronomy
335 and Space Sciences*, *9*

336 Clarke J. T., et al., 2009, Response of Jupiter's and Saturn's auroral activity to the solar
337 wind, *Journal of Geophysical Research: Space Physics*, *114*

338 Crameri F., Shephard G., Heron P., 2020, The misuse of colour in science communication,
339 *Nat Commun*, *11*, 5444

340 Desch M. D., 1982, Evidence for solar wind control of saturn radio emission, *Journal of
341 Geophysical Research: Space Physics*, *87*, 4549

342 Desch M. D., Rucker H. O., 1983, The relationship between Saturn kilometric radiation
343 and the solar wind, *J. Geophys. Res.*, *88*, 8999

344 Dougherty M., et al., 2004, The cassini magnetic field investigation, *Space Science Re-
345 views*, *114*, 331

346 Dougherty M., Kellock S., Sloatweg A., Achilleos N., Joy S., Mafi J., 2019, CASSINI
347 ORBITER MAG CALIBRATED SUMMARY AVERAGED V2.0, NASA Planetary
348 Data System, doi:<https://doi.org/10.17189/1519602>

- 349 Fischer G., Taubenschuss U., Píša D., Lamy L., Wu S., Ye S., Jackman C., O'Dwyer
350 E., 2023, A special form of low-frequency cutoff of Saturn Kilometric Radiation, *in*
351 *Planetary, Solar and Heliospheric Radio Emissions IX*, ed. C. K. Louis, C. M. Jack-
352 man, G. Fischer, A. H. Sulaiman, P. Zucca, Dublin Institute for Advanced Studies, ,
353 doi:<https://doi.org/10.25546/103099>
- 354 Galopeau P. H. M., Lecacheux A., 2000, Variations of Saturn's radio rotation period
355 measured at kilometer wavelengths, *Journal of Geophysical Research: Space Physics*,
356 *105*, 13089
- 357 Gurnett D. A., Kurth W. S., Scarf F. L., 1981, Narrowband electromagnetic emissions
358 from Saturn's magnetosphere, , *292*, 733
- 359 Gurnett D. A., et al., 1995, The Polar Plasma Wave Instrument, , *71*, 597
- 360 Gurnett D. A., et al., 2004, The Cassini Radio and Plasma Wave Investigation, *Space Sci.*
361 *Rev.*, *114*, 395
- 362 Gurnett D., et al., 2005, Radio and plasma wave observations at Saturn from Cassini's
363 approach and first orbit, *Science (New York, N.Y.)*, *307*, 1255
- 364 Jackman C., Achilleos N., Bunce E., Cecconi B., Clarke J., Cowley S. W. H., Kurth
365 W. S., Zarka P., 2005, Interplanetary conditions and magnetospheric dynamics during
366 the Cassini orbit insertion fly-through of Saturn's magnetosphere, *J. Geophys. Res.*,
367 *110*, A10212
- 368 Jackman C. M., Lamy L., Freeman M. P., Zarka P., Cecconi B., Kurth W. S., Cowley S.
369 W. H., Dougherty M. K., 2009, On the character and distribution of lower-frequency
370 radio emissions at Saturn and their relationship to substorm-like events, *Journal of*
371 *Geophysical Research: Space Physics*, *114*
- 372 Jackman C. M., O'Dwyer E. P., Louis C. K., Fogg A. R., Waters J. E., Lamy L., 2023,
373 Using crossings of saturn's magnetospheric boundaries to explore the link between
374 upstream conditions and radio emission., *in Planetary, Solar and Heliospheric Radio*
375 *Emissions IX*, ed. C. K. Louis, C. M. Jackman, G. Fischer, A. H. Sulaiman, P. Zucca,
376 Dublin Institute for Advanced Studies, , doi:<https://doi.org/10.25546/103100>
- 377 Kaiser M. L., Desch M. D., 1984, Radio emissions from the planets Earth, Jupiter, and
378 Saturn, *Reviews of Geophysics*, *22*, 373
- 379 Kaiser M. L., Desch M., Warwick J., Pearce J., 1980, Voyager Detection of Nonthermal
380 Radio Emission from Saturn, *Science*, *209*, 1238
- 381 Kaiser M. L., Desch M. D., Kurth W. S., Lecacheux A., Genova F., Pedersen B. M.,
382 Evans D. R., 1984, in eds Gehrels T., Matthews M. S., , , Saturn. pp 378–415
- 383 Kurth W., et al., 2005, An Earth-like correspondence between Saturn's auroral features
384 and radio emission, *Nature*, *433*, 722

- 385 Kurth W., et al., 2016, Saturn kilometric radiation intensities during the Saturn auroral
386 campaign of 2013, *Icarus*, *263*, 2
- 387 Kurth W. S., et al., 2017, The Juno Waves Investigation, , *213*, 347
- 388 Lamy L., 2017, The Saturnian kilometric radiation before the Cassini Grand Finale, in
389 *Planetary Radio Emissions VIII*, eds Fischer, G. and Mann, G. and Panchenko, M.
390 and Zarka, P., pp 171–190 (arXiv:1709.07693), doi:10.1553/PRE8s171
- 391 Lamy L., Zarka P., Cecconi B., Prangé R., Kurth W. S., Gurnett D., 2008, Saturn Kilo-
392 metric Radiation: average and statistical properties, *J. Geophys. Res.*, *113*
- 393 Lamy L., Cecconi B., Zarka P., 2009, Cassini/RPWS/HFR LESIA/Kronos SKR Data
394 Collection (Version 1.0), PADC, doi:https://doi.org/10.25935/zkxb-6c84
- 395 Lamy L., et al., 2013, Multispectral simultaneous diagnosis of Saturn’s aurorae throughout
396 a planetary rotation, *Journal of Geophysical Research: Space Physics*, *118*, 4817
- 397 Lamy L., et al., 2018, The low-frequency source of Saturn’s kilometric radiation, *Science*,
398 *362*, eaat2027
- 399 Louis C. K., Zarka P., Dabidin K., Lampson P. A., Magalhães F. P., Boudouma A.,
400 Marques M. S., Cecconi B., 2021, Latitudinal Beaming of Jupiter’s Radio Emissions
401 From Juno/Waves Flux Density Measurements, *Journal of Geophysical Research (Space*
402 *Physics)*, *126*, e29435
- 403 Louis C. K., et al., 2022a, SPACE Labelling Tool Version 2.0.0,
404 doi:10.5281/zenodo.6886528
- 405 Louis C., et al., 2022b, The “SPectrogram Analysis and Cataloguing Environment”
406 (SPACE) labelling tool, *Frontiers in Astronomy and Space Sciences*, *9*
- 407 Louis C. K., Smith K. D., Jackman C. M., Fogg A. R., Waters J. E., O’Dwyer E. P.,
408 Granroth L., 2023, Latitudinal distribution of auroral kilometric radiation based on
409 polar spacecraft observations., in *Planetary, Solar and Heliospheric Radio Emissions*
410 *IX*, ed. C. K. Louis, C. M. Jackman, G. Fischer, A. H. Sulaiman, P. Zucca, Dublin
411 *Institute for Advanced Studies*, , doi:https://doi.org/10.25546/103088
- 412 Marques M. S., Zarka P., Echer E., Ryabov V. B., Alves M. V., Denis L., Coffre A., 2017,
413 Statistical analysis of 26 yr of observations of decametric radio emissions from Jupiter,
414 , *604*, A17
- 415 Menietti J. D., Mutel R. L., Schippers P., Ye S.-Y., Gurnett D. A., Lamy L., 2011,
416 Analysis of Saturn kilometric radiation near a source center, *Journal of Geophysical*
417 *Research: Space Physics*, *116*
- 418 Morioka A., et al., 2008, AKR breakup and auroral particle acceleration at substorm
419 onset, *Journal of Geophysical Research (Space Physics)*, *113*, A09213
- 420 Mutel R. L., et al., 2010, CMI growth rates for Saturnian kilometric radiation, *Geophysical*
421 *Research Letters*, *37*

- 422 O'Dwyer E. P., Jackman C. M., Domijan K., Lamy L., Louis C. K., 2023, Selection of
423 Low Frequency Extensions of Saturn Kilometric Radiation detected by Cassini/RPWS.,
424 doi:10.5281/zenodo.7895766, <https://doi.org/10.5281/zenodo.7895766>
- 425 Reed J. J., Jackman C. M., Lamy L., Kurth W. S., Whiter D. K., 2018, Low-Frequency
426 Extensions of the Saturn Kilometric Radiation as a Proxy for Magnetospheric Dynam-
427 ics, *Journal of Geophysical Research (Space Physics)*, 123, 443
- 428 Taubenschuss U., Rucker H. O., Kurth W. S., Cecconi B., Zarka P., Dougherty M. K.,
429 Steinberg J. T., 2006, Linear prediction studies for the solar wind and Saturn kilometric
430 radiation, *Annales Geophysicae*, 24, 3139
- 431 Wang Z., Gurnett D. A., Fischer G., Ye S.-Y., Kurth W. S., Mitchell D. G., Leisner J. S.,
432 Russell C. T., 2010, Cassini observations of narrowband radio emissions in Saturn's
433 magnetosphere, *Journal of Geophysical Research: Space Physics*, 115
- 434 Wu C., Lee L., 1979, A theory of the terrestrial kilometric radiation, *Astrophys. J.*, 230,
435 621
- 436 Wu S., Ye S., Fischer G., Wang J., Long M., Menietti J., Cecconi B., Kurth W., 2021,
437 Statistical Study on Spatial Distribution and Polarization of Saturn Narrowband Emis-
438 sions, *The Astrophysical Journal*, 918, 64
- 439 Wu S. Y., et al., 2022, Saturn Anomalous Myriametric Radiation, a New Type of Saturn
440 Radio Emission Revealed by Cassini, *Geophysical Research Letters*, 49, e2022GL099237
- 441 Ye S.-Y., Gurnett D. A., Groene J. B., Wang Z., Kurth W. S., 2010, Dual periodicities
442 in the rotational modulation of Saturn narrowband emissions, *Journal of Geophysical
443 Research: Space Physics*, 115

0.3 Chapter II

This chapter consists of an article published in the Journal of Geophysics Research titled ‘Image-Based Classification of Intense Radio Bursts from Spectrograms: An Application to Saturn Kilometric Radiation’. I was the first author of this article. My contributions consist of preparing the training set for the model training, separating the training set into model training, validation and testing sets, designing the model architecture based on the Unet (Ronneberger, Fischer, and Brox, 2015), tuning the model hyperparameters, conducting the post-processing steps, applying the trained model to the full dataset and extracting the resulting catalogue of LFEs, preparing all figures in the article and contributing to the writing of the article along with my co-authors.

Key Points:

- Supervised learning applied to database of labeled polygons marked on radio spectrograms
- Focus on Low Frequency Extensions of Saturn Kilometric Radiation to return a full catalog from the Cassini mission
- A modified U-Net architecture achieved median Intersection over Union values of 0.98 and 0.97 across the training and testing set

Correspondence to:




C. M. Jackman,
cjackman@cp.dias.ie

Citation:

O'Dwyer, E. P., Jackman, C. M., Domijan, K., & Lamy, L. (2023). Image-based classification of intense radio bursts from spectrograms: An application to Saturn Kilometric Radiation. *Journal of Geophysical Research: Space Physics*, 128, e2023JA031926. <https://doi.org/10.1029/2023JA031926>

Received 25 JUL 2023
 Accepted 5 OCT 2023

Image-Based Classification of Intense Radio Bursts From Spectrograms: An Application to Saturn Kilometric Radiation

E. P. O'Dwyer^{1,2} , C. M. Jackman¹ , K. Domijan², and L. Lamy^{3,4} 

¹School of Cosmic Physics, DIAS Dunsink Observatory, Dublin Institute for Advanced Studies, Dublin, Ireland, ²Department of Mathematics and Statistics, Maynooth University, Maynooth, Ireland, ³LESIA, Observatoire de Paris, CNRS, Université PSL, Sorbonne Université, Université Paris Cité, Meudon, France, ⁴Aix-Marseille Université, CNRS, CNES, LAM, Marseille, France

Abstract Saturn Kilometric Radiation (SKR) is a non-thermal auroral emission with peak emission occurring at 100–400 kHz. Its properties have been extensively studied since Cassini's arrival at Saturn until mission end with its Radio and Plasma Wave Science (RPWS) experiment. Low Frequency Extensions (LFEs) of SKR which consist of global intensifications of SKR accompanied by extensions of the main SKR band down to lower frequencies have been studied in particular. Low Frequency Extensions result from internally driven tail reconnection and from solar wind compressions of the magnetosphere, which also trigger tail reconnection. They have been cataloged through visual inspection with two approaches, using an intensity threshold for LFEs in 2006 (Reed et al., 2018, <https://doi.org/10.1002/2017ja024499>) and more recently O'Dwyer et al. (2023a, <https://doi.org/10.25546/103103>) produced a sample of LFEs detected by Cassini/RPWS by fitting their exact frequency-time coordinates with polygons. In this study we use the latter catalog of LFEs as a training set for an image based machine learning algorithm to classify all LFEs detected by Cassini/RPWS. The inputs to the model are multi-channel images consisting of spectrogram images in flux density and degree of circular polarization. The outputs of the model are binary masks showing the exact location of the LFE in frequency-time space. The median Intersection Over Union across the testing and training set were calculated to be 0.97 and 0.98, respectively. The output of this study is a list of all 4,874 LFEs detected using this method. The list of LFE frequency-time coordinates is available for use amongst the scientific community.

Plain Language Summary We are using radio observations from the Cassini spacecraft that was in orbit around the planet Saturn for 13 years. We want to search for characteristic features of Saturn's auroral radio emissions (called Saturn Kilometric Radiation or SKR) in the data stream from the radio instrument—specifically events called Low Frequency Extensions (LFEs). The edges of these events can be tracked in time-frequency spectrograms of Cassini radio observations. We find several hundred examples of the LFEs that we're looking for, and feed these into a computer algorithm which learns what they look like. The algorithm can then be applied to new/unseen data and we allow it to search for similar events. The end result is an extensive catalog of all the LFEs observed throughout the 13-year near-Saturn mission by the radio instrument of Cassini. This catalog can be used by the scientific community as a basis for statistical studies of Saturn's radio emissions. The machine learning aspect of this work can be adapted through something known as transfer learning to other planets where we look for similar features in data.

1. Introduction

Saturn's radio emissions have been observed for several decades by spacecraft; initially by the Voyager Planetary Radio Astronomy instrument and subsequently by Ulysses Unified Radio and Plasma Wave Instrument (Galopeau & Lecacheux, 2000; Kaiser et al., 1980). More recently the Radio and Plasma Wave Science (RPWS) instrument aboard the Cassini spacecraft has been observing Saturn's radio emissions from mid-2004 to late 2017 (Gurnett et al., 2004). The most powerful radio emission from Saturn is the Saturn Kilometric Radiation (SKR), which is a non-thermal, auroral emission that occurs in the range of a few kHz to 1.2 MHz (Kaiser & Desch, 1984; Lamy, 2017, and references therein). Peak emission occurs in the frequency range of approximately 100–400 kHz (Lamy et al., 2008). SKR is generated by the cyclotron maser instability (Lamy et al., 2010; Menietti et al., 2011; Mutel et al., 2010; Wu & Lee, 1979). Radio waves are generated at frequencies close to the local electron gyrofrequency f_{ce} by electrons that are accelerated along field lines in auroral zones. As $f_{ce} = qB/(2\pi m)$, where q is the electron charge, B is the local magnetic field strength, and m is the electron mass, the frequency of the radio

emission is directly proportional to the local magnetic field strength and inversely proportional to the distance from the planet's centre. SKR waves propagate mainly in the Right-handed eXtraordinary (R-X) mode and its fully elliptically polarized, right-handed and left-handed emissions can be sourced back to the southern and northern hemispheres, respectively. SKR is radiated anisotropically along a thin, few degrees wide, hollow cone with a large aperture angle with respect to the local magnetic field vector. This results in strong visibility effects depending on the position of the observer (e.g., Lamy et al., 2023).

Occasionally, the SKR emission intensifies and extends to upper and especially lower frequencies, in events which have been termed Low Frequency Extensions (LFEs) (Bunce et al., 2005; Jackman et al., 2009; Reed et al., 2018). Analogous signatures have been observed at the Earth (Morioka et al., 2008), and there used as a diagnostic of magnetospheric dynamics, in particular linking to magnetotail reconnection and substorm activity. At Saturn, LFEs have been linked to solar wind compression-induced dynamics and global reconfigurations of the magnetosphere which result in increased precipitation of energetic particles into the auroral zone. Our motivation in this work is to conduct a complete examination of the 13-year Cassini near-Saturn data set, to compile a catalog of all observed LFEs which in turn can spark follow-on statistical and case studies of the properties of these SKR features and their links to magnetospheric dynamics. In order to achieve this aim, we have taken an image-based machine learning (ML) approach.

O'Dwyer et al. (2023a) details the generation and curation of an extensive labeled set of LFEs from the Cassini radio data which can be found at O'Dwyer et al. (2023b). We note the difference in our approach in comparison to that of Reed et al. (2018), who produced an extensive catalog of LFEs detected by Cassini/RPWS in 2006 using a numerical criterion for integrated power in two frequency ranges. The Reed list consisted of the LFE start and stop times. In comparison, the list produced by O'Dwyer et al. (2023a) consists of the frequency-time coordinates of the exact position of the LFE in the time-frequency spectrograms of the SKR flux density and degree of circular polarization detected by Cassini/RPWS. More precisely, they labeled 984 LFEs in total and these were labeled according to distinct classes. There are six classes: LFE (standard appearance), LFE_m (for "massive"), LFE_{sp} (for "sparse"), LFE_{ext} (for "extinction"), LFE_{dg} (for "data-gap"), and LFE_{sm} (for "small"). The list also contains a set of start and stop times for confirmed "NoLFE" occurrences in the Cassini/RPWS data set. "NoLFE" may consist of SKR without an LFE, narrowband emission centered at 5 and 20 kHz, respectively and also no radio emission at all. There are 980 "NoLFE" intervals in the labeled data set and each are 5 hr long.

This paper focuses on the application of advanced ML techniques to the classification of LFEs observed by Cassini/RPWS. Section 2 covers the used data set, and the broad properties of the training data (LFE list). Section 3 covers our choice of ML architecture, while Section 4 details the results of the application of the model, and the ultimate outputs of the classification. Section 5 ends with a summary and future perspectives.

2. Data

2.1. Cassini Radio Data

For this study, we used data obtained by the Cassini RPWS High Frequency Receiver (RPWS HFR, Gurnett et al., 2004). The HFR quasi-continuously measures the wave electric field with three 1 m-long electric monopole antennas within the frequency range of 3.5 kHz–16 MHz. Subsequently, the Stokes parameters, including the total flux density S and the normalized degree of circular polarization V , were computed by performing goniopolarimetric or direction finding inversions from auto- and cross-correlations of the antenna signals (Cecconi & Zarka, 2005). Lamy et al. (2008) calibrated the flux densities and processed the data such that solar type III bursts and radio frequency interferences were removed and solely Saturn's emission in the kilometer range remained, including SKR and narrowband-emission near 5 and 20–40 kHz. To account for the frequent changes of instrumental modes, the data were also re-integrated into regular time-frequency arrays with fixed spectral and temporal resolution. Overall, the final data set consists of a calibrated, homogeneous time series of S ($W \cdot m^{-2} \cdot Hz^{-1}$) normalized to 1 AU and V for each frequency channel. There are 48 frequency channels, sampling in the range of 3.5–1,500 kHz at a temporal resolution of 180 s. The first 24 frequency channels are logarithmically spaced (with $\Delta f/f = 20\%$), and the subsequent 24 are linearly spaced (with $\Delta f = 50$ kHz). This SKR data collection, referenced as Lamy et al. (2009), was primarily constructed to investigate SKR properties on a long-term basis and is therefore ideal to track LFEs throughout the Cassini mission. Finally, we have removed from the SKR data set a list of time intervals during which the sign of V was considered as erroneous. These unreliable time intervals

Table 1
Distribution of Low Frequency Extension Categories Within Labeled Data

Type	Count	Description
LFE	479	Standard appearance
LFE _m	96	LFEs longer than a single planetary rotation
LFE _{sp}	99	LFE with sparse emission
LFE _{sm}	164	LFE that is of intermediate extension, excursion to >40 kHz but <100 kHz
LFE _{dg}	111	LFE with a datagap
LFE _{ext}	35	LFE with extinction at high frequencies

correspond to periods when the 2-antenna plane is coming close to the wave direction of arrival and represent only a small portion of the data set (less than 1%–2% per year).

2.2. LFE Catalog

We are using a catalog detailed in O’Dwyer et al. (2023b) which consists of a selection of LFEs detected by Cassini using a polygon selector tool (Louis et al., 2022). O’Dwyer et al. (2023a) outlines their exact criterion for LFE selection, which primarily consists of a minimum frequency extension of SKR to 40 kHz, significant intensification of SKR above background level and continuous emission with respect to frequency. The LFEs are divided into six classes which are described in detail in the paper. There are 984 LFEs in total and the exact frequency-time coordinates of each is provided.

The catalog provides continuous labeling for 2006 and several months in 2008, as well as a sample of LFEs from most other years of the mission. 2006 was chosen as it allows for blind comparison with the catalog by Reed et al. (2018). Several months in 2008 were labeled in order to include LFEs sampled from different spacecraft locations. In 2006 Cassini spent the majority of its time within $\pm 10^\circ$ latitude of the equator, and reached distances up to $\sim 68 R_S$ along Saturn’s magnetotail. By contrast, in 2008 Cassini orbited at latitudes $> 50^\circ$ and at distances much closer to the planet ($< 40 R_S$). The catalog also provides a list of 980 5-hr periods of data where it is confirmed to not see an LFE: these may consist of SKR without an LFE, narrowband emission near 5 and 20 kHz or no emission at all. A brief description of each class of LFE, as well as their respective counts are presented in Table 1. The “LFE” class is defined as an LFE with typical appearance: it consists of a continuous extension of intensified SKR down to 40 kHz or lower. The “LFE_m” class (“m” is for massive) is defined as an LFE that occurs over an interval of one planetary rotation (~ 11 hr) or longer. The “LFE_{sp}” (for “sparse”) is defined as intensified SKR that extends down to at least 40 kHz, but with some frequency channels not displaying intensified emission. As a result the LFE has a sparse appearance. “LFE_{sm}” (for “small”) is defined as intensified SKR that extends down below the main frequency band, but does not extend down to 40 kHz. The frequency extension of this class is intermediate between the lower limit of the main band (100 kHz) and 40 kHz, “LFE_{sm}” LFEs extend down to ~ 70 kHz at least. “LFE_{dg}” is an LFE with a datagap during its occurrence. The datagap may occur during or cut short the LFE by occurring at the beginning or end of the LFE. A datagap is defined as a full gap in emission over all frequency channels for multiple consecutive timesteps. “LFE_{ext}” is defined as an LFE with an extinction in the main frequency band of SKR. This may be a complete or partial extinction of emission at the main band frequencies. This occurs as a result of a viewing effect as discussed by Lamy et al. (2008), when the observer is at high latitudes. Refer to Figure 2 of O’Dwyer et al. (2023a) for an example of each class shown in frequency-time spectrograms of flux density and degree of circular polarization.

2.3. Spacecraft Coverage

Cassini orbited Saturn from July 2004 until September 2017, over 13 years in total, and sampled a broad range of latitudes and radial distances. Figure 1 shows the coverage by Cassini from 2004 day 001 to 2017 day 255. The gray trace in Figure 1a illustrates the latitudinal coverage (right-hand y-axis) as a function of time, showing the diversity between equatorial sampling (such as throughout 2010–2012) and higher latitude sampling (including during 2008–2009 and the Grand Finale orbits in 2017). Figure 1b shows the spread in latitude versus local time for each of the orbits of Cassini.

In addition to showing the overall mission coverage, the aim of this figure is to illustrate the diversity of spacecraft locations included in the sample of data labeled for our supervised learning work. The position of the observing spacecraft can have a huge impact on the nature of the measured radio data. It was thus important to account for the vast array of locations explored by Cassini in the subset of LFEs used for model training (a diverse training set is essential to account for visibility issues associated with inhomogenous beaming of radio emission etc.). Overplotted on the gray trace in Figure 1a we show histograms for occurrence of LFEs (orange) and non-LFEs (blue) as a function of time, with a bin size of 50 days. As shown, LFEs were sampled from nearly every year of the mission and a wide variety of spacecraft latitudes were included. The entirety of 2006 was labeled, as well as

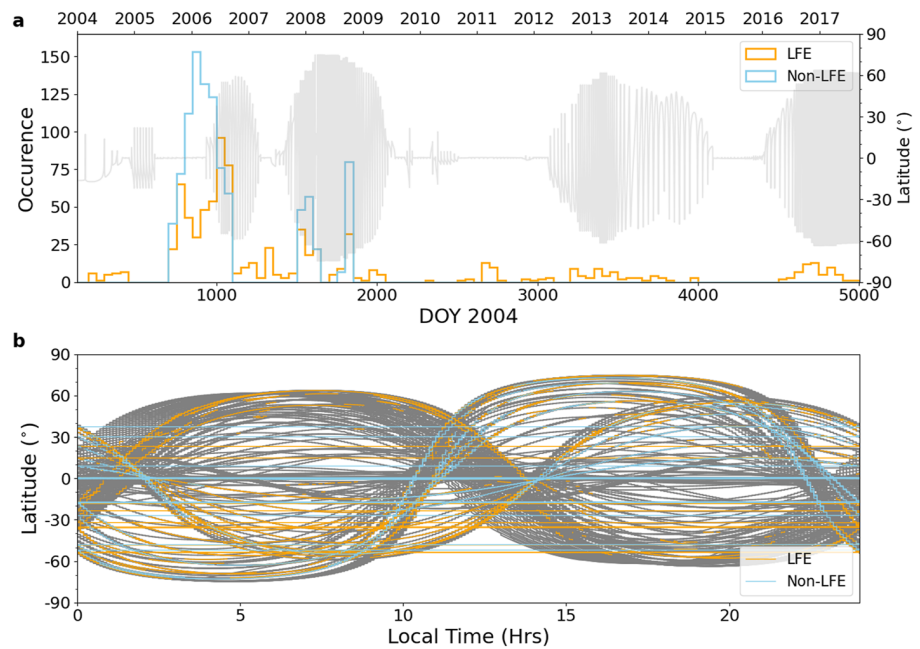


Figure 1. (a) Histograms for occurrence of Low Frequency Extensions (LFEs) (orange) and non-LFEs (blue) as a function of time, with a bin size of 50 days. We plot Cassini's latitude from day 1 of 2004 to day 255 of 2017 in the background in gray (with y-axis shown on the right). (b) Plot of spacecraft latitude (°) versus Local Time (hours) for the same time period as in panel (a), with periods of LFEs and non-LFEs overplotted in orange and blue, respectively.

all LFEs in March, May, and December of 2008. The fully labeled sections were used to find the sections of data without LFE. The duration of the LFEs vary, and the non-LFEs were set to 5 hr in length.

3. Methods

Our aim in this work is to use our labeled training data (the set of polygons drawn around LFEs and the intervals of non-LFE events from a subset of Cassini's exploration), and apply a supervised machine learning approach to the classification of LFEs from the entire Cassini data set. It is perhaps contrary to expectations to use an image-based technique for time series data. However, the radio data are typically viewed on a spectrogram, a time-frequency image showing signal strength of flux density and degree of circular polarization, an interval of which can be considered as an image. Typical time series network models can be trained to accurately predict the occurrence of an LFE at a specific time point, but do not produce the exact co-ordinates in the frequency time space over which the LFE occurs. This is very important information to preserve and can be represented by semantic segmentation output of image-based models.

In early iterations of this work, we considered applying time series machine learning approaches such as Recurrent Neural Networks or Long Short Term Memory, as these are set up for adoption with time series data. However, we didn't simply want to retain a start/stop time of an LFE: we wanted to retain the full mask/shape of the event, as the nature of the timing and morphology of the extension to lower frequencies contains very important physics about the nature of the radio source and perhaps even information which can inform us about the ignition mechanism for radio bursts. In Figure 2 we show two examples of dynamic spectra from the catalog by O'Dwyer et al. (2023b) ("LFE" and "NoLFE" class, respectively). The left-hand example which contains an LFE has the polygon selection indicated by dotted lines. The bottom panels in each case show the corresponding masks, which are generated by setting emission within the polygon to 1 and emission outside of the polygon to zero. Thus the "NoLFE" case is an empty mask. This figure shows the information we would like to preserve in the output of our model. Considering the requirement to categorize each pixel in the image/mask, we have chosen to use a modified U-Net architecture (Ronneberger et al., 2015) for the semantic segmentation of LFEs.

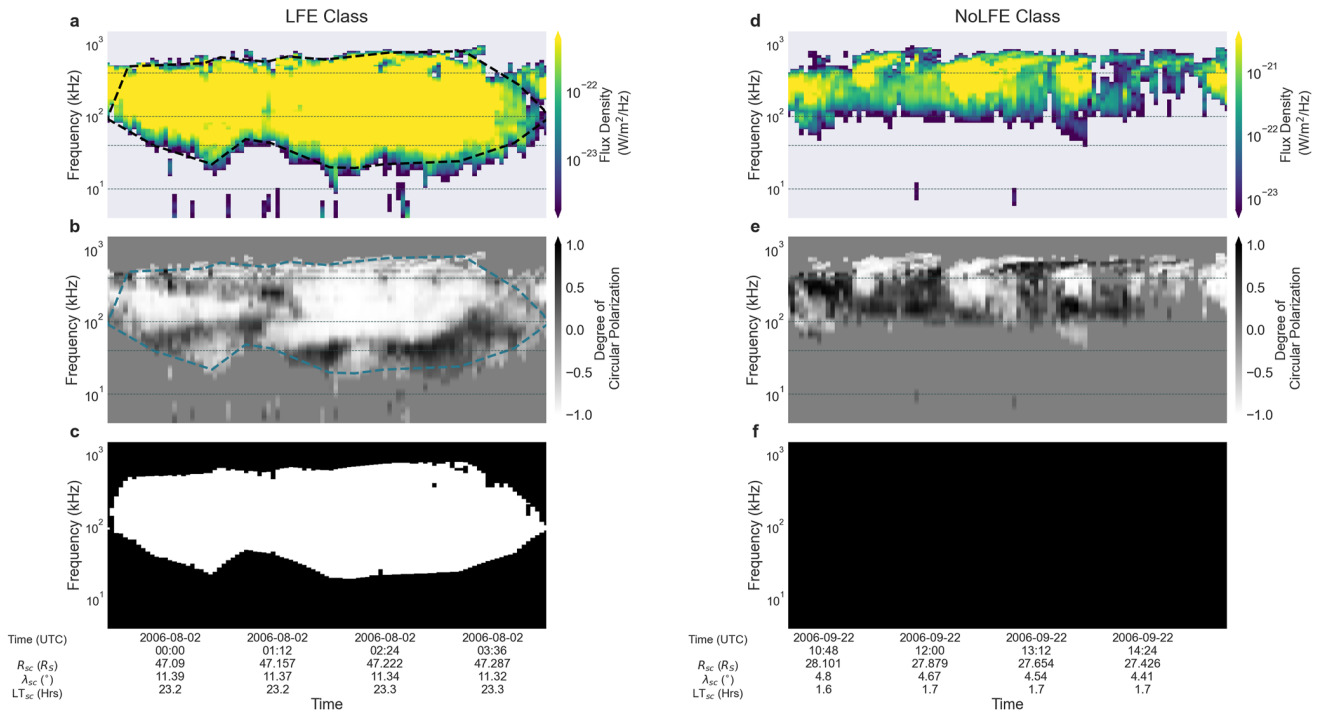


Figure 2. Examples of the “Low Frequency Extension (LFE)” (left-hand panels) and “NoLFE” (right-hand panels) classes and their corresponding masks. Panels (a, b) and show an LFE present in the centre of Cassini Radio and Plasma Wave Science dynamic spectra in flux density and degree of polarization for the same time range. LFE polygon selection is shown in black and blue, respectively. Panel (c) shows the corresponding mask for the LFE polygon selection. Panels (d–f) are of the same format for the “NoLFE” case. Since this is a “NoLFE” class example, panel (f) displays an empty mask. The respective class labels are also indicated by the title on panels (a, d). Note that in panels (a, b) and (d, e), the weak emission present at and below 10 kHz is Saturn’s narrowband emission.

3.1. Model Architecture

The deep-learning model employed in this study is the U-Net (Ronneberger et al., 2015). It was originally used for Biomedical Image Segmentation but has been applied in many other domains. U-Net has been shown to perform accurate image segmentation while trained on relatively small labeled data sets. Its name is derived from the encoder-decoder structure of the model, where the contracting-expanding path resembles a U in shape. The U-Net consists of convolutional and downsampling (max-pooling) layers in the contracting path, and convolutional and upsampling layers in the expanding path. Each level in the expanding path includes a concatenation with the corresponding feature map from the contracting path. U-Net output is a probability value for each of the pixels, which can be thresholded to obtain binary masks. For our purposes, the output is a single mask to identify the LFE. U-Net takes in multi-channel images as input.

Figure 3 shows a schematic of the modified U-Net architecture used in this study. The down-sampling path contains 5 blocks: each block consisting of two 3×3 padded convolutional layers, followed by a rectified linear unit (ReLU) activation. Between the convolutional layers a dropout layer is applied, with a dropout rate of 0.4. Then a 2×2 with stride 2 max-pooling operation is applied. The number of filters used in the convolutional layers is doubled with every block, starting with 32 filters at the first block and ending with 1,024 filters at the last block. After the downsampling path, there is a bottleneck. The bottleneck consists of two 3×3 padded convolutional layers, each with 2048 filters, followed by ReLU activation. A kernel regularizer with l1 regularization penalty at a rate of 1×10^{-6} is used on the convolutional layers at the bottleneck. Following the bottleneck is the up-sampling path. The up-sampling path comprises five corresponding blocks. Each block consist of a 2×2 up-sampling operation, followed by a concatenation of the corresponding feature map from the down-sampling path, and then two 3×3 padded convolutional layers each with ReLU activation. The number of filters used in each block is halved each time. Finally, a 1×1 padded convolution with a single filter and a sigmoid activation is applied. The sigmoid activation function returns an array with probability values between 0 and 1 at each pixel which can be thresholded to obtain the output binary mask.

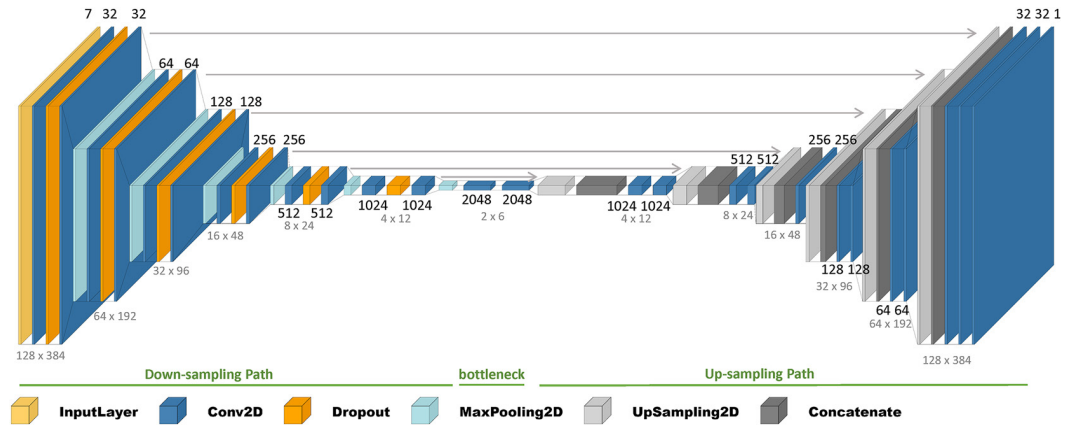


Figure 3. Modified U-Net architecture. Each cuboid is a multi-channel feature map, colored by the operation it results from. The number of filters is denoted in black at the top/bottom of each convolutional layer (dark blue), and the dimensions of the inputs to each block are denoted in gray at the bottom of each block. Gray lines running from left to right indicate the feature maps to be concatenated. The layers present in the down-sampling, bottleneck, and up-sampling path are indicated with green lines.

3.2. Model Inputs

Our training set consisted of 820 spectrogram images with an LFE centered on the image (the time window of the spectrogram is restricted to LFE start to LFE end) and 980 spectrogram images of “NoLFE” type. We do not include the LFE_{sm} class in our training data, as it consists of an intermediate extension in frequency. We assert that the model should be trained with well-defined examples of LFEs only. We expanded our training set using data augmentation which is explained in detail in Section 3.3. The images containing an LFE are of varying duration due to the varying timescale over which the LFEs occur. They range from 0.415 to 96.9 hr with a mean duration of 7.76 hr. The “NoLFE” images are set to be 5 hr in duration. The images vary in size in the x (time) dimension but are consistently 384 pixels in the y (frequency) dimension. It is an issue to have images varying in size for the model as it is necessary to pre-define the exact input dimensions. U-Net model requires input images of the same pre-defined dimension, thus bilinear interpolation (Chollet et al., 2015) implemented in the python module `keras layer.resize` function was used to resize images to a set dimension of 384×128 pixels. The y-dimension remains the same, but the x-dimension is resized to 128 pixels. One hundred twenty-eight data points with a time resolution of 3 min corresponds to 6 hr and 24 min of data.

The inputs to the model consist of images with seven channels in total: this corresponds to an array with dimensions $384 \times 128 \times 7$. The first two channels comprise spectrogram images showing flux density and normalized degree of polarization. The degree of circular polarization was included as a channel along with flux density as it allows for the differentiation between SKR and non-cyclotron maser generated narrowband emissions centered at 5 kHz also present in the radio observations. The 5 kHz component is more weakly circularly polarized than the SKR, and has opposite polarization sense compared to SKR when observed from the same hemisphere. Four channels contain spacecraft trajectory information; spacecraft median latitude, spacecraft latitude standard deviation, spacecraft local time median and spacecraft local time standard deviation over the time range the spectrogram occurs. Each of these four parameters contains only a single value which is repeated at each point in the frequency \times time array. The final channel is a 2-D array comprising the corresponding frequency channel that was sampled in the flux density and degree of polarization array, repeated at each time-point. This channel gives the convolution access to input coordinates of the LFE events in the y (frequency) dimension. The values in each channel array are normalized to (0,1) interval.

3.3. Data Augmentation

One of the exceptional aspects of the U-Net as a deep learning model is that it requires few training images: it was originally trained with three data sets consisting of just 25, 30, and 35 images, respectively (Ronneberger et al., 2015). The original authors made heavy use instead of data augmentation in the form of elastic deformations by generating a coarse grid of random displacement vectors and interpolating to calculate the by-pixel

Table 2
Model Training Parameters

Train count	Validation count	Test count	Loss function	Optimizer	Learning rate	Batch size	Epochs
996 (49%)	537 (26%)	511 (25%)	Binary cross entropy	Adam	1×10^{-5}	8	132

Note. The percentage of the total of the train, validation, and test counts are indicated alongside their absolute counts.

displacement (Ronneberger et al., 2015). We also used several data augmentation techniques, specifically to remedy the issue of the LFE being centered in the middle of the image. This was done in three ways.

First we combined images of an LFE and non-LFE by simply concatenating the two together. The non-LFE image can be placed at either side of the LFE image. We randomly chose 100 images of an LFE and 100 without an LFE and concatenated 50% on the left of the given LFE and the remaining 50% on the right. Images with the “NoLFE” concatenated to the left were given the label “LFE_{aug1}” and those with “NoLFE” concatenated to the right were given “LFE_{aug2}.” Another method was to shift the LFE inside the given time window. Using LFEs between 8 and 12 hr in duration, we applied horizontal shifts so that part of the LFE is removed from the frame. We padded the shifted image with zeros so that the each image had a width of 10 hr. The factor the image was shifted by was randomly chosen from the range 0.45–0.65, with a step size of 0.05. This was done to 100 images in total, with 50% of images shifted to the left and the remaining 50% shifted to the right. Images shifted to the left were given the label “LFE_{aug3}” and those shifted to the right were given the label “LFE_{aug4}.” Finally, 44 images containing several LFEs were generated by finding LFEs that occurred within 3 hr of each other. Within the 44 images, the number of LFE instances per image ranged from 2 to 4 LFEs. These were given the label “LFE_{aug5}.”

3.4. Performance Metrics

Performance of the model's prediction is assessed by comparing at a pixel level the labeled image and the model prediction. In this work we use two metrics: Binary Accuracy and Average Intersection over Union (IoU) (Equations 1 and 2). After the output predictions are converted to a binary array, the predicted mask can be compared to the binary true mask. The average IoU is calculated by treating the binary array as an array with two classes, that is, pixels with a value of “1” are one class and pixels with a value of “0” are another class. We will just use the term “IoU” henceforth when discussing average IoU.

$$\text{Binary Accuracy} = (TP + TN) / (TP + TN + FP + FN) \quad (1)$$

1. Equation for Binary Accuracy of the model output. True positive (TP) denotes a correctly classified positive pixel (positive meaning value of “1”), true negative (TN) denotes a correctly classified negative pixel (negative meaning a value of “0”), false positive (FP) denotes a incorrectly classified negative pixel and false negative (FN) identifies an incorrectly classified positive pixel.

$$\text{Average IoU} = 1/2 \sum_0^1 (TP_n) / (TP_n + FP_n + FN_n) \quad (2)$$

2. Equation for Average IoU of the model output. The subscript n is denoting the class whose IoU we are calculating. In each case, the values for TP, TN, FN and FP are different depending on which class (0 or 1) we are using.

3.5. Model Training and Optimization

In Table 2, we list the hyper-parameters used in model training. These hyper-parameters were found by manually tuning the model.

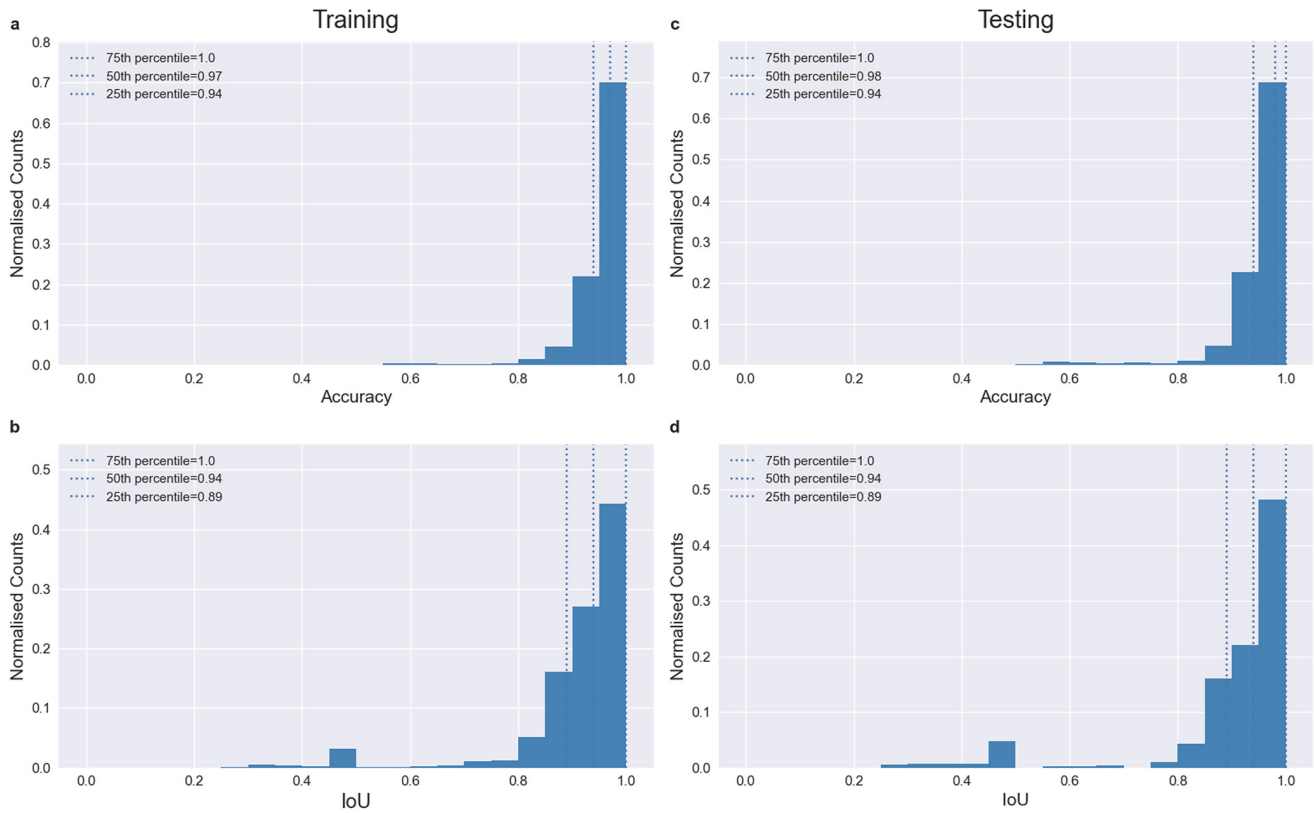


Figure 4. Four panel plot showing histograms of the accuracy and Intersection over Union per image for the train set (a, b) and the test set (c, d).

4. Results

The training data, which consisted of 2,044 images in total after the augmented images were generated, were split into the training, validation, and test set according to the ratios of 49:26:25. The augmented data were included in the training set only. Besides the augmented data, each LFE class and the non-LFE class were included in equal proportions in the training, validation and test set. The kernel weights in each convolutional layer were initialized using the Glorot uniform initializer (Glorot & Bengio, 2010) and the model was trained for 132 epochs using mini-batches of 8 images, with the weights being updated after each mini-batch. After all of the training data were inputted to the model, the validation data were inputted and the weights were updated. This process was repeated for each epoch. After training, the model makes predictions on the test set.

The output of the model is a 2D array of shape (384, 128) with a value between 0 and 1 at each point in the array corresponding to the probability that a given point belongs to the positive class. A threshold is applied to the probabilities to ascertain whether they belong to the positive or negative class. Typically 0.5 is used as this threshold, but we may yield a higher IoU when a different threshold is used. In order to calculate the probability threshold for IoU that yields the highest average value across the whole testing set, we calculate the mean IoU of all images in the test set for different thresholds. We calculated the mean IoU for thresholds between 0.1 and 0.9 inclusive, with a step size of 0.05. We found that a threshold of 0.65 yielded the best mean IoU for the testing set. This value is used for calculating the IoU and is the threshold used for converting from model output to binary mask.

On the basis of the outputs from the test set, we calculated the IoU and in Figure 4 show histograms of the IoU statistics. In Figures 5 and 6, a number of inputs from the test set are shown along with their corresponding predicted mask. Examples in Figure 5 show well classified images and those in Figure 6 show poorly classified images. In Table 3, we see list of mean loss, accuracy and IoU, as well as standard deviation of each, for each class in the training and testing set. It is clear from this table that the performance varies across each class, the “NoLFE” class is at the peak in terms of loss, accuracy and IoU for both the training and test set. For all classes in the train and test set, we see values of at least 0.90 and 0.83 for the mean accuracy and mean IoU, respectively.

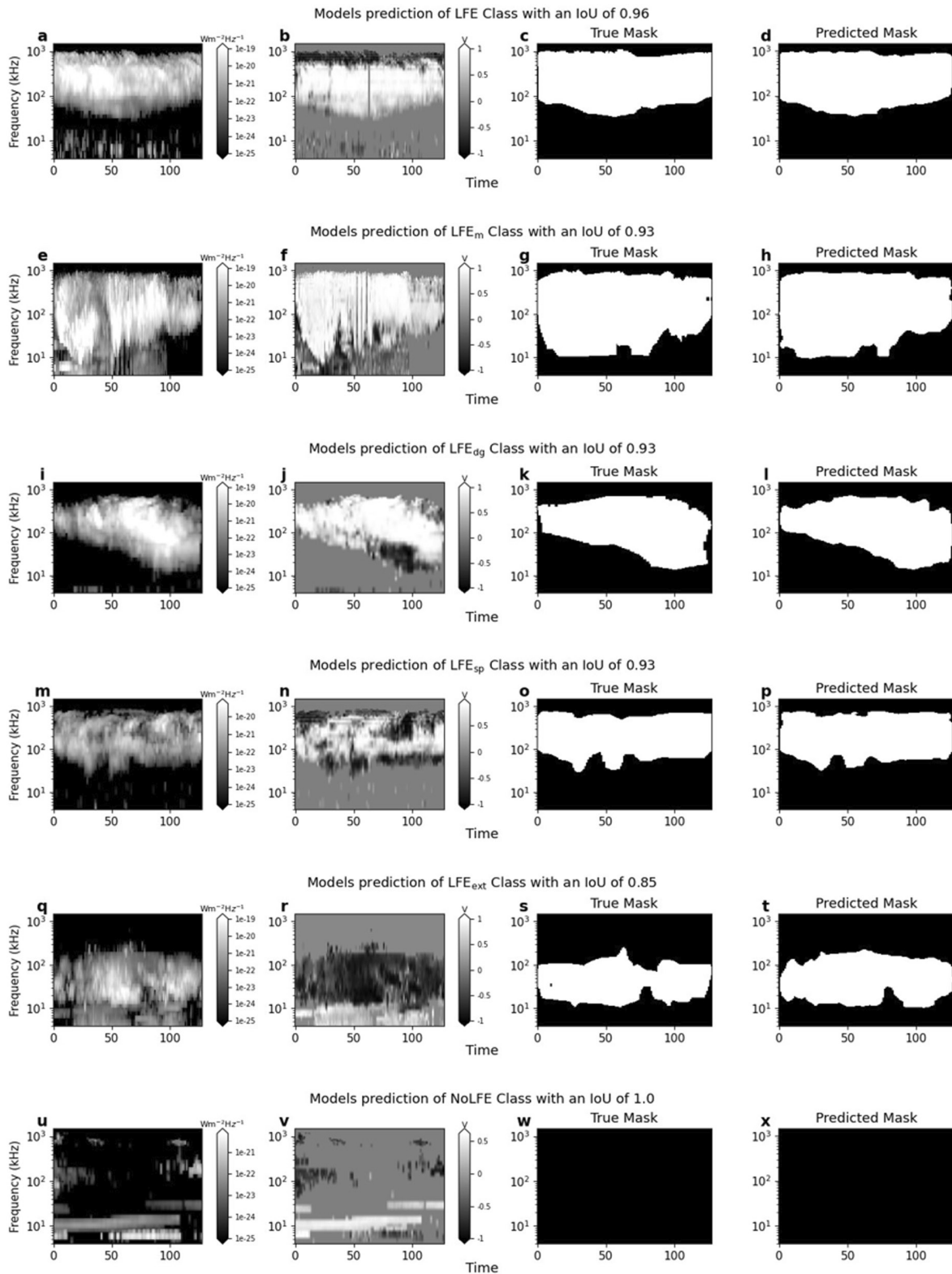


Figure 5. Examples of well classified results from each class in the test set. Shown in this figure are results from six classes, with four panels for each class. Panels (a, b) are spectrograms of flux density and normalized degree of circular polarization, (c) is the ground truth mask of the corresponding spectrogram and (d) is a mask showing the model's prediction. A title on each row indicates the image class.

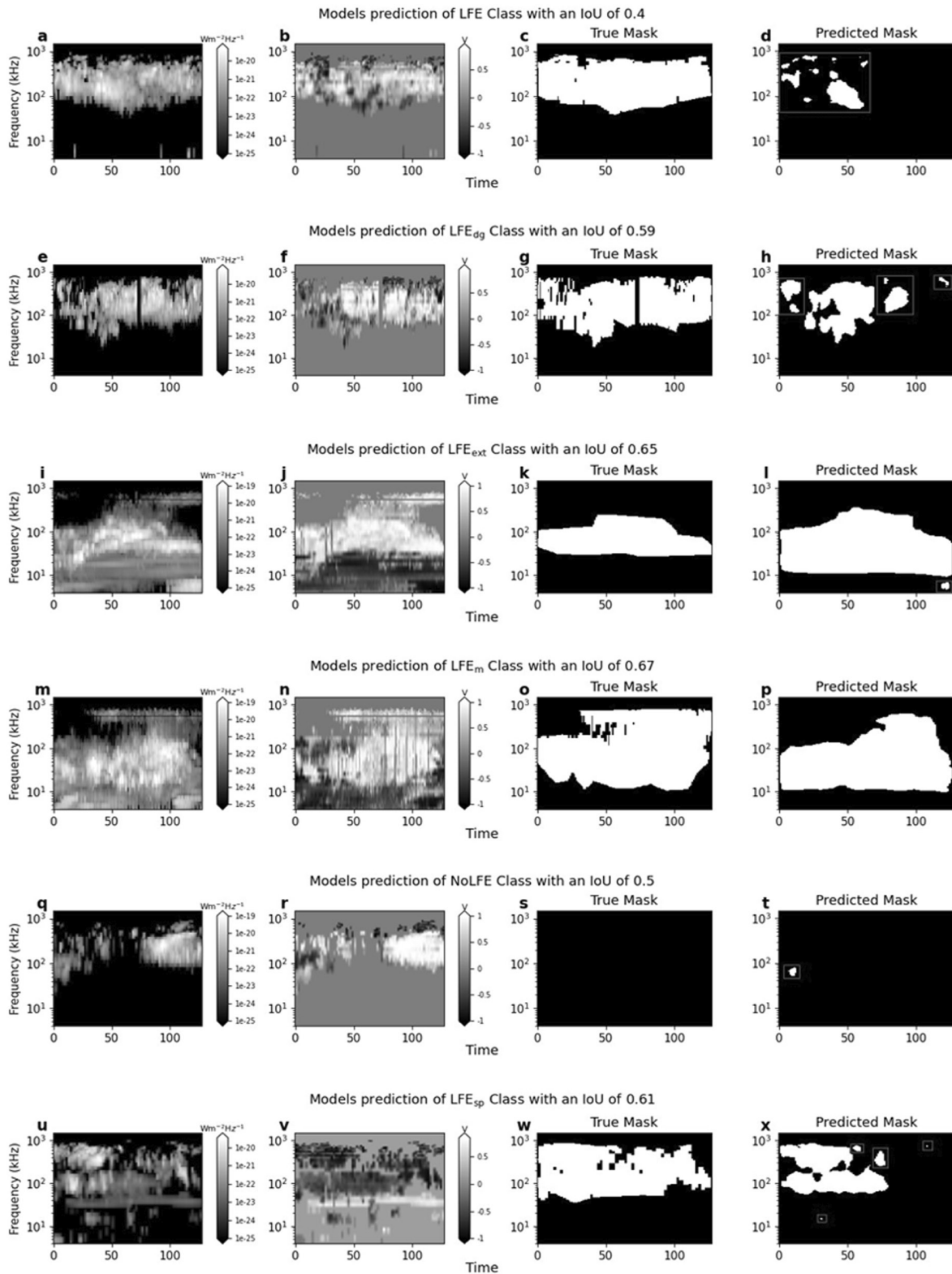


Figure 6. Examples of poorly classified results from each class in the test set. Shown in this figure are results from six classes, with four panels for each class. Panels (a, e, i, m, and u) and (b, f, j, n, and v) are spectrograms of flux density and normalized degree of circular polarization, respectively, panels (c, q, k, o, and w) show the ground truth mask of the corresponding spectrogram and panels (d, h, l, p, and x) show the model's prediction. A title on each row indicates the image class. Red boxes are drawn around small clusters of positively classified pixels that are removed in the post processing steps outlined in Section 4.1.

Table 3
Average Metrics per Class for the Training Set, Test Set, and LFE_{sm} Test Set

Class	Count	Mean loss	Standard deviation	Mean accuracy	Standard deviation	Mean IoU	Standard deviation
Training set							
LFE	343	0.19	0.05	0.94	0.03	0.9	0.06
NoLFE	702	0.09	0.09	0.99	0.06	0.95	0.16
LFE _{dg}	79	0.2	0.04	0.94	0.03	0.89	0.04
LFE _{sp}	71	0.22	0.04	0.93	0.03	0.87	0.05
LFE _m	69	0.2	0.03	0.95	0.02	0.9	0.03
LFE _{ext}	25	0.22	0.1	0.93	0.05	0.87	0.07
LFE _{aug1}	50	0.22	0.09	0.92	0.06	0.85	0.11
LFE _{aug2}	50	0.19	0.08	0.94	0.04	0.88	0.08
LFE _{aug3}	50	0.13	0.02	0.97	0.01	0.91	0.05
LFE _{aug4}	50	0.12	0.03	0.97	0.01	0.93	0.03
LFE _{aug5}	44	0.27	0.08	0.9	0.04	0.83	0.06
Test set							
LFE	136	0.19	0.04	0.94	0.03	0.9	0.06
NoLFE	278	0.1	0.15	0.98	0.08	0.93	0.19
LFE _{dg}	32	0.23	0.11	0.93	0.04	0.86	0.09
LFE _{sp}	28	0.22	0.06	0.93	0.03	0.87	0.06
LFE _m	27	0.21	0.08	0.94	0.03	0.89	0.05
LFE _{ext}	10	0.23	0.1	0.92	0.06	0.85	0.08
LFE _{sm} Test set							
LFE _{sm}	164	0.29	0.19	0.9	0.1	0.75	0.22

Note. The mean loss, accuracy, and IoU are calculated by finding the mean of each metric per input value, that is, mean loss is the mean of the loss of each input in the test/training set.

In Figure 6 we can see a mix of possible reasons why the U-Net output may have failed to replicate the training data. One class of examples is where the labeled LFE from the training set is only partially classified (Figures 6d and 6h). These cases are most often associated with the U-Net mistaking radio emission for a standard SKR burst as opposed to an LFE, in cases where the extension to lower frequencies is far less pronounced than in other training set examples. Generally we are happy for the U-Net output to err on the side of being conservative in its selection of LFE candidates, as this gives us confidence that the outputted list of LFEs represents the clearest possible list of events covering the entire Cassini catalog. However, when it finds many isolated clusters of pixels we want to examine further. In the next section we detail several post-processing steps motivated by our domain knowledge of Saturn's radio emission.

4.1. Post-Processing Steps

Upon inspection of the results, it emerged that we frequently observed small, isolated clusters of positive predictions within the output mask. This could occur within an image containing an LFE or without. We can see examples of these small clusters of positive pixels in Figure 6, where we plotted examples of six model inputs from the test set, along with their ground truth and predicted mask. The IoU of each prediction is also listed at the top of each example. Red boxes are drawn around the isolated positive pixels. We can see in Figure 6d, an image with “LFE” class prediction, that the predicted mask contains many isolated clusters of pixels that are correctly classified but are separated by FN pixels in between. Similarly in Figure 6l, showing an example of “LFE_{ext}” class prediction, the majority of the image is well classified but in the bottom right there is a small cluster of FP pixels that is separated from the main cluster of positive pixels that is largely classified correctly. In Figure 6x, the model's prediction of “LFE_{sp}” class, there are four clusters of positive pixels separate from the main cluster. They

vary in size, with three correctly classified and one small cluster in the lower portion of the image incorrectly classified. Figure 6h showing the model's prediction of "LFE_{dg}" class, contains six clusters of isolated pixels. They are all correctly classified but are separate from the main cluster of positive pixels. In Figure 6t we see the model's prediction of a non-LFE image. This image has just one small cluster of FP pixels in the lower portion of the image. We can see that the IoU for this prediction is 0.5, despite the cluster being very small.

The small, isolated clusters of positive pixels do not match the global, long-lasting, physical nature of LFEs. They essentially do not satisfy the criterion of a continuous extension from the main band SKR down to lower frequencies, as they often occur solely in the main band or solely in the lower frequency band. Based on our extensive domain knowledge of the commonly observed radio signatures, we deem it necessary to remove these clusters from the output mask. In order to do this we place a criterion on Δf ($\Delta f = \text{maximum frequency value} - \text{minimum frequency value}$) and also on the minimum frequency value. We placed a minimum Δf threshold of 100 pixels. This is a criterion based on visual observation and the fact that 100 pixels corresponds to less than 30% of the total image height: an LFE would typically span at least 50% so it is a moderate minimum value. We also note that the respective frequency bandwidth of 40–400 kHz and 40–100 kHz correspond to 148 pixels and 60 pixels on the spectrogram image. 100 pixels corresponds to a bandwidth from 40 to 187 kHz. We do not impose a stricter criterion as we want to preserve "LFE_{ext}" which typically does not span the entire main band frequency range. We also convert from pixels to actual frequency values and place a criterion on minimum frequency: minimum frequency must be 100 kHz or less. This means that it must extend down to the edge of the main SKR band at least. We then remove these clusters of pixels that do not satisfy the criterion from the model's predictions. These correspond to examples like those shown in the red boxes in Figure 6.

We apply one further post-processing step, which was to place a fixed lower limit on event duration. We set this value at 10 data points, corresponding to 30 min given that the data are at 3-min time resolution. This removed several tens of events, where the entire event was more akin to an isolated cluster of points than to a significant extended interval of lower frequency radio emission. This 30-min lower limit was also employed by Reed et al. (2018), and is a way of defining a minimum event extension to ensure statistical feasibility.

Upon applying the post processing criteria to the test set predictions, the distribution of the IoU of predictions of the test samples has changed slightly. Before applying the processing criteria, the 25th, 50th, and 75th percentiles of the total IoU of the test set were 0.89, 0.94, and 1.0. After applying the post processing criteria, the 25th, 50th, and 75th percentiles were found to be 0.9, 1.0, and 1.0. It is clear that the post processing criterion has improved the test results. Similarly for the model's training predictions, the 25th, 50th, and 75th percentiles were found to be 0.89, 0.94, and 1.0. After applying the post processing criterion, these values were recalculated as 0.9, 0.94, and 1.0. For the test set, these isolated clusters of positive pixels that do not satisfy the criterion were removed from 79 images with an LFE and 29 images without an LFE. For the training set, they were removed from 285 images with an LFE and 58 images without an LFE. For the images without an LFE that contain the small clusters of pixels, the IoU is dramatically affected. The IoU is an average of the IoU for the LFE class and IoU for the background class. For an image without an LFE, the true mask does not contain any positive pixels and the IoU of the positive class in the image would be zero if the model predicts any positive pixels. Thus, when the average of the IoU of the background class and LFE class is calculated it will always be less than 0.5 if any FP pixels are predicted in a non-LFE image. For this reason, the application of the post-processing step described above dramatically increases the IoU of non-LFE images but would only slightly increase the IoU of LFE images. Since there were a larger proportion of LFE images to non-LFE images that were affected by the post processing criterion, we do not see a dramatic increase in the distribution of IoU after the processing was applied.

4.2. Testing of LFE_{sm} Class

The second testing set consisting of the LFE_{sm} class only was tested on the model. This testing set consists of 164 images in total. The model is not trained using the LFE_{sm} class because it consists of a really moderate extension in frequency and the physical reasons behind this are not understood. It is preferable to solely use the well defined LFEs to train the model. However, we would like to understand how the model treats LFEs with a moderate extension and so we use the samples in this class as a testing set. In Table 3, the mean of the loss and performance metrics are listed, as well as their standard deviation. Generally, the model does not predict the LFE_{sm} as well as the other classes present in the train and test set. We see a higher mean loss for the LFE_{sm} set than for the other classes in the training and test set, as well as a higher standard deviation. The mean accuracy is slightly lower,

Table 4
Normalized Confusion Matrix Computed From Pixel-To-Pixel Comparison of the Ground Truth and the Model's Prediction of the Data Recorded in 2006

		True	
		LFE	No-LFE
Predicted	LFE	0.91	0.09
	No-LFE	0.02	0.98

and the standard deviation is higher than that of the classes in the train and test set. The mean IoU is also lower with a higher standard deviation than the other classes. Looking at the distribution of the IoU of the model's predictions of the LFE_{sm} set, the 25th, 50th, and 75th percentiles are 0.61, 0.87, and 0.91. After applying the post processing steps outlined in Section 4.1, the 25th, 50th, and 75th percentiles are calculated as 0.60, 0.87, and 0.91.

4.3. Application to the Full Radio Data Set

4.3.1. Input Method

In order to apply the model to the full Cassini radio data set, the data were split into arrays with a time range of 6 hr and 24 min. This corresponds to 128 pixels in width since the time resolution of the radio data is 3 min. The end of each array (aside from the last) overlaps in time with the subsequent ones by 2 hr and 45 min, which corresponds to 55 pixels in width. Every array aside from the first and last overlaps with the previous and subsequent array by 55 pixels on each side, such that only the center 18 pixels will not be overlapping. The first and last arrays will only overlap with the subsequent/previous by 55 pixels. The model performs a prediction on each array and then we find the mean value at each pixel of the overlapping segments.

4.3.2. Testing on One Year of Labeled Data

In order to test the performance of this method, we split the data recorded in the year 2006 into arrays as described. Since this year is fully labeled, we can directly compare the ground truth of the entire year to the model's prediction. After this is completed, we analyzed the results by computing the IoU and a confusion matrix. For this whole year, we calculated an IoU of 0.818. The normalized confusion matrix is computed by comparing the predicted pixels to the ground truth pixels and computing the counts of TP, FP, TN, and FN. In Table 4, the confusion matrix is shown. The counts are normalized by dividing by the total counts in each row such that TP + FP = 1 and TN + FN = 1. In Figure 7, there are four examples of model predictions using the specified input method for data in 2006. For each example, there are three spectrograms with colourbars showing: flux density normalized to 1 AU, degree of polarization and a ground truth binary mask indicating where the LFEs occur within the given time range. The model's prediction, converted from a mask to frequency time coordinates, is indicated with an orange polygon on each spectrogram.

4.3.3. Converting Mask to Polygon

In order to extract the frequency time coordinates of the LFEs, we must find the coordinates of the edges of the LFE predictions in the binary mask. First, the predicted mask, which consists of probabilities at each pixel, is converted to a binary mask by setting values above the optimized threshold (0.65) to 1 and below to zero. Following this, we use the function `findContours` from the python library `OpenCV`. This function returns the coordinates of the curve along a boundary, joining points with the same value. In this case it is the boundary between the pixels with a value of zero and pixels with a value of 1. After finding the coordinates of the contours found in the predicted binary mask, we need to convert these coordinates from positions in an array to actual frequency time coordinates. We map the contour coordinates back to frequency time by finding their positions in the actual frequency time array.

4.3.4. Results of Full Data Set

We find the predictions of the full Cassini data set by inputting the data as described in Section 4.3.1. Then the post processing steps were applied to the predicted mask. We find the frequency-time coordinates of the contours found in the predicted mask. In total 4,874 LFEs were found. Of these 4,874, 3,166 are of type "LFE," 839 are of type "LFE_m" and 869 of type "LFE_{sm}." These types are not outputted by the U-Net, but rather are determined by subsequent examination of the duration (>11 hr for LFE_m), or the lower frequency bounds (for LFE_{sm}). The "LFE" class thus likely contains examples which are from subclasses such as LFE_{dg} (for datagaps), LFE_{ext} (for extinctions seen from higher latitudes) and LFE_{sp} (for sparse emission). The detailed examination of these sub-groups is outside the scope of this paper, but the list of all predicted LFE cases is made available on Zenodo as a community resource for anyone wishing to explore cases in more detail.

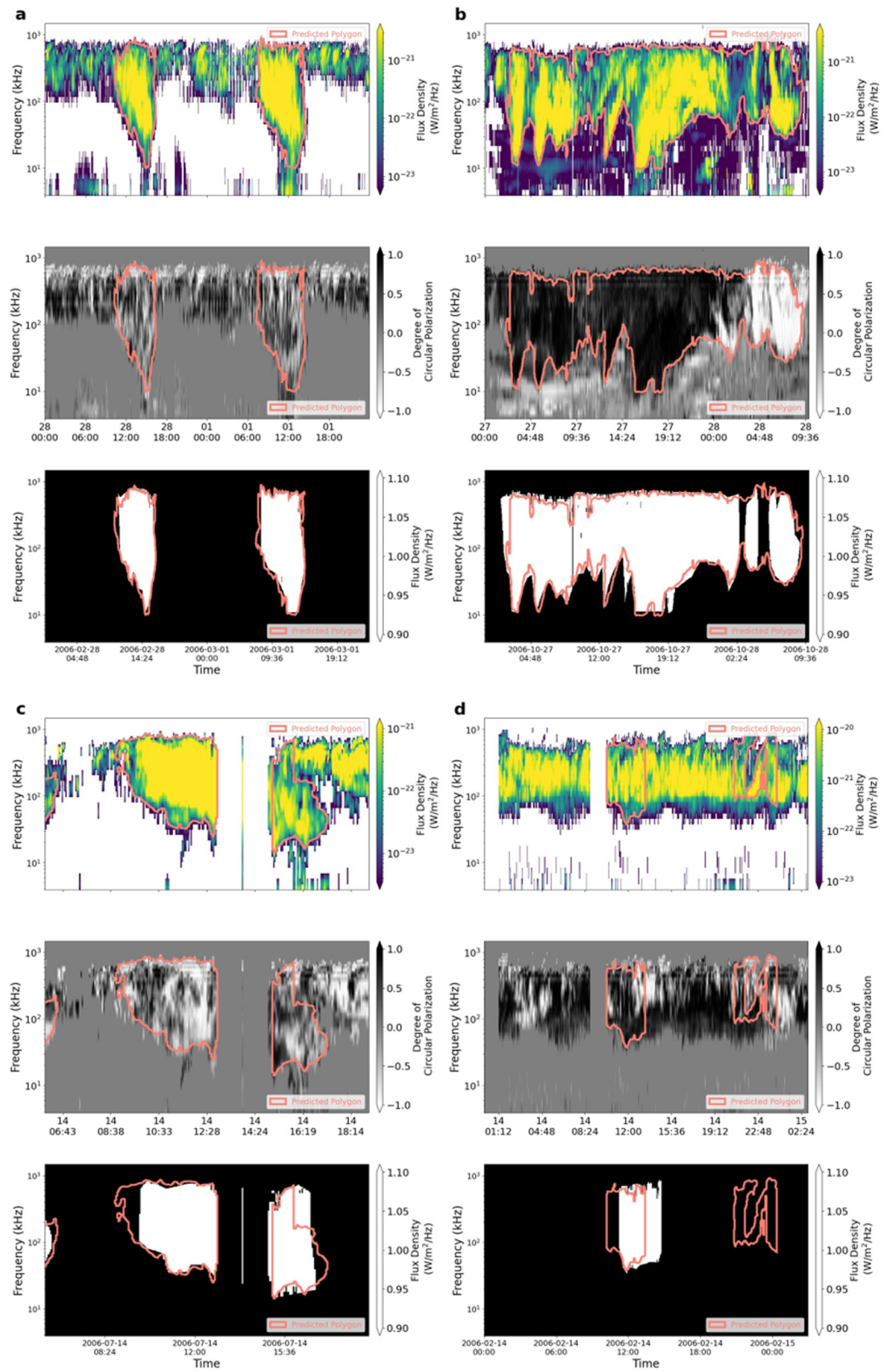


Figure 7. Examples of model predictions using the input method described in Section 4.3.1. In panels (a–d), we see four examples of dynamic spectra (with colourbars showing flux density normalized to 1 AU and degree of polarization) and the corresponding ground truth mask plotted below. Overplotted in orange is the model’s prediction, converted from binary mask to frequency-time coordinates.

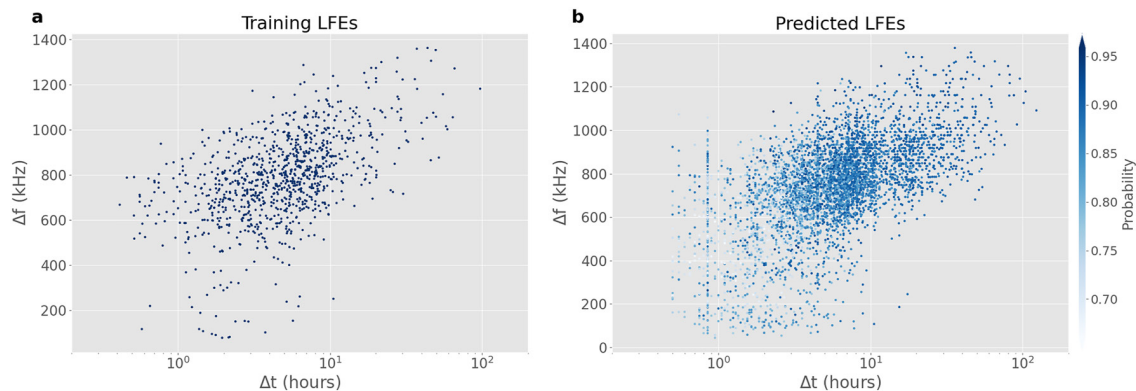


Figure 8. Scatter plots of delta f (in kHz) versus delta t (in hours) for (a) Low Frequency Extensions (LFEs) present in the training set and (b) LFEs predicted by the model with each point colored according to the average probability of pixels occurring within the LFE contour.

Along with the frequency-time coordinates for each LFE, we calculate the mean value of the predicted probabilities found at each pixel within the contour. This is useful as a flag for the confidence of the model's prediction for each LFE. In Figure 8, we display a two panel plot showing Δf (in kHz) versus Δt (in hours) for the training LFEs in Figure 8a and for the model's predicted LFEs in Figure 8b. The points in Figure 8b are colored according to their average probability. We can see that the relationship between Δf and Δt appears to be linear in both cases. In addition, Figure 8b shows that LFEs with a high average probability tend to coincide with LFEs of higher frequency extension and duration. In Figure 9, six examples of the model's prediction are shown. There are two panels for each example, both containing a spectrogram for the given time range with the first panel displaying a colourbar of flux density normalized to 1 AU and the second panel with a colourbar displaying degree of circular polarization. The model's prediction of the LFE in frequency time coordinates is overplotted with an orange line in each panel.

In Figure 10 we repeat the format of Figure 1, exchanging the training LFEs for those predicted by the model. As before, Figure 10a shows Cassini's latitudinal coverage (right-hand axis) from 2004 day 001–2017 day 255. Overplotted in orange is a histogram with a bin size of 50 days of LFE occurrence over time. In Figure 10b, the latitude versus local time coverage of each of Cassini's orbits is plotted in gray with periods of predicted LFEs overplotted in orange. From Figure 10a, we can see that LFEs are continuously detected. From 2004 until mid-2009, counts consistently reach values above 50 (per 50 days). From mid-2009 to mission end, counts tend to lie below 50 aside from several peaks located at \sim mid 2012, mid 2015, and late 2016. In Figure 10b, we can see that LFEs are predicted from virtually all spacecraft latitude and local time positions.

5. Interpretation and Summary

With the benefit of domain knowledge, and a moderate amount of manual labeling, we have conducted a supervised learning approach to identify LFEs of Saturn radio emission in the 13-year Cassini/RPWS data set. We have used a modified U-Net architecture which was suitable because it allows for semantic segmentation without a large training set. The model was trained on a set of 1,533 images (996 training and 537 validation) which consisted of images with an LFE and without, along with augmented images as outlined in Section 3.3. After applying a post processing step to remove small clusters of positive pixels that do not correspond physically to an LFE, we reached median IoU values of 0.97 and 0.98 for the testing and training set, respectively. The model made predictions on the entire Cassini/RPWS data set by inputting images with overlapping start and end times and computing the average of the model prediction for the overlapping segments. The output is a list of all LFEs predicted using the method outlined in this paper, which consists of 4,874 LFEs in total. Of these 4,874, 3,166 are of type “LFE,” 839 are of type “LFE_m” and 869 of type “LFE_{sm}.” Comparison of Δf versus Δt of the training LFEs and the predicted LFEs show similar behavior. For both groups, the relationship between Δf versus Δt is approximately linear. We also note that generally the model makes predictions with higher probability for LFEs with higher values of Δf and Δt . Analysis of predicted LFE occurrence over time shows that LFEs are predicted at all stages of the mission, with a higher occurrence rate from 2004 to mid-2009. The exact frequency time coordinates of each LFE have been extracted and made available for use across the scientific community. The large

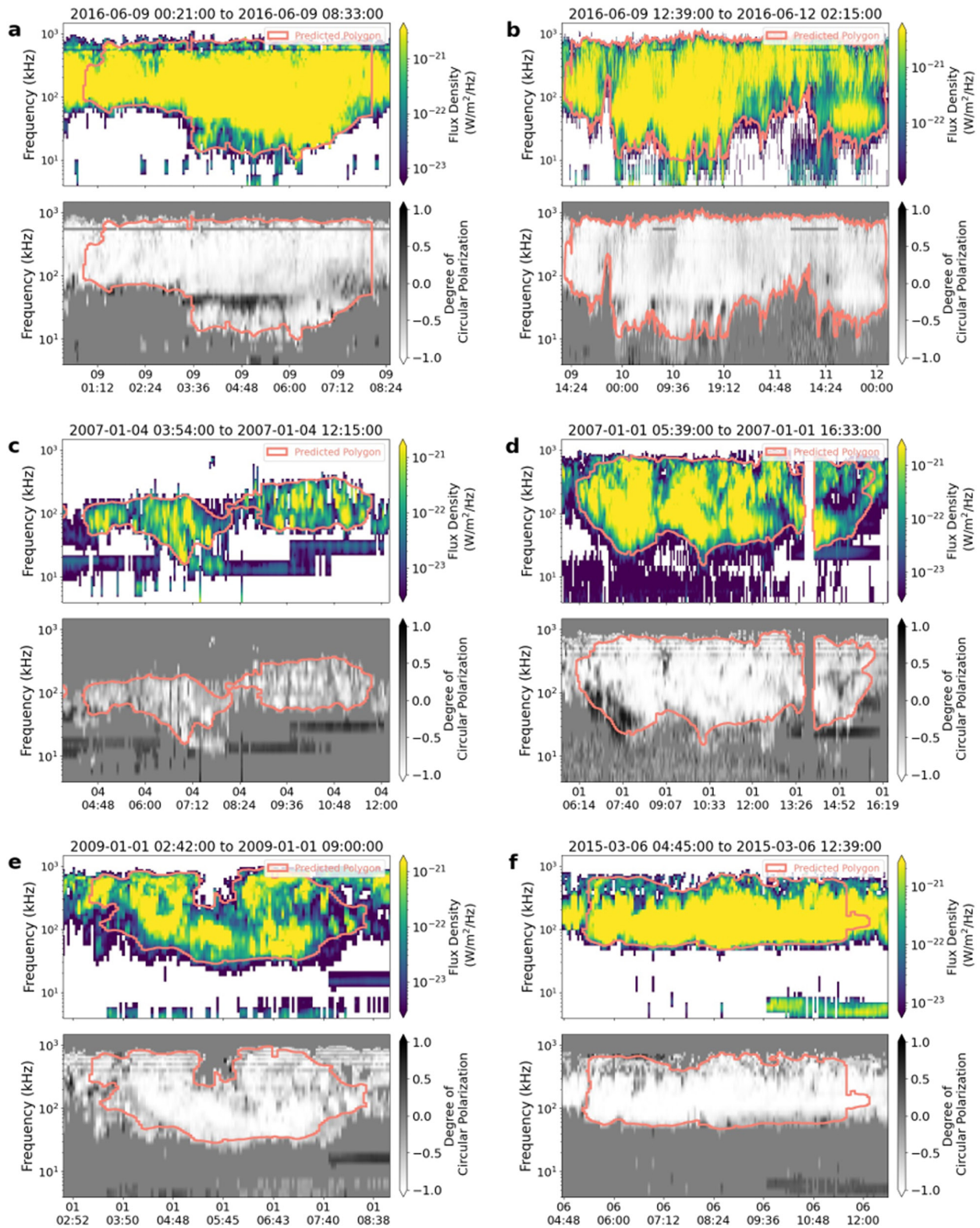


Figure 9. Six examples of model's prediction on unseen data from the Cassini/Radio and Plasma Wave Science radio data set. Shown for each example are the model inputs of spectrograms with colourbars showing flux density normalized to 1 AU and degree of circular polarization, along with the model's prediction in frequency-time coordinates overplotted with an orange line. For each case, the Low Frequency Extension is centered on the spectrogram.

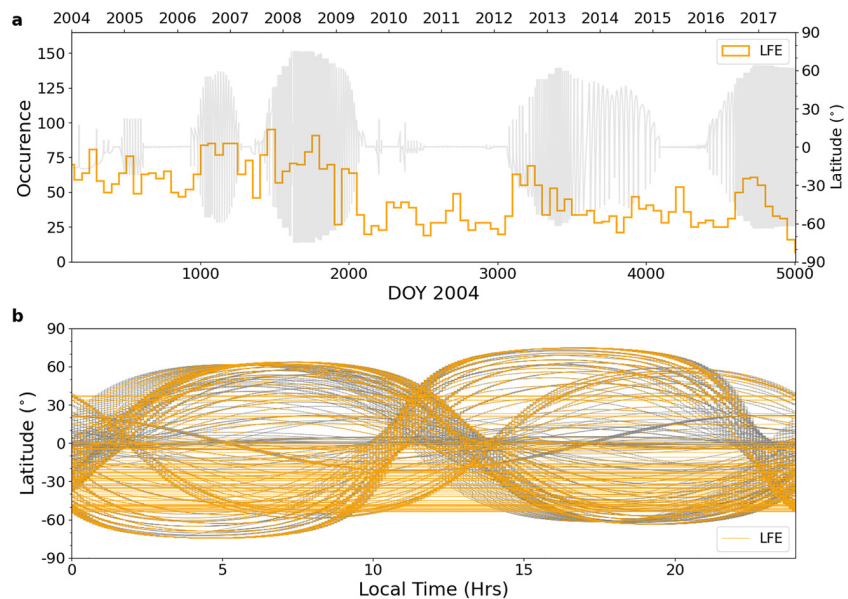


Figure 10. (a) Histograms for occurrence of Low Frequency Extension (LFE) predictions as a function of time, with a bin size of 50 days. We plot Cassini's latitude from day 1 of 2004 to day 255 of 2017 in the background in gray (with y-axis shown on the right). (b) Plot of spacecraft latitude (°) versus Local Time (hours) for the same time period as in panel (a), with periods of predicted LFEs overlaid in orange.

benefit of curating this list is for statistical studies and to explore the breadth of radio signatures that arise from complex magnetospheric dynamics.

Data Availability Statement

The catalog of the frequency-time coordinates of all LFEs detected using this method is available at <https://zenodo.org/record/8314868>, O'Dwyer, Jackman, Domijan, and Lamy (2023), in Time Frequency Catalogue (TFCAT) format (Cecconi et al., 2023). The Cassini/RPWS (Gurnett et al., 2004) data used in this study were processed according to Lamy et al. (2008) and can be found at Lamy et al. (2009). The Cassini trajectory data were recorded by the Cassini MAG instrument (Dougherty et al., 2004) and can be found at Dougherty et al. (2019). Figure 3 was made using python library `visualker` found at Gavrikov (2020). The code used to train the U-Net model and carry out the subsequent analysis can be found at https://github.com/elodwyer1/Unet_Application_to_Saturn_Kilometric_Radiation.

Acknowledgments

E. P. O'Dwyer's and C.M. Jackman's work at DIAS was supported by Science Foundation Ireland Grant 18/FRL/6199. L. Lamy acknowledges support from CNES and CNRS/INSU national programs of planetology (PNP) and heliophysics (PNST). We acknowledge helpful discussions with Daragh Hollman regarding code implementation and testing.

References

- Bunce, E. J., Cowley, S. W. H., Wright, D. M., Coates, A. J., Dougherty, M. K., Krupp, N., & Rymer, A. M. (2005). In situ observations of a solar wind compression-induced hot plasma injection in Saturn's tail. *Geophysical Research Letters*, 32(20), L20S04. <https://doi.org/10.1029/2005GL022888>
- Cecconi, B., Louis, C. K., Bonnin, X., Loh, A., & Taylor, M. B. (2023). Time-frequency catalogue: JSON implementation and python library. *Frontiers in Astronomy and Space Sciences*, 9, 1049677. <https://doi.org/10.3389/fspas.2022.1049677>
- Cecconi, B., & Zarka, P. (2005). Direction finding and antenna calibration through analytical inversion of radio measurements performed using a system of two or three electric dipole antennas on a three-axis stabilized spacecraft. *Radio Science*, 40(3), RS3003. <https://doi.org/10.1029/2004RS003070>
- Chollet, F., et al. (2015). Keras [Software]. GitHub. Retrieved from <https://github.com/fchollet/keras>
- Dougherty, M., Kellock, S., Slootweg, A., Achilleos, N., Joy, S., & Mafi, J. (2019). Cassini orbiter mag calibrated summary averaged v2.0 [Dataset]. NASA Planetary Data System. <https://doi.org/10.17189/1519602>
- Dougherty, M., Kellock, S., Southwood, D., Balogh, A., Smith, E., Tsurutani, B., et al. (2004). The Cassini magnetic field investigation. *Space Science Reviews*, 114(1–4), 331–383. <https://doi.org/10.1007/s11214-004-1432-2>
- Galopeau, P. H. M., & Lecacheux, A. (2000). Variations of Saturn's radio rotation period measured at kilometer wavelengths. *Journal of Geophysical Research*, 105(A6), 13089–13101. <https://doi.org/10.1029/1999JA005089>
- Gavrikov, P. (2020). visualker [Software]. GitHub. Retrieved from <https://github.com/paulgavrikov/visualker>
- Glorot, X., & Bengio, Y. (2010). Understanding the difficulty of training deep feedforward neural networks. *Journal of Machine Learning Research - Proceedings Track*, 9, 249–256.

- Gurnett, D. A., Kurth, W. S., Kirchner, D. L., Hospodarsky, G. B., Averkamp, T. F., Zarka, P., et al. (2004). The Cassini radio and plasma wave investigation. *Space Science Reviews*, *114*(1–4), 395–463. <https://doi.org/10.1007/s11214-004-1434-0>
- Jackman, C. M., Lamy, L., Freeman, M. P., Zarka, P., Cecconi, B., Kurth, W. S., et al. (2009). On the character and distribution of lower-frequency radio emissions at Saturn and their relationship to substorm-like events. *Journal of Geophysical Research*, *114*(A8), A08211. <https://doi.org/10.1029/2008JA013997>
- Kaiser, M. L., Desch, M., Warwick, J., & Pearce, J. (1980). Voyager detection of nonthermal radio emission from Saturn. *Science*, *209*(4462), 1238–1240. <https://doi.org/10.1126/science.209.4462.1238>
- Kaiser, M. L., & Desch, M. D. (1984). Radio emissions from the planets Earth, Jupiter, and Saturn. *Reviews of Geophysics*, *22*(4), 373–384. <https://doi.org/10.1029/RG022i004p00373>
- Lamy, L. (2017). The Saturnian kilometric radiation before the Cassini Grand Finale. In G. Fischer, G. Mann, M. Panchenko, & P. Zarka (Eds.), *Planetary radio emissions viii* (pp. 171–190). <https://doi.org/10.1553/PRE8s171>
- Lamy, L., Cecconi, B., & Zarka, P. (2009). Cassini/RPWS/HFR LESIA/KRONOS SKR data collection [Dataset]. PADC. <https://doi.org/10.25935/zkxb-6c84>
- Lamy, L., Schippers, P., Zarka, P., Cecconi, B., Arridge, C. S., Dougherty, M. K., et al. (2010). Properties of Saturn Kilometric Radiation measured within its source region. *Geophysics Research Letters*, *37*(12), L12104. <https://doi.org/10.1029/2010GL043415>
- Lamy, L., Waters, J., & Louis, C. (2023). Comparative visibility of planetary auroral radio emissions and implications for the search for exoplanets. In G. Fischer, C. M. Jackman, C. K. Louis, A. H. Sulaiman, & P. Zucca (Eds.), *Planetary, solar and heliospheric radio emissions ix*.
- Lamy, L., Zarka, P., Cecconi, B., Prangé, R., Kurth, W. S., & Gurnett, D. (2008). Saturn kilometric radiation: Average and statistical properties. *Journal of Geophysical Research*, *113*(A7), A07201. <https://doi.org/10.1029/2007ja012900>
- Louis, C. K., Jackman, C. M., Mangham, S. W., Smith, K. D., O'Dwyer, E. P., Empey, A., et al. (2022). Space labelling tool version 2.0.0 (v2.0.0) [Software]. Zenodo. <https://doi.org/10.5281/zenodo.6886528>
- Menietti, J. D., Mutel, R. L., Schippers, P., Ye, S.-Y., Gurnett, D. A., & Lamy, L. (2011). Analysis of Saturn Kilometric Radiation near a source center. *Journal of Geophysical Research*, *116*(A12), A12222. <https://doi.org/10.1029/2011JA017056>
- Morioka, A., Miyoshi, Y., Tsuchiya, F., Misawa, H., Yumoto, K., Parks, G. K., et al. (2008). AKR breakup and auroral particle acceleration at substorm onset. *Journal of Geophysical Research*, *113*(A9), A09213. <https://doi.org/10.1029/2008JA013322>
- Mutel, R. L., Menietti, J. D., Gurnett, D. A., Kurth, W., Schippers, P., Lynch, C., et al. (2010). CMI growth rates for Saturnian kilometric radiation. *Geophysical Research Letters*, *37*(19), L19105. <https://doi.org/10.1029/2010GL044940>
- O'Dwyer, E. P., Jackman, C., Domijan, K., & Lamy, L. (2023). Image-based classification of Intense radio bursts from spectrograms: An application to Saturn Kilometric Radiation [Dataset]. Zenodo. <https://doi.org/10.5281/zenodo.8314868>
- O'Dwyer, E. P., Jackman, C. M., Domijan, K., Lamy, L., & Louis, C. K. (2023a). A selection of low frequency extensions of Saturn kilometric radiation. In C. K. Louis, C. M. Jackman, G. Fischer, A. H. Sulaiman, P. Zucca & Dublin Institute for Advanced Studies (Eds.), *Planetary, solar and heliospheric radio emissions IX*. <https://doi.org/10.25546/103103>
- O'Dwyer, E. P., Jackman, C. M., Domijan, K., Lamy, L., & Louis, C. K. (2023b). Selection of Low frequency extensions of Saturn kilometric radiation detected by Cassini/RPWS [Dataset]. Zenodo. <https://doi.org/10.5281/zenodo.8074022>
- Reed, J. J., Jackman, C. M., Lamy, L., Kurth, W. S., & Whiter, D. K. (2018). Low-frequency extensions of the Saturn kilometric radiation as a proxy for magnetospheric dynamics. *Journal of Geophysical Research: Space Physics*, *123*(1), 443–463. <https://doi.org/10.1002/2017JA024499>
- Ronneberger, O., Fischer, P., & Brox, T. (2015). U-Net: Convolutional networks for biomedical image segmentation. arXiv e-prints, arXiv:1505.04597.
- Wu, C., & Lee, L. (1979). A theory of the terrestrial kilometric radiation. *The Astrophysical Journal*, *230*, 621–626. <https://doi.org/10.1086/157120>

0.4 Chapter III

This chapter consists of an article published in the Planetary, Solar and Heliospheric Radio Emissions IX conference proceedings titled 'Using crossings of Saturn's magnetospheric boundaries to explore the link between upstream conditions and radio emission'. I contributed to this article by providing a list of LFEs to be used as a comparison to a list of Cassini's magnetospheric boundary crossings. I contributed to discussions surrounding the article regarding the definition of LFEs.

1 USING CROSSINGS OF SATURN'S 2 MAGNETOSPHERIC BOUNDARIES TO 3 EXPLORE THE LINK BETWEEN UPSTREAM 4 CONDITIONS AND RADIO EMISSION

5 C.M. Jackman¹, E.P. O'Dwyer¹, C.K. Louis¹, A.R. Fogg¹,
J.E. Waters², and L. Lamy³

6 Abstract

7 Saturn has several components to its radio emission which can change in re-
8 sponse to varying solar wind and magnetospheric conditions. These radio compo-
9 nents include the Saturn Kilometric Radiation (SKR), a cyclotron maser instability-
10 generated emission which occasionally displays Low Frequency Extensions (LFEs),
11 some of which can last for more than a planetary rotation. We utilise a list of all
12 magnetopause and bow shock crossings by Cassini during its 13-year tour of the
13 Saturn system to explore how measurements of the upstream and near-boundary
14 conditions at Saturn can inform our knowledge of the solar wind driving and its
15 links to radio emission. Solar wind intervals give a direct measure of the upstream
16 environment to compare against. Furthermore, bow shock and magnetopause cross-
17 ings can be used in concert with boundary models to infer the upstream solar wind
18 dynamic pressure at the time of crossings. We show several case studies which elu-
19 cidate the timeline of solar wind-magnetosphere-ionosphere coupling at Saturn and
20 outline open questions and future avenues for exploration.

21 1 Introduction

22 Saturn's radio emissions were first sampled by the Voyager-1 spacecraft in 1980 (Kaiser
23 et al., 1980), and our understanding of them significantly developed during the 13-year
24 exploration of the near-Saturn system by the Cassini spacecraft which had a Radio and

¹School of Cosmic Physics, DIAS Dunsink Observatory, Dublin Institute for Advanced Studies (DIAS),
Dublin 15, Ireland #1

²Department of Physics and Astronomy, University of Southampton, Highfield Campus, Southampton,
SO17 1BJ, UK #2

³LAM, Pytheas, Aix Marseille Universite, CNRS, CNES, 38 Rue Frederic Joliot Curie, 13012 Marseille,
France #3

25 Plasma Wave Science (RPWS) instrument on board (Gurnett et al., 2004). The strongest
 26 component of Saturn’s radio emissions is called the Saturn Kilometric Radiation (SKR),
 27 a cyclotron maser instability (CMI)-generated emission with a spectrum extending from
 28 ~ 2 kHz to 1.2 MHz, and a broad peak generally located between ~ 100 to 400 kHz.
 29 This emission is highly circularly/elliptically polarized which facilitates its identification
 30 among other kronian or solar radio emissions (e.g. Kaiser & Desch, 1984; Lamy et al.,
 31 2008a; Lamy, 2017).

32 It has long been postulated that there is a link between Saturn’s radio emissions and the
 33 upstream solar wind conditions. Studies with Voyager data found a correlation between
 34 SKR intensity and interplanetary magnetic field (IMF) strength (Desch & Rucker, 1983)
 35 while more recent work with Cassini showed that the solar wind speed can be correlated
 36 with the period of the SKR (Zarka et al., 2007). A statistical study which compared
 37 various upstream parameters to SKR intensity found the strongest correlation with solar
 38 wind dynamic pressure (Taubenschuss et al., 2006). It appears there can be a finite lag
 39 between a change in upstream conditions and a response from the SKR. This response can
 40 take the form of (i) an intensification of the emission (Jackman et al., 2005b; Thomsen
 41 et al., 2019; Cecconi et al., 2022), (ii) a change in the regular pulsing of the emission
 42 (Badman et al., 2008), (iii) a change in the morphology of the emission, specifically an
 43 extension of the emission to lower frequencies (Bunce et al., 2005; Jackman et al., 2009;
 44 Reed et al., 2018). These so-called Low Frequency Extensions (LFEs) are interpreted as
 45 a growth/movement of the radio sources to higher altitudes along field lines, with the
 46 consequence of lower frequency emission being observed. LFEs are thought to be driven
 47 by solar wind compressions and also linked to dramatic magnetotail reconfiguration events
 48 which increase the precipitation of energetic particles into the auroral zone. LFEs have a
 49 well-studied terrestrial analogue in the extension of Auroral Kilometric Radiation (AKR)
 50 emission at Earth (Morioka et al., 2007).

51 One of the main challenges at the outer planets is the lack of an upstream monitor to pro-
 52 vide context for magnetospheric observations. At Saturn we have a rich dataset of 13 years
 53 of quasi-continuous radio observations from the Cassini spacecraft which bring potential
 54 to probe the site of particle acceleration and to act as a remote proxy for conditions which
 55 drive dynamics in the magnetosphere. In this work we pursue several approaches to quan-
 56 tifying the link between the upstream solar wind conditions and Saturn’s radio response.
 57 In section 2 we introduce the data set and associated visibility constraints, in section 3 we
 58 examine direct and indirect methods for exploring solar wind-radio connection. Section 4
 59 presents a summary and future perspectives.

60 **2 Dataset and visibility constraints**

61 The Cassini spacecraft orbited Saturn from July 2004 to September 2017, and the Cassini
 62 Radio Plasma Wave Science (RPWS) High Frequency Receiver (HFR) took data quasi-
 63 continuously for this time, recording radio electric signals from 3.5 kHz to 16 MHz using
 64 two or three electric antennas with various operation modes affecting the time-frequency
 65 coverage (Gurnett et al., 2004). Goniopolarimetric inversions of 2- and 3-antenna mea-
 66 surements then provided the wave Stokes parameters, including the flux density S and the

67 degree of circular polarization V . This instrument allows for reconstruction of the absolute
68 flux density and polarisation of the observed radio waves (Cecconi & Zarka, 2005). For the
69 purpose of analyzing solely the SKR component on long timescales, (Lamy et al., 2008a)
70 constructed a cleaned calibrated dataset made of regular time-frequency arrays for the
71 quantities S (expressed in $W/m^2/Hz$ and normalized to 1 AU) and V ($= \pm 1$ for purely
72 LH/RH circularly polarized waves). These arrays consist of 48 frequency channels (24
73 logarithmically spaced channels between 3.5 and 300 kHz and 24 linearly spaced channels
74 between 350 and 1500 kHz) with a native time resolution of 180 sec. For the purpose of
75 this study, we used a updated version of this dataset with a time resolution of 90 sec.

76 In addition to the remotely sensed radio emission, in this work we also employ data from
77 the Cassini magnetometer instrument (Dougherty et al., 2004) and the Cassini Plasma
78 Spectrometer (CAPS) (Young et al., 2004) (where available). During Cassini's excursions
79 outside the magnetosphere, these datasets describe the IMF and solar wind plasma pa-
80 rameters. These data were used by (Jackman et al., 2019) to determine the timing of
81 magnetopause and bow shock crossings during the Cassini mission. Boundary crossings
82 were characterised by sharp changes in the character of field (amplitude, level of fluc-
83 tuation, orientation), and plasma (density, temperature) properties and the intervals in
84 between magnetopause and bow shock crossings represent a significant amount of time
85 spent in Saturn's turbulent magnetosheath. This boundary crossing list has since been
86 updated with minor corrections and then full set of 2118 magnetopause and 1247 bow
87 shock crossings is available here: (Jackman, 2022). In this work, we combine the bound-
88 ary crossing times with models of the magnetopause (Kanani et al., 2010) and bow shock
89 (Went et al., 2011) to infer the upstream solar wind dynamic pressure at the times of
90 crossings by tracking back to the nose standoff distance. These dynamic pressure val-
91 ues give an instantaneous snapshot of conditions without the ability to account for rapid
92 boundary motion.

93 2.1 Spacecraft coverage

94 Figure 1 shows the trajectory of the Cassini spacecraft from Saturn Orbit Insertion (SOI)
95 in July 2004 to mission end in September 2017. Cassini's initial approach to Saturn
96 was from the dawn flank and the first long capture orbit was also out towards dawn,
97 with subsequent orbits covering all local times and a wide range of latitudes. There are
98 magnetopause and bow shock crossings near the nose, and dawn/dusk flanks, and this
99 diverse local time coverage is critical for comparing the viewing of radio sources from
100 different observation points.

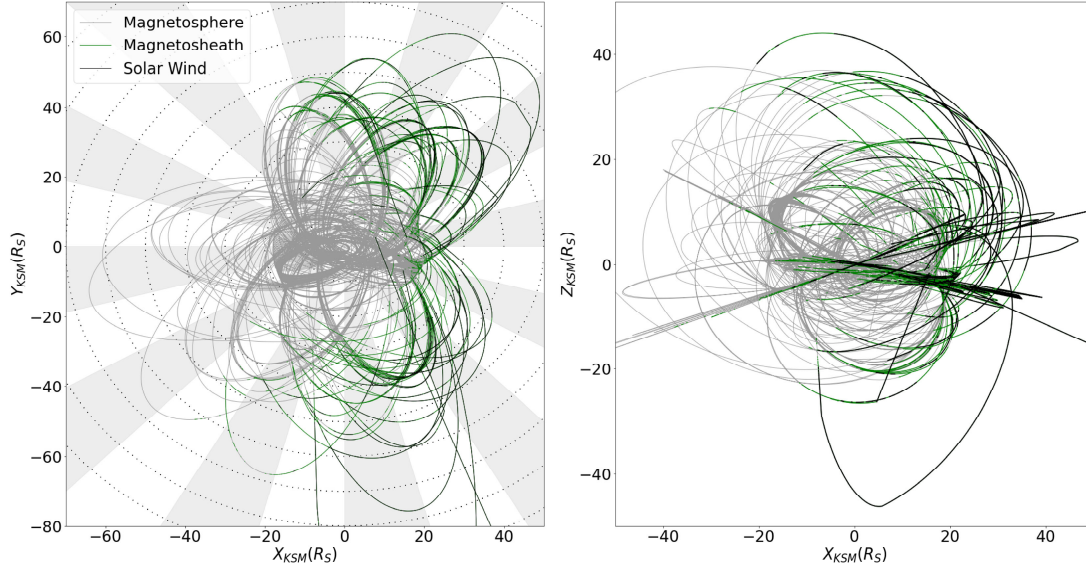


Figure 1: Trajectory of the Cassini spacecraft from Saturn Orbit Insertion in July 2004 to mission end in September 2017. The grey lines show the trajectory within the magnetosphere, green within the magnetosheath, and black in the solar wind. Data are shown in the Kronian Solar Magnetospheric (KSM) co-ordinate system, where the x axis coincides with the direction of the Sun, the x-z plane contains the planetary dipole axis, and the y component is azimuthal, positive toward dusk. 1a) shows the x-y KSM view, and 1b) shows the x-z KSM view. Alternating grey and white markings in 1a) denote hour-wide local time sectors. Concentric dotted circles are drawn every $10 R_S$.

101 2.2 Visibility of Saturn's radio sources

102 Before interpreting any observed radio emissions, it is critical to take the viewing con-
 103 ditions into account. As mentioned above, SKR is CMI-generated, and it is beamed in
 104 hollow cones from source regions near the auroral zone. Previous studies at Saturn (Lamy
 105 et al., 2008b; Cecconi et al., 2009; Lamy et al., 2009; Kimura et al., 2013; Reed et al., 2018;
 106 Nakamura et al., 2019) have shown that the beamed nature of CMI-generated radio emis-
 107 sions and the constrained radio source locations results in emission which is preferentially
 108 observed from restricted sectors in local time and latitude. At Saturn, goniopolarimetric
 109 studies have revealed the typical location of radio sources in the morning-to-noon sector
 110 at high latitudes (Warwick et al., 1981; Lecacheux & Genova, 1983; Galopeau et al., 1995).
 111 In practice, this means that the most intense radio powers are observed whenever the most
 112 intense radio sources can be observed, typically from a two-peak window in Local Time
 113 separated from the source flux tube by several hours LT (Cecconi et al., 2009; Andrews

114 et al., 2010; Lamy et al., 2013).

115 In addition to viewing constraints associated with the local time of the observer, there are
116 also latitudinal influences on the measured radio signal. Lamy et al. (2008b) showed that
117 the SKR spectrum maximizes whenever observed from $20 - 30^\circ$ latitude, while extinctions
118 at both highest and lowest frequencies are seen from very high latitudes. Such features are
119 correctly reproduced from simulations. Nakamura et al. (2019) examined the full Cassini
120 near-Saturn dataset from 2004 to 2017, including occurrence distributions of the northern
121 and southern SKR as a function of latitude. Close examination of these data reveals
122 the extinction of the main SKR emission at higher latitudes as well as some hemispheric
123 asymmetries. O’Dwyer et al. (2023) manually labelled hundreds of LFEs from
124 the Cassini dataset and note a specific class of events called “extinction LFEs” which are
125 observed from higher latitudes and where the upper frequency range of the main SKR band
126 (around 400 to 600 kHz) is significantly attenuated and sometimes completely disappears
127 when observed from the highest latitudes. Lamy et al. (2023) present a complete
128 statistical examination of the Cassini dataset with a view to further characterising the
129 SKR visibility as a function of the sub-observer co-ordinates (LT and latitude).

130 Thus clearly it is critical to take spacecraft location into consideration when interpreting
131 both the signal strength and the frequency span of radio emissions at Saturn as it’s
132 possible to see attenuation across the spectrum, extinction of a portion of the spectrum,
133 or reflection and refraction effects. For the short interval case studies presented in this
134 work, viewing conditions are relatively steady as the spacecraft doesn’t move much within
135 the observation window. For bigger statistical studies that may follow from this work,
136 where authors seek to quantitatively compare integrated powers and spectral morphologies
137 across the mission, care should be taken to account for visibility effects.

138 **3 Radio response to solar wind driving**

139 There are several key ways in which we can assess the response of Saturn’s radio emissions
140 to external driving by the variable solar wind. Here we focus first (section 3.1) on direct
141 solar wind comparison with radio emission (tracking radio emissions while Cassini was
142 outside the bow shock). We then follow up with an indirect examination (section 3.2),
143 inferring the upstream dynamic pressure at boundary crossings and tracking the radio
144 signatures around those encounters.

145 **3.1 Directly sampling solar wind**

146 In the absence of an upstream monitor at Saturn, and given the uncertainties in shock
147 arrival times from heliospheric propagation models, the most robust way to compare the
148 upstream solar wind driver and the resultant planetary radio emission is by direct mea-
149 surement of both simultaneously. Detailed studies of the IMF structure and solar wind
150 properties upstream of Saturn during the Cassini approach phase and SOI capture or-
151 bit have been made (Jackman et al., 2004, 2005a), and compression intervals shown to
152 elicit a response from the planet’s radio emissions (Jackman et al., 2005b). Moreover,

Table 1: Table of solar wind excursions with duration greater than 10 days following first Cassini capture orbit. Dates and times are given in the format YYYY-DOY-HR:MM (where DOY = Day of Year). Comments regarding each excursion are given in the right-hand column. The spacecraft is within 5° of the equatorial plane for all but the final solar wind excursion in 2016 when higher latitudes of 35° were reached.

Start SW excursion	End SW excursion	Duration (days)	LT range (hrs)	Comment
2004-314-12:43	2004-345-09:07	32.75	5.5 - 8.5	Case study in Figure 2
2005-027-16:13	2005-042-07:52	14.50	6.5 - 8.3	2 moderate compressions with closely-associated LFEs
2007-205-02:00	2007-232-08:30	27.25	13 - 16	1 moderate compression with broad IMF amplitude increase and closely-associated LFE
2007-245-12:30	2007-265-18:25	20.25	12.9 - 15.8	Rarefaction and significant data gap
2007-301-22:30	2007-314-01:40	12.25	12.6 - 14.8	1 very broad compression signature with LFE activity throughout
2011-137-17:45	2011-151-21:46	14.25	14.5 - 16.1	1 clear compression preceded by LFE
2016-140-17:45	2016-152-14:24	11.75	6.9 - 9.8	Rarefaction and patchy radio emission observed from higher latitudes (approx 35°)

153 Taubenschuss et al. (2006) took a quantitative approach to examining the time lag be-
 154 tween changes in upstream parameters and Saturn’s radio response, basing their study on
 155 Cassini’s approach to the planet prior to SOI as well as the first long capture orbit (2004
 156 DOY 202 to 326: July 20th – November 21st).

157 For this study we focus on later data, beyond the first capture orbit. During its 13-year
 158 Saturn orbital tour, Cassini crossed the bow shock outbound and sampled the solar wind
 159 on a total 623 occasions (Jackman et al., 2019; Jackman, 2022). The solar wind excursions
 160 vary in duration from several minutes to tens of days. Based on the duration of a solar
 161 rotation as seen from ~ 9 AU (25.5 days), and the typical phasing of compressions and
 162 rarefactions seen at Saturn orbit (two several-day long compressions each solar rotation,
 163 particularly during the declining phase of the solar cycle), we expect that 10 days or
 164 greater is a well justified time window of solar wind excursion to search for in the dataset
 165 to maximise the chances of capturing significant solar wind dynamics in the form of
 166 compressions. Table 1 shows the seven ≥ 10 – day long solar wind excursions which the
 167 Cassini spacecraft made during its primary orbital tour of Saturn. As can be seen, these
 168 excursions from one outbound bow shock crossing to the next inbound crossing, range in
 169 duration from 11.75 to 32.75 days. Unfortunately, due to spacecraft pointing issues and an
 170 instrument failure in 2012, we do not have regular plasma measurements in the solar wind

171 near Saturn so we cannot routinely measure parameters such as density, temperature,
 172 or solar wind dynamic pressure. For the solar wind excursions in this study we thus
 173 use magnetometer measurements as our primary indicator of the timing of solar wind
 174 compression. We manually inspected the IMF traces in all cases and noted compressions
 175 as the onset of intervals where the IMF magnitude exceeds 0.5 nT. We expect these
 176 compressions to be phased twice per solar rotation during the declining phase of the
 177 solar cycle (early years of Cassini Saturn exploration).

178 Figure 2 shows data from 2004 day 334-344 (November 29th - December 9th). This 10-
 179 day interval is part of a longer 32-day solar wind excursion. During the first 20 days
 180 of the excursion, the radio emission displayed regular SKR bursts modulated in concert
 181 with the Planetary Period Oscillations (PPOs) and the solar wind was relatively quiet
 182 (Bradley et al., 2020). The interval we discuss here reveals a significant departure from
 183 this steady state. During these 10 days, the spacecraft was inbound toward Saturn from
 184 its apoapsis position, traversing radial distances from ~ 72 to $\sim 48 R_S$ on the dawn flank
 185 of the magnetosphere.

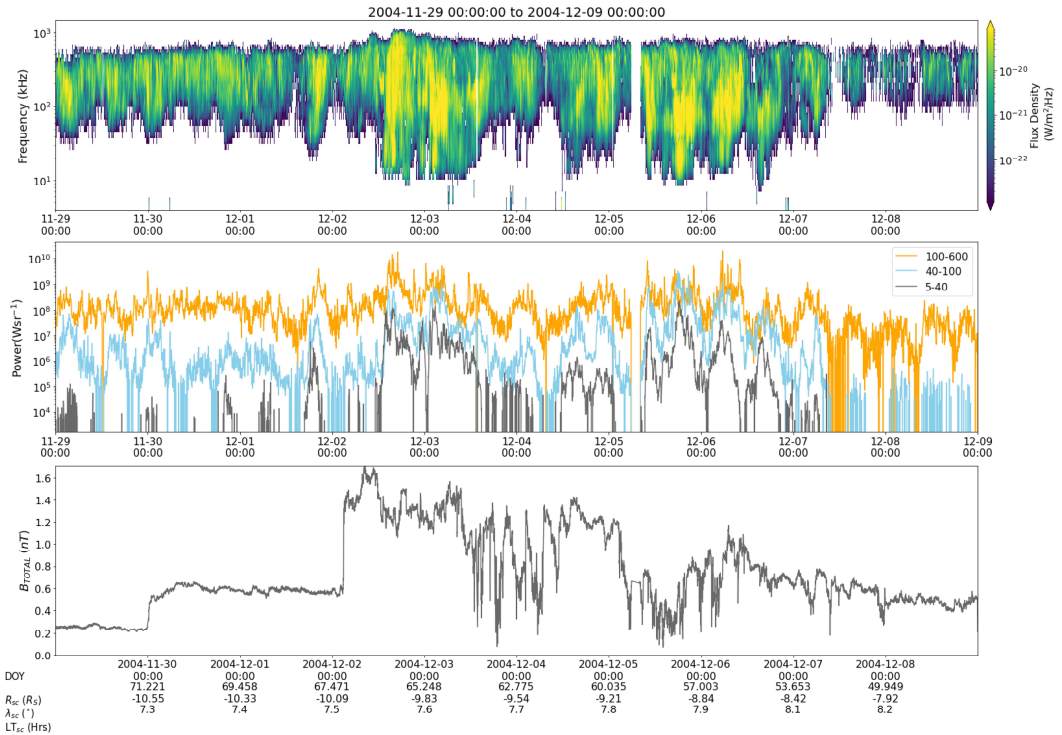


Figure 2: 10 days of Cassini radio and magnetometer data for an interval from 2004 day 334-344 (November 29th - December 9th). Top panel is a frequency-time spectrogram from Cassini RPWS, middle panel is the integrated radio power in 3 bands (100-600 kHz gold, 40-100 kHz blue, 5-40 kHz grey). The bottom panel shows the total IMF strength measured by Cassini in the solar wind

186 We observe a weak compression begin on November 30th with a small step change in

187 the IMF magnitude. Three days later, on December 2nd at 03:00, we observe a much
188 more significant sharp change in the amplitude of the field, representative of the arrival
189 of a strong shock compression at the spacecraft, with an almost instantaneous increase in
190 IMF magnitude of ~ 1 nT, consistent with the type of solar wind compressions reported
191 in (Jackman et al., 2004). Approximately 10 hours later the radio emissions start to
192 significantly brighten and then explosively expand into a huge LFE which continues for
193 almost 24 hours. We class this as a “monster LFE” such as those labelled by O’Dwyer et
194 al. (2023). Such radio signatures are relatively rare, and are distinct from
195 the more regular, short LFEs which tend to fall in phase with the PPOs (Badman et al.,
196 2008; Reed et al., 2018). We thus interpret this interval of severe radio disturbance
197 as being directly driven by the arrival of a solar wind compression which in turn set
198 in motion a chain of magnetospheric disturbance, culminating in the precipitation of
199 energetic particles into the auroral zone, and the stimulation of radio sources at higher
200 altitudes, producing the observed lower frequency radio emission.

201 It is very important to note that this is a favourable case study example. It had been
202 hoped that solar wind excursions during the main Cassini mission may have yielded more
203 opportunities to sample significant solar wind compressions in situ with field and plasma
204 instruments and explore their radio counterparts. However, as can be seen from the notes
205 in Table 1, many of the extended solar wind excursions did not lend themselves to such
206 comparison. There are several reasons for this. Firstly, some intervals were hampered by
207 data gaps. Secondly, several intervals displayed some moderate compressions but with
208 very broad signatures in IMF magnitude, thus not allowing us to ascertain a clear start
209 time for the effect of the compression. The sharp forward shocks such as shown in Figure
210 2 are somewhat exceptional. Thirdly, Cassini was a magnetospheric orbiter, with science
211 goals which required much of its orbit to take place quite close to Saturn and its moons
212 and rings. Thus the apoases of the spacecraft during the main mission were all typically
213 within $70 R_S$ of the planet with many within $40 R_S$, particularly later in the mission as
214 the spacecraft latitude increased. For the spacecraft to be sampling the solar wind at such
215 positions, one would require a significantly compressed bow shock such that the boundary
216 was pushed planetward of the spacecraft. Jackman et al. (2019) showed a distribution
217 of inferred dynamic pressure from bow shock crossings made by Cassini compared to a
218 distribution of dynamic pressure from a propagated model, and it revealed a clear shift
219 of the bow shock crossing distribution to higher (more compressed) dynamic pressures.
220 Thus it may be the case that when Cassini spent a significant amount of time in the
221 solar wind near apoapsis, the primary compression which led to that scenario happened
222 before the solar wind excursion, and thus the solar wind sampling revealed moderate or
223 seemingly steady state conditions. We can postulate that compressions preceded these
224 intervals, but with a single spacecraft the separation of temporal from spatial effects is
225 extremely challenging and relies on several assumptions.

226 3.2 Inferring solar wind conditions near boundaries

227 As mentioned above, Cassini traversed the magnetopause and bow shock a few thousand
228 times during the mission. At each of these crossings we can employ boundary models to
229 track from the crossing location back to the nose of the magnetosphere and in turn infer the

230 upstream dynamic pressure which would place a boundary at that location (under steady
 231 state conditions). Jackman et al. (2019) explored this, utilising the magnetopause model
 232 of Kanani et al. (2010) and the bow shock model of Went et al. (2011). When searching
 233 for evidence of solar wind compression on the magnetosphere through indirect means,
 234 we can explore the boundary crossing intervals and take information from these inferred
 235 dynamic pressures. In particular, we can examine cases where Cassini’s radial distance
 236 from the planet is increasing, and the spacecraft crosses the magnetopause outbound
 237 followed by the bow shock outbound next. If this inter-crossing interval (and associated
 238 magnetosheath residence time) is short, and/or the inferred dynamic pressure at these
 239 successive boundary crossings shows a large difference, it may reasonably be assumed that
 240 this corresponds to an interval where the magnetosphere was undergoing compression such
 241 that the bow shock was moved inward of its nominal position.

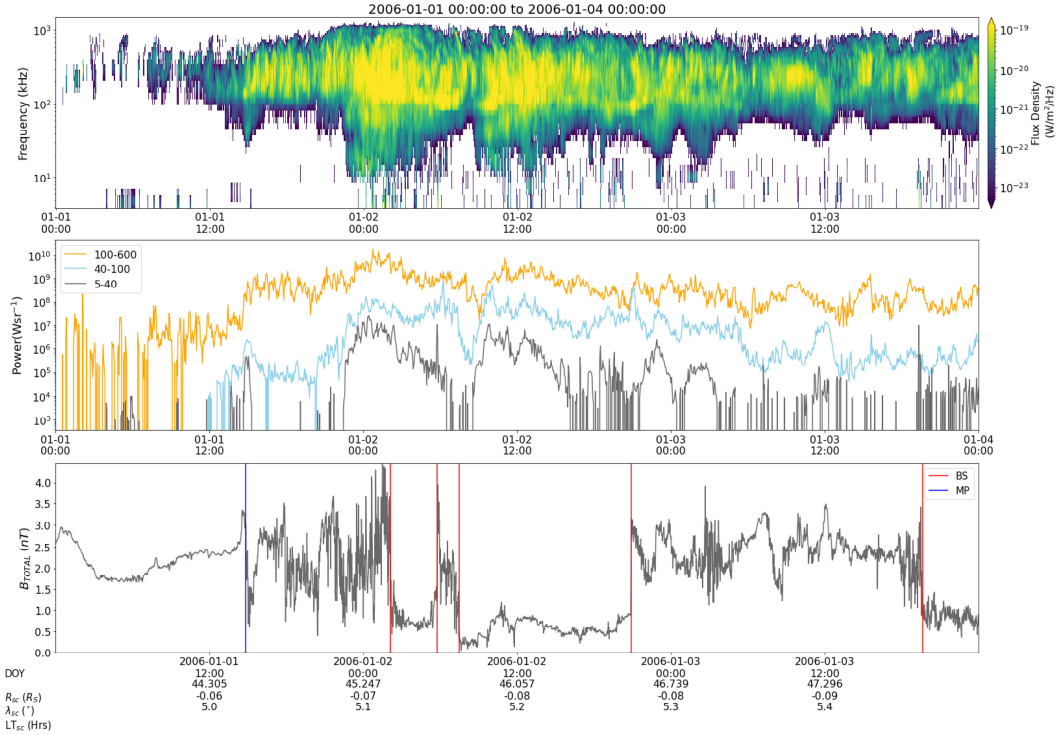


Figure 3: A 4 day interval from 2006 day 001-004 (January 1st-4th) in the same format as Figure 2 with a radio spectrogram, integrated radio powers, and total magnetic field strength. Vertical lines on the bottom panel show the times of magnetopause (blue) and bow shock (red) boundary crossings.

242 In Figure 3 we examine one such example and compare to the observed radio emissions.
 243 During the four-day interval shown, Cassini begins in the magnetosphere at a radial
 244 distance of $\sim 44 R_S$ pre-dawn. At 14:49 on day 001, Cassini crossed the magnetopause
 245 outbound. Less than 12 hours later, at 02:07 on day 002, Cassini crossed the bow shock
 246 outbound. This outbound crossing was preceded by an interval of significantly enhanced

247 magnetosheath magnetic field amplitude. The inferred upstream dynamic pressure at
 248 these crossings was 0.022 and 0.19 nPa respectively. The latter value represents signif-
 249 icantly compressed solar wind when compared to the typical distribution of solar wind
 250 dynamic pressure (D_P) values at the orbit of Saturn (Jackman & Arridge, 2011). The
 251 following bow shock crossings over the subsequent 30 hours show a slowly decreasing pro-
 252 file of D_P , with values of 0.178, 0.173, 0.138 and 0.101 nPa for the bow shock crossings
 253 marked by horizontal lines on Figure 3. This interval of solar wind compression is tied
 254 closely to an extended SKR burst and associated “monster” LFE which began to build
 255 from $\sim 15 : 00$ on day 001, with an order of magnitude increase in main SKR band power
 256 (middle panel), followed by an explosive ignition of the lower frequency components of
 257 the radio spectrum from $\sim 22 : 00$ on day 001. This intense LFE then persisted from
 258 several planetary rotations, only petering out from early on day 003.

259 4 Conclusions and Perspectives

260 In this article we have briefly summarised some of the key work linking Saturn’s radio
 261 emissions to extreme upstream driving and significant magnetospheric dynamics. We
 262 have outlined several ways that our list (Jackman, 2022) of magnetopause and bow shock
 263 crossings from the Cassini mission can be used to select out extended solar wind intervals
 264 (for direct sampling, Section 3.1 above), and pairs of boundary crossings with large gradi-
 265 ent in inferred solar wind dynamic pressure (indirect sampling, Section 3.2 above). There
 266 seems to be a moderately robust correlation between apparent solar wind compressions
 267 and the appearance of long (greater than 1 planetary rotation) LFEs. Several open ques-
 268 tions remain and below we list several, along with ideas for how they might be tackled in
 269 the near future:

- 270 • How is the lag time between a solar wind compression and radio response impacted
 271 by the observer location? Taubenschuss et al. (2006) examined the link between
 272 SKR and upstream parameters during the Cassini approach near dawn, when the
 273 steady local time viewing position was most favourable relative to the primary SKR
 274 beaming pattern. How can we use cases from the rest of the Cassini mission at other
 275 local times to test the response time to known compressions?
- 276 • Are long (multiple planetary rotation) LFEs a near-perfect proxy for compression?
 277 These “monster” LFEs (O’Dwyer et al., 2023) are seen from case studies
 278 (Bunce et al., 2005; Kurth et al., 2005; Palmerio et al., 2021) and small statistical
 279 studies (Jackman et al., 2009; Reed et al., 2018; Lamy et al., 2018) to almost uni-
 280 versally link to extreme compression-driven magnetospheric dynamics, and to have
 281 a different character to the PPO-modulated shorter SKR bursts which appear far
 282 more frequently in the dataset. The work of O’Dwyer et al. will ultimately lead
 283 to a complete list of LFEs from the mission and this will enable quantification of
 284 the distribution of LFE durations, allowing us to explore if there is a threshold
 285 above which “long” LFEs have properties distinct from their shorter counterparts.
- 286 • What impact does observer position have on confidence in correlating radio be-
 287 haviour and upstream driving? Several studies have revealed the average location

of Saturn’s radio sources in the near-dawn local time range (Lamy et al., 2009) and we know that this results in an observed pattern of emission which maximises in a several-hours-wide sector (Reed et al., 2018). It remains to be quantified whether this results in a total attenuation of LFEs in so-called unfavourable viewing regions (such as near dusk) or whether we may simply be able to apply a normalisation criterion to track dynamic radio emission in this zone. We risk losing a vast amount of information from noon-to-midnight local times if we cannot find a way to appropriately account for poorer visibility in these regions.

- Which upstream parameters are most closely linked with the appearance of long LFEs? Future work will include the use of mutual information theory to compare upstream measures such as solar wind dynamic pressure, velocity, density and IMF magnitude with time series of integrated radio power across the lower frequency bands. Similar techniques (Fogg et al., submitted 2023) have been employed at Earth to match the timescales for correlation of upstream metrics with geomagnetic indices, particularly during extreme substorm intervals.
- What is the spectral morphology of LFEs and what does this tell us about the vertical structure of the auroral acceleration region? Statistical analysis of SKR bursts and LFEs from the entire Cassini mission will soon be possible, based on the catalogue of O’Dwyer et. al., (2023) and the results of using this catalogue as training data from a machine learning algorithm to select such events across 13 years O’Dwyer et. al. in prep, 2023. These approaches will provide the full shape of SKR bursts and how they evolve into LFEs via the motion of radio sources to higher altitude and the associated emission at lower frequencies. We wish to explore the timeline where a burst becomes an LFE to understand what is special about this lower frequency portion of Saturn’s radio spectrum.

Acknowledgements: CMJ, EOD, CKL, ARF were funded by Science Foundation Ireland award 18/FRL/6199. ARF’s work was supported by IRC Government of Ireland Postdoctoral Fellowship GOIPD/2022/782. J. E. Waters’s work was supported by the EPSRC Centre for Doctoral Training in Next Generation Computational Modelling Grant No. EP/L015382/1. LL acknowledges the support from CNES and CNRS/INSU programs of planetology and heliophysics. CMJ acknowledges many enlightening discussions with Michelle Thomsen about the generation of the crossing list and its broader utility.

References

- Andrews D. J., Coates A. J., Cowley S. W. H., Dougherty M. K., Lamy L., Provan G., Zarka P., 2010, Magnetospheric period oscillations at Saturn: Comparison of equatorial and high-latitude magnetic field periods with north and south Saturn kilometric radiation periods, *Journal of Geophysical Research (Space Physics)*, 115, A12252
- Badman S. V., Cowley S. W. H., Lamy L., Cecconi B., Zarka P., 2008, Relationship between solar wind corotating interaction regions and the phasing and intensity of Saturn kilometric radiation bursts, *Annales Geophysicae*, 26, 3641

- 328 Bradley T. J., et al., 2020, Saturn's Nightside Dynamics During Cassini's F Ring and
329 Proximal Orbits: Response to Solar Wind and Planetary Period Oscillation Modula-
330 tions, *Journal of Geophysical Research (Space Physics)*, *125*, e27907
- 331 Bunce E. J., Cowley S. W. H., Wright D. M., Coates A. J., Dougherty M. K., Krupp
332 N., Kurth W. S., Rymer A. M., 2005, In situ observations of a solar wind compression-
333 induced hot plasma injection in Saturn's tail, *Geophysical Research Letters*, *32*, L20S04
- 334 Cecconi B., Zarka P., 2005, Model of a variable radio period for Saturn, *Journal of Geo-
335 physical Research (Space Physics)*, *110*, A12203
- 336 Cecconi B., Lamy L., Zarka P., Prangé R., Kurth W. S., Louarn P., 2009, Goniopolarimet-
337 ric study of the revolution 29 perikrone using the Cassini Radio and Plasma Wave Sci-
338 ence instrument high-frequency radio receiver, *Journal of Geophysical Research (Space
339 Physics)*, *114*, A03215
- 340 Cecconi B., Witasse O., Jackman C. M., Sánchez-Cano B., Mays M. L., 2022, Effect
341 of an Interplanetary Coronal Mass Ejection on Saturn's Radio Emission, *Frontiers in
342 Astronomy and Space Sciences*, *9*, 800279
- 343 Desch M. D., Rucker H. O., 1983, The relationship between saturn kilometric radiation
344 and the solar wind, *Journal of Geophysical Research: Space Physics*, *88*, 8999
- 345 Dougherty M. K., et al., 2004, The Cassini Magnetic Field Investigation, *Space Science
346 Reviews*, *114*, 331
- 347 Galopeau P. H. M., Zarka P., Le Quéau D., 1995, Source location of Saturn's kilometric ra-
348 diation: The Kelvin-Helmholtz instability hypothesis, *Journal of Geophysical Research:
349 Space Physics*, *100*, 26397
- 350 Gurnett D. A., et al., 2004, The Cassini Radio and Plasma Wave Investigation, *Space
351 Science Reviews*, *114*, 395
- 352 Jackman C., 2022, List of Saturn magnetopause and bow shock crossings by the Cassini
353 spacecraft, doi:10.5281/zenodo.5913537, <https://doi.org/10.5281/zenodo.5913537>
- 354 Jackman C. M., Arridge C. S., 2011, Solar Cycle Effects on the Dynamics of Jupiter's
355 and Saturn's Magnetospheres, *Solar Physics*, *274*, 481
- 356 Jackman C. M., Achilleos N., Bunce E. J., Cowley S. W. H., Dougherty M. K., Jones
357 G. H., Milan S. E., Smith E. J., 2004, Interplanetary magnetic field at ~ 9 AU during
358 the declining phase of the solar cycle and its implications for Saturn's magnetospheric
359 dynamics, *Journal of Geophysical Research (Space Physics)*, *109*, A11203
- 360 Jackman C. M., Achilleos N., Bunce E. J., Cowley S. W. H., Milan S. E., 2005a, Structure
361 of the interplanetary magnetic field during the interval spanning the first Cassini fly-
362 through of Saturn's magnetosphere and its implications for Saturn's magnetospheric
363 dynamics, *Advances in Space Research*, *36*, 2120

- 364 Jackman C. M., Achilleos N., Bunce E. J., Cecconi B., Clarke J. T., Cowley S. W. H.,
365 Kurth W. S., Zarka P., 2005b, Interplanetary conditions and magnetospheric dynamics
366 during the Cassini orbit insertion fly-through of Saturn's magnetosphere, *Journal of*
367 *Geophysical Research (Space Physics)*, 110, A10212
- 368 Jackman C. M., Lamy L., Freeman M. P., Zarka P., Cecconi B., Kurth W. S., Cowley
369 S. W. H., Dougherty M. K., 2009, On the character and distribution of lower-frequency
370 radio emissions at Saturn and their relationship to substorm-like events, *Journal of*
371 *Geophysical Research (Space Physics)*, 114, A08211
- 372 Jackman C. M., Thomsen M. F., Dougherty M. K., 2019, Survey of Saturn's Magne-
373 topause and Bow Shock Positions Over the Entire Cassini Mission: Boundary Statistical
374 Properties and Exploration of Associated Upstream Conditions, *Journal of Geophysical*
375 *Research (Space Physics)*, 124, 8865
- 376 Kaiser M. L., Desch M. D., 1984, Radio emissions from the planets earth, Jupiter, and
377 Saturn., *Reviews of Geophysics and Space Physics*, 22, 373
- 378 Kaiser M. L., Desch M. D., Warwick J. W., Pearce J. B., 1980, Voyager Detection of
379 Nonthermal Radio Emission from Saturn, *Science*, 209, 1238
- 380 Kanani S. J., et al., 2010, A new form of Saturn's magnetopause using a dynamic pressure
381 balance model, based on in situ, multi-instrument Cassini measurements, *Journal of*
382 *Geophysical Research (Space Physics)*, 115, A06207
- 383 Kimura T., et al., 2013, Long-term modulations of Saturn's auroral radio emissions by
384 the solar wind and seasonal variations controlled by the solar ultraviolet flux, *Journal*
385 *of Geophysical Research (Space Physics)*, 118, 7019
- 386 Kurth W. S., et al., 2005, An Earth-like correspondence between Saturn's auroral features
387 and radio emission, *Nature*, 433, 722
- 388 Lamy L., 2017, The Saturnian kilometric radiation before the Cassini Grand Finale, in
389 *Planetary Radio Emissions VIII*, eds Fischer, G. and Mann, G. and Panchenko, M.
390 and Zarka, P., pp 171–190 (arXiv:1709.07693), doi:10.1553/PRE8s171
- 391 Lamy L., Zarka P., Cecconi B., Prangé R., Kurth W. S., Gurnett D. A., 2008a, Sat-
392 urn kilometric radiation: Average and statistical properties, *Journal of Geophysical*
393 *Research (Space Physics)*, 113, A07201
- 394 Lamy L., Zarka P., Cecconi B., Hess S., Prangé R., 2008b, Modeling of Saturn kilometric
395 radiation arcs and equatorial shadow zone, *Journal of Geophysical Research (Space*
396 *Physics)*, 113, A10213
- 397 Lamy L., Cecconi B., Prangé R., Zarka P., Nichols J. D., Clarke J. T., 2009, An auroral
398 oval at the footprint of Saturn's kilometric radio sources, colocated with the UV aurorae,
399 *Journal of Geophysical Research (Space Physics)*, 114, A10212
- 400 Lamy L., et al., 2013, Multispectral simultaneous diagnosis of Saturn's aurorae throughout
401 a planetary rotation, *Journal of Geophysical Research (Space Physics)*, 118, 4817

- 402 Lamy L., et al., 2018, Saturn's Northern Aurorae at Solstice From HST Observations
403 Coordinated With Cassini's Grand Finale, *Geophysical Research Letters*, *45*, 9353
- 404 Lecacheux A., Genova F., 1983, Source Localization of Saturn Kilometric Radio Emission,
405 *Journal of Geophysical Research: Space Physics*, *88*, 8993
- 406 Morioka A., et al., 2007, Dual structure of auroral acceleration regions at substorm onsets
407 as derived from auroral kilometric radiation spectra, *Journal of Geophysical Research*
408 (*Space Physics*), *112*, A06245
- 409 Nakamura Y., et al., 2019, Seasonal variation of north-south asymmetry in the intensity
410 of Saturn Kilometric Radiation from 2004 to 2017, *Planetary and Space Science*, *178*,
411 104711
- 412 Palmerio E., et al., 2021, Magnetic Structure and Propagation of Two Interacting
413 CMEs From the Sun to Saturn, *Journal of Geophysical Research (Space Physics)*, *126*,
414 e2021JA029770
- 415 Reed J. J., Jackman C. M., Lamy L., Kurth W. S., Whiter D. K., 2018, Low-Frequency
416 Extensions of the Saturn Kilometric Radiation as a Proxy for Magnetospheric Dynam-
417 ics, *Journal of Geophysical Research (Space Physics)*, *123*, 443
- 418 Taubenschuss U., Rucker H. O., Kurth W. S., Cecconi B., Zarka P., Dougherty M. K.,
419 Steinberg J. T., 2006, Linear prediction studies for the solar wind and Saturn kilometric
420 radiation, *Annales Geophysicae*, *24*, 3139
- 421 Thomsen M. F., Jackman C. M., Lamy L., 2019, Solar Wind Dynamic Pressure Upstream
422 From Saturn: Estimation From Magnetosheath Properties and Comparison With SKR,
423 *Journal of Geophysical Research (Space Physics)*, *124*, 7799
- 424 Warwick J. W., et al., 1981, Planetary Radio Astronomy Observations from Voyager 1
425 near Saturn, *Science*, *212*, 239
- 426 Went D. R., Hospodarsky G. B., Masters A., Hansen K. C., Dougherty M. K., 2011,
427 A new semiempirical model of Saturn's bow shock based on propagated solar wind
428 parameters, *Journal of Geophysical Research (Space Physics)*, *116*, A07202
- 429 Young D. T., et al., 2004, Cassini Plasma Spectrometer Investigation, *Space Science*
430 *Reviews*, *114*, 1
- 431 Zarka P., Lamy L., Cecconi B., Prangé R., Rucker H. O., 2007, Modulation of Saturn's
432 radio clock by solar wind speed, *Nature*, *450*, 265

0.5 Chapter IV

This chapter consists of an article published in the Journal of Geophysics Research titled ‘Saturn Anomalous Myriametric radiation, a new type of Saturn radio emission revealed by Cassini’. I am a co-author of this article. I contributed to this article by facilitating the comparison of incidents of Saturn Anomalous Myriametric Radion to LFEs. I hand-labelled a selection of LFEs using the visual criteria that I developed, prior to using the machine learning approach detailed in chapter II.














Geophysical Research Letters[®]



RESEARCH LETTER

10.1029/2022GL099237

Saturn Anomalous Myriametric Radiation, a New Type of Saturn Radio Emission Revealed by Cassini

S. Y. Wu^{1,2} , S. Y. Ye¹ , G. Fischer³ , U. Taubenschuss⁴ , C. M. Jackman⁵ , E. O'Dwyer⁵ , W. S. Kurth⁶ , S. Yao⁷ , Z. H. Yao⁸ , J. D. Menietti⁶ , Y. Xu⁸ , M. Y. Long⁹ , and B. Cecconi² 

Key Points:

- A new radio component namely the Saturn Anomalous Myriametric Radiation (SAM) is reported
- The characteristics of SAM are given including its spatial distribution, typical frequency, bandwidth and time duration
- SAM shows a possible connection to the compression of the magnetosphere

Supporting Information:

Supporting Information may be found in the online version of this article.

Correspondence to:

S. Y. Ye,
yyeessy@gmail.com

Citation:

Wu, S. Y., Ye, S. Y., Fischer, G., Taubenschuss, U., Jackman, C. M., O'Dwyer, E., et al. (2022). Saturn Anomalous Myriametric radiation, a new type of Saturn radio emission revealed by Cassini. *Geophysical Research Letters*, 49, e2022GL099237. <https://doi.org/10.1029/2022GL099237>

Received 25 APR 2022
Accepted 1 AUG 2022

¹Department of Earth and Space Sciences, Southern University of Science and Technology, Shenzhen, People's Republic of China, ²LESIA, Observatoire de Paris, Université PSL, CNRS, Sorbonne Université, Université de Paris, Meudon, France, ³Space Research Institute, Austrian Academy of Sciences, Graz, Austria, ⁴Department of Space Physics, Institute of Atmospheric Physics of the Czech Academy of Sciences, Prague, Czechia, ⁵School of Cosmic Physics, DIAS Dunsink Observatory, Dublin Institute for Advanced Studies, Dublin, Ireland, ⁶Department of Physics and Astronomy, University of Iowa, Iowa City, IA, USA, ⁷School of Geophysics and Information Technology, China University of Geosciences (Beijing), Beijing, People's Republic of China, ⁸Key Laboratory of Earth and Planetary Physics, Institute of Geology and Geophysics, Chinese Academy of Sciences, Beijing, People's Republic of China, ⁹Department of Space Physics, School of Electronic Information, Wuhan University, Wuhan, People's Republic of China

Abstract A new radio component namely Saturn Anomalous Myriametric Radiation (SAM) is reported. A total of 193 SAM events have been identified by using all the Cassini Saturn orbital data. SAM emissions are L-O mode radio emission and occasionally accompanied by a first harmonic in R-X mode. SAM's intensities decrease with increasing distance from Saturn, suggesting a source near Saturn. SAM has a typical central frequency near 13 kHz, a bandwidth greater than 8 kHz and usually drifts in frequency over time. SAM's duration can extend to near 11 hr and even longer. These features distinguish SAM from the regular narrowband emissions observed in the nearby frequency range, hence the name anomalous. The high occurrence rate of SAM after low frequency extensions of Saturn Kilometric Radiation and the SAM cases observed during compressions of Saturn's magnetosphere suggest a special connection to solar wind dynamics and magnetospheric conditions at Saturn.

Plain Language Summary This paper reports a new type of radio emission at Saturn. We name this emission "Saturn Anomalous Myriametric Radiation" (SAM). Due to the different morphological behavior of SAM emissions in the spectrogram, compared to the regularly observed narrowband emissions, SAM emissions are identified as a new radio component. We search for SAM events by using all the available data acquired by the Cassini spacecraft. A total of 193 SAM events are found and we summarized its characteristics. The spatial distribution of SAM shows a high latitude preference in occurrence. The observed intensities of SAM increase as the spacecraft approaches Saturn, suggesting a source near Saturn. The typical central frequency of SAM is near 13 kHz and the duration of SAM can extend to near 11 hr and even longer. The majority of the 193 SAM emissions are observed after the enhancement of the dominant Saturn radio emission Saturn Kilometric Radiation (SKR), which is deemed to be closely connected to the solar wind dynamics at Saturn. Therefore, SAM emissions are also possibly related to the conditions that cause the enhancement of SKR. This newly identified SAM emission may be used to study the magnetospheric dynamics of Saturn in the future.

1. Introduction

Saturnian radio emissions, such as the Saturn Kilometric Radiation (SKR) (Kaiser et al., 1980; Lamy et al., 2008), 5 kHz Narrowband emissions (5 kHz NB or narrowband Saturn Myriametric radiation (n-SMR) (Gurnett et al., 1981; Louarn et al., 2007; Ye et al., 2010), and 20 kHz Narrowband emissions (Lamy et al., 2008; Ye et al., 2011), have been studied for several decades. Discovered by the Voyager 1 planetary radio experiment (Kaiser et al., 1980), SKR is right hand circularly/elliptically polarized with respect to the source magnetic field with a frequency range of 3 kHz to 1.2 MHz (Fischer et al., 2009; Lamy et al., 2008). SKR is generated through the cyclotron maser instability in the auroral region (Lamy et al., 2008, 2018; Wu & Lee, 1979; Zarka, 1998). NB emissions were discovered by Voyager 1 in the 1980s as well (Gurnett et al., 1981; Scarf & Gurnett, 1977). NB emissions are observed in stable frequency ranges near 5 and 20 kHz, with a much narrower bandwidth in

© 2022. The Authors.
This is an open access article under the terms of the [Creative Commons Attribution License](https://creativecommons.org/licenses/by/4.0/), which permits use, distribution and reproduction in any medium, provided the original work is properly cited.

contrast to the broad-banded SKR (Ye et al., 2011). They are thought to be generated through mode conversion processes (Gurnett et al., 1981; Ye et al., 2009, 2010). The L-O mode NB emissions (for both 5 and 20 kHz) can be converted from Z-mode NB emissions that have been shown to be generated by non-thermal plasma distributions characterized by a loss cone and temperature anisotropy (Menietti et al., 2010, 2011, 2016, 2018).

Radio emissions are closely connected to magnetospheric activities in the Saturnian magnetosphere (Louarn et al., 2007; Mitchell et al., 2015; Wing et al., 2020). The power of SKR is strongly correlated with solar wind characteristics (Desch, 1982; Desch & Rucker, 1983; Jackman et al., 2010; Taubenschuss et al., 2006). A typical phenomenon, namely the low frequency extension (LFE) of SKR, which is an expansion of the entire kilometric spectrum and in particular of the main band from high to low frequencies, is shown to be a good proxy for reconnection events and compression-induced hot plasma injections in Saturn's magnetosphere (Bunce et al., 2005; Jackman & Arridge, 2011; Jackman et al., 2009, 2010; Reed et al., 2018). The LFE of SKR can be explained by the variation of the SKR source region, which would extend to a higher altitude along the magnetic field lines as a direct consequence of the precipitation of energetic particles along field lines into the auroral zone (Bunce et al., 2005; Jackman et al., 2009), and this feature is also commonly seen at Earth (Morioka et al., 2007, 2014). The SKR enhancement can be related to so-called type-1 plasma injection events (Mitchell et al., 2015), which are related to current sheet collapse and magnetotail reconnection at radial distances beyond $\sim 12 R_s$ (R_s : Saturn radius = 60,268 km). Recently, the 5 kHz NB emissions have been found to be connected to type-2 injection events (Wing et al., 2020), which are related to the interchange instability in the inner magnetosphere at a smaller radial distance (Hill, 1976).

We identify for the first time a new radio component which is usually observed near 10 kHz. Emissions at 10 kHz were observed in previous works (Menietti et al., 2009; Wing et al., 2020), but were simply referred to as NB emissions observed near 10 kHz. We name this type of emission Saturn Anomalous Myriametric radiation (SAM) based on their differences with the 5 and 20 kHz NB emissions (that can sometimes extend up or down to 10 kHz), such as the average wavelength, duration of the SAM signals and the morphology in the electric field spectrogram. Examples of the newly defined SAM emissions are shown in Section 2 and their characteristics are shown in Section 3. The main characteristics of SAM are a larger frequency drift, a larger bandwidth, and a longer duration compared to ordinary NB emissions around 10 kHz. This justifies their identification, isolation and separate study in this work. We also discuss these events in their broader magnetospheric context, exploring their link to SKR bursts and LFEs (Section 4).

2. Examples of the SAM Emission

Four examples of SAM are shown in Figure 1. The electric field spectrograms (in panels (a), (c), (e), and (g)) are from the Cassini Radio and Plasma Wave Science (RPWS) instrument and the values plotted in the figure are the auto-correlations of the dipole X-antenna signals (Gurnett et al., 2004). The circular polarization data shown in Figures 1b, 1d, 1f, and 1h are the Stokes V parameter (defined in the plane perpendicular to the wave normal, Kraus, 1966; Lamy et al., 2011; Fischer et al., 2009), obtained using the algorithm of Cecconi and Zarka (2005) by presetting the source at the center of Saturn. The R-X mode emissions in the polarization data in Figure 1b show a circular polarization degree close to -1 (blue) in the northern hemisphere and 1 (red) in the southern hemisphere due to the variation of the angle between the wave vector and the background magnetic field (Lamy et al., 2011; Ye et al., 2009). The L-O mode has opposite senses of polarization with respect to the wave vector in the northern ($V = +1$) and southern ($V = -1$) hemispheres.

The morphologies of the SAM (white solid boxes) in the spectrogram are different from the 5 kHz NB (red dashed boxes), the 20 kHz NB (orange dashed boxes) and the SKR (white dashed boxes in the spectrogram and black dashed boxes in the polarization plot). The SAM signals show variable frequency drifts (both downward and upward) with the lowest frequency extending down to 5 kHz (white box in panel (d)) and the highest frequency extending up to 20 kHz or even higher (panel (a)). The frequencies of SAM center around 13 kHz (detailed in Figure 2j). Compared to the 5 and 20 kHz NB, which usually show a stable frequency within a narrow band (Gurnett et al., 1981; Wang et al., 2010), SAM emissions sometimes cover broader frequency ranges (in panels (a) and (g) and also Figure 2j, often with more significant drifts (see details in Section 3). The frequency drifts in Figures 1a and 1c are roughly within the range 5 kHz/day to 12 kHz/day (see details in Section 3). In general, the duration of SAM is longer than typical 5 and 20 kHz NB emissions as shown in panels (a) and (g).

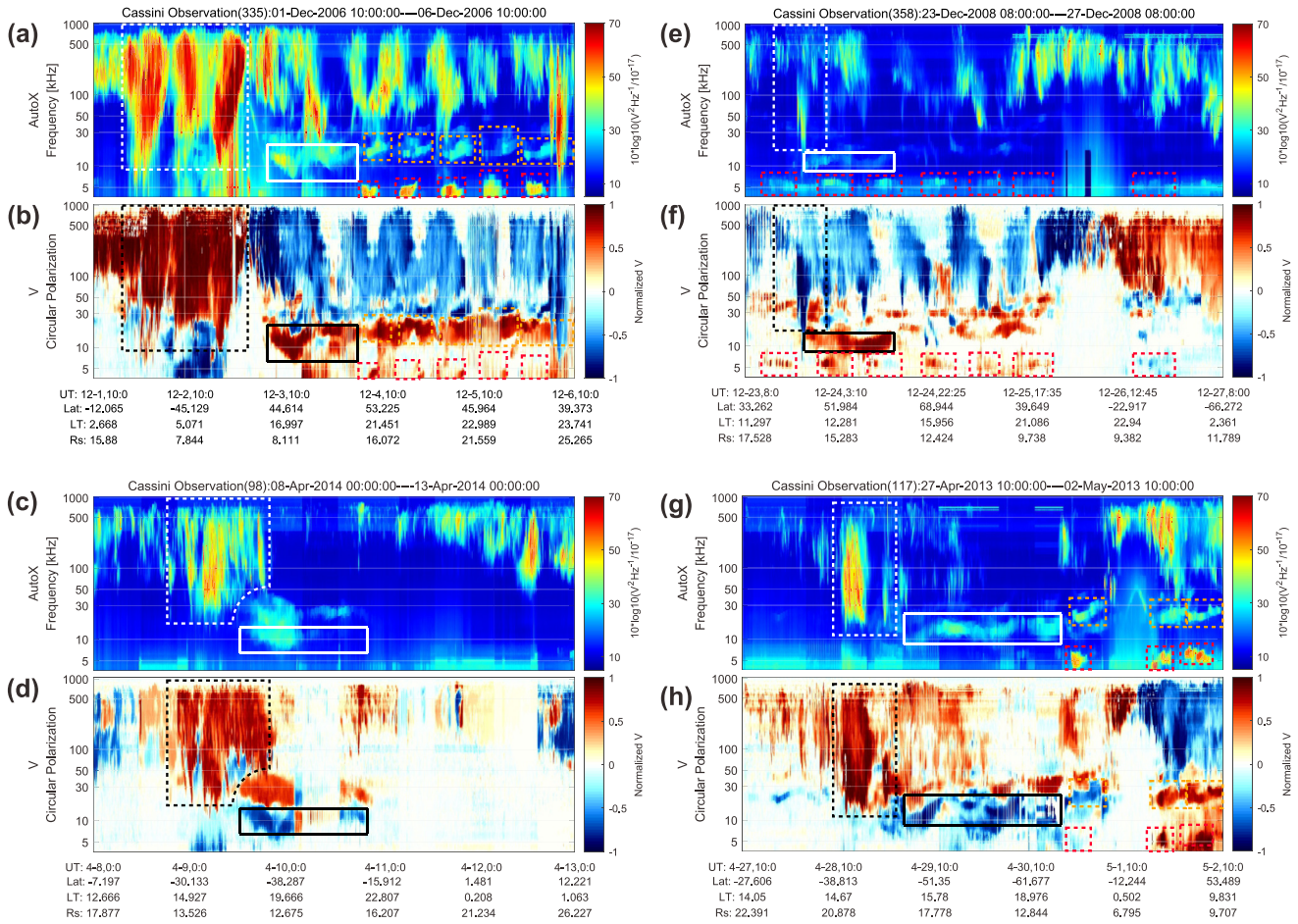


Figure 1. Four examples of the Saturn Anomalous Myriametric Radiation (SAM) signals. Panels (a–h) show four SAM cases with Panels (a, c, e, and g) showing the electric field spectrograms (measured by the Cassini Radio and Plasma Wave Science High Frequency Receiver (HFR)) and panels (b, d, f, and h) giving the circular polarization degree (obtained from the inversion method of Cecconi and Zarka (2005)). The SAM emissions are marked by the white and black solid boxes in the intensity and polarization panels (only the fundamental emissions are boxed), separately. The white and black dashed boxes indicate the Saturn Kilometric Radiation low frequency extension preceding the SAM. The red and orange dashed boxes indicate the 5 and 20 kHz NB, respectively. Cassini ephemeris data given at the bottom of each case are in the Saturn planetocentric coordinates.

SAM occasionally appear with a weaker first harmonic as can be recognized more easily in the circular polarization data in panels (d) and (h). The circular polarization degree shown in panels (d) and (h) suggests that the fundamental SAM is L-O mode and the harmonic is R-X mode. As indicated by the white dashed boxes in Panels (a), (c), (e) and (g), SAM usually appears after an LFE of SKR. Therefore, we will investigate a possible connection between the SKR LFE and the SAM in Section 4.

3. Method to Identify SAM and the Characteristics of SAM

Based on the Cassini RPWS instrument data (Gurnett et al., 2004), we manually identified 193 SAM cases by using the data from 2004 DOY (day-of-year) 001 to 2017 DOY 258. First, the start time, end time, lower and upper frequency limits of the fundamental emission of each event are marked in the electric field spectrogram by hand as indicated by the white solid boxes in Figures 1a, 1c, 1e, and 1g. The accurate information of each SAM event is then obtained by setting a threshold on the circular polarization to $|V| > 0.2$ within each white box. The power flux of each SAM event is then calculated by using the spectral density in the corresponding frequency range, the detailed calculation procedure is the same as given in Zarka et al. (2004) and Ye et al. (2010). The final list of all identified events is given in the Supporting Information S1.

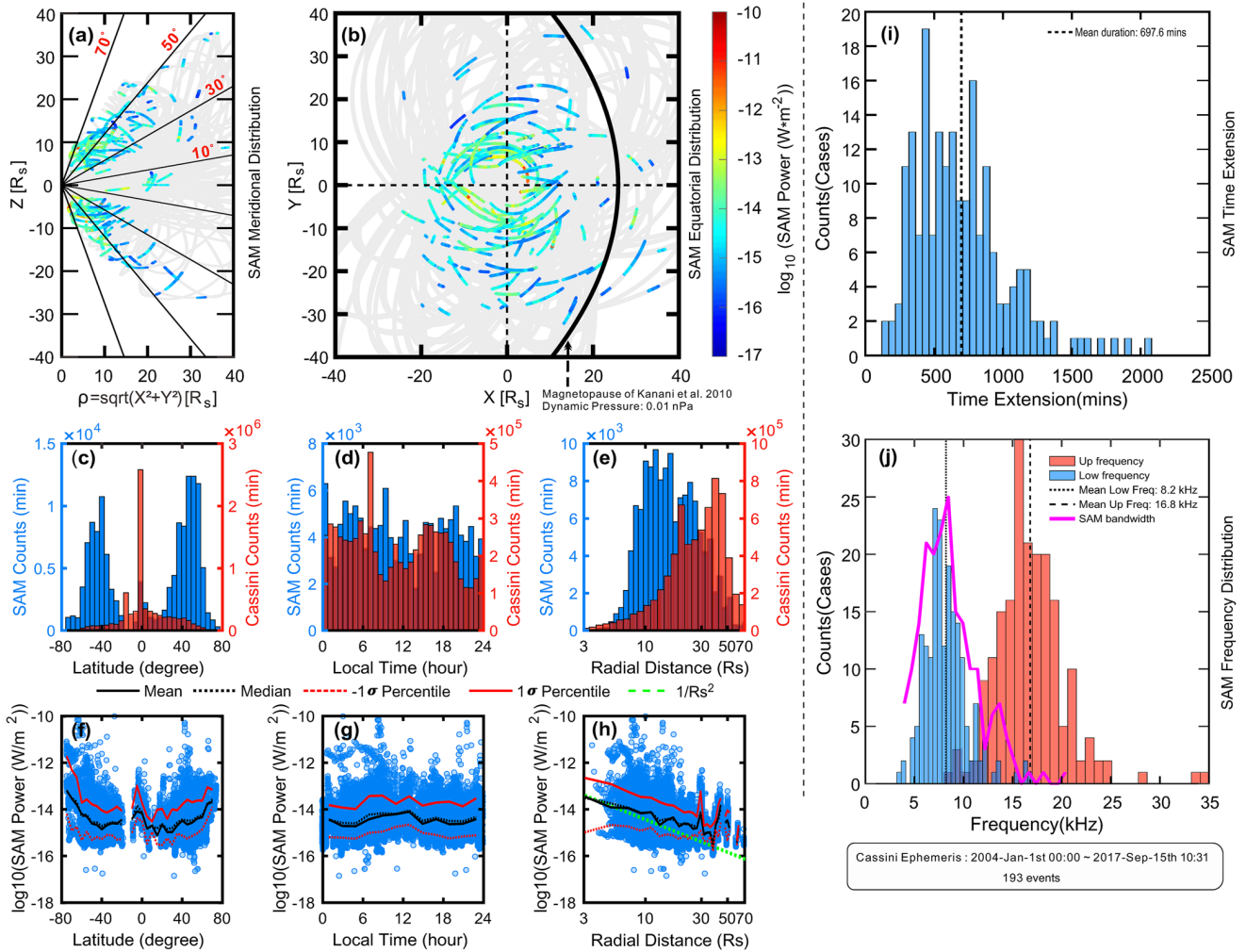


Figure 2. Characteristics of Saturn Anomalous Myriametric Radiation (SAM). Panels (a) and (b) give the spatial distribution of SAM in the meridional and equatorial plane with the power flux of SAM coded using the color bar on the right. The trajectory of Cassini during its Saturn orbital tour when SAM is not observed is marked in gray. The blue bins in Panels (c)–(e) show the histogram of SAM distribution in latitude, local time and radial distance. The overplotted red bins are the respective Cassini dwell times. Panels (f)–(h) give the power flux distribution of SAM in latitudes, local time and radial distance. The black and red lines (both solid and dotted) in panels (f)–(h) show the calculated power values (black: mean and median, red: percentile of ± 1 standard deviation) to indicate the variation trends of the data. The green line in Panel (h) marks a $1/r^2$ decreasing trend of the SAM power with the radial distance. Panels (i) and (j) give the time duration and frequency distribution of the SAM emissions. The pink line in panel (j) gives the bandwidth of SAM emissions.

The criteria which enabled us to distinguish the SAM from the neighboring SKR and from NB emissions in the overlapping frequency range of 3–35 kHz are as follows:

1. The SAM emissions' frequency varies between 3 and 35 kHz (typically 3–8 kHz for 5 kHz NB and 12–30 kHz for 20 kHz NB. Wu et al., 2021), and the center frequency of the fundamental emissions is near 10–15 kHz (typically around 5 and 20 kHz for the NB emissions Ye et al., 2009).
2. The SAM emissions' frequency shows larger frequency drifts (roughly several kilohertz/day, a simple eye-estimation of the frequency drifts on the cases in Figures 1a and 1c are approximately from 5 to 12 kHz/day) than the NB (typically upward frequency drift with 200 ~ 400 Hz/day for 5 and 20 kHz NB. Wang et al., 2010), and the upward drift and downward drift can be observed both in a single event.
3. The bandwidth of the fundamental SAM emissions is broader than the NB (2 ~ 3 kHz for 5 kHz NB and within 10 for 20 kHz NB. Wang et al., 2010).

We note here that each single SAM case in the list should meet at least the first two requirements above to be identified (for some cases the emissions are not that broadband but do satisfy the first two criteria). Finally, 193

cases of the SAM were identified, and the SAM events are very rare when compared to more than 2,000 cases for 5 kHz NB and more than 1,000 cases of the 20 kHz NB during the 13 years of data (Wu et al., 2021). Because of the rarity of this emission and the similarity between SAM and NB emissions, we note here that identifying the SAM in the spectrogram could be pretty subjective in some cases. However, the criteria mentioned above and the different spectral morphology of SAM and NB as displayed in Figure 1 warrant correct identification in the vast majority of the cases. The rarity of SAM observations in the complete Cassini RPWS data set may be due to the following reasons:

1. The SAM intensities are often weak. The power spectral density of a considerable part of the SAM cases is close to $10^{-15} \sim 10^{-16} \text{ V}^2 \text{ Hz}^{-1}$, which is close to the background noise level (Gurnett et al., 2004). Many cases in our event list were identified by looking at the polarization data since the signal in the power spectrogram is too weak.
2. SAMs are preferably observed at higher latitudes as shown in Figures 2a and 2c. No SAM emission was observed in 2015 due to the low inclination of Cassini's orbit during that year. Only 8 SAM cases are observed in the equatorial plane as shown in panel (a), which could be due to the reflection at the magnetosheath when the electron density in the magnetosheath is high enough, similar to the 5 kHz NB (Wu et al., 2022). This suggests that SAM emissions rarely undergo reflections at the magnetosheath as their frequency is mostly above the plasma frequency in the sheath (Wu et al., 2022).
3. These SAM emissions are sporadic events that may be attributed to some special magnetospheric conditions which are not fully understood at this time (as discussed in detailed in Section 4).

We note here that all the characteristics described below are for the fundamental emissions of SAM. The distributions of the 193 SAM events in the meridional and equatorial planes are given in Figures 2a and 2b. The SAM emissions are mainly observed at high latitudes with latitudes above 20° , similar to the 20 kHz NB (Wang et al., 2010; Wu et al., 2021).

The detailed occurrence and power flux distributions are given in panels (c)–(e) and (f)–(h) of Figure 2. The blue and red bins in panels (c)–(e) are the SAM counts and all Cassini orbital positions, respectively. The majority of the SAM emissions is observed between 20° and 70° southern and northern latitudes. Local time dependence is not observed. Most SAMs are observed inside the magnetopause as marked by the black solid line in Panel (b) (Kanani et al., 2010).

After integration over the SAM spectral frequency range for each of the 193 events, a total of 134,608 power flux values is obtained. These are plotted as blue circles with respect to latitude, local time and radial distance in Figures 2f–2h. The power of SAM decreases from high latitudes to low latitudes as indicated by the overplotted profiles in panel (f) (black solid and dotted for mean and median, respectively, red for percentile of 1 standard deviation, these profiles are derived from the logarithm scale (=mean of exponents)). The integration carried out within a box is sometimes polluted by a low frequency extension of SKR, especially near the equatorial plane, where it is difficult to separate SAM from SKR according to polarization (SKR emitted from the opposite hemisphere has the same sign of Stokes-V as the SAM emissions). Therefore, the small peak of the calculated average intensity near 0° in latitude in panel (f) may be an overestimate. No significant variation with local time is visible in panel (g). The power of SAM ranging from 10^{-16} W/m^2 to 10^{-10} W/m^2 shows a $1/r^2$ dependence on the radial distance (indicated by the green dashed line and also the calculated mean/median lines in panel (h)), which is consistent with a point source close to Saturn as the signal gradually weakens as it propagates away from Saturn. We also checked the longitudinal distribution of the SAM emissions, which shows quite uniform distribution (not shown). SAM events usually last for several hours, that is, they cover a broad longitude range due to Saturn's rapid rotation. It is thus not surprising that SAM visibility smears over all longitudes almost uniformly.

The distribution of time durations of SAM in Panel (i) peaks around 500 min with a mean duration of 697.6 min. Given Saturn's rotation period of roughly 10.6 hr (636 min), the average SAM duration is just a bit longer than one Saturn rotation, and in some cases, SAM can last for 2–3 Saturn rotations (e.g., case in Figure 1c and Figure S159 in the Supporting Information S1). The frequency distribution shown in Figure 2j suggests that SAMs' frequency ranges from 3 to 30 kHz and centers near 13 kHz. The pink line in Panel (j) gives the approximate bandwidths of the SAM emissions. Most of the SAM emissions have bandwidths larger than 5 kHz.

4. Relations Between SAM, LFE, Reconnection, and the Compression of the Magnetosphere

When identifying SAM events from the data, we notice that the SAM emissions are often observed after an SKR LFE (defined in the next paragraph). The SKR LFE is deemed as a good proxy for strong magnetospheric dynamics, which can include tail reconnection (e.g., Bunce et al., 2005; Jackman et al., 2009) that may be induced by solar wind compression (Reed et al., 2018).

To further explore this feature, we adopted an interactive polygon labeling method (Louis et al., 2022) to label the SKR LFE. The specific criteria of labeling SKR LFE are similar to the criteria of Reed et al. (2018) and are listed below:

1. The LFE begins when the main SKR band extends below 100 kHz and ends when it has returned to above 100 kHz.
2. The SKR has a minimum frequency of 40 kHz or less for it to be an LFE.
3. The SKR LFE also is a continuous extension, that is, there should be no frequency gap.

We identified 381 LFEs during the time interval between 24 hr before the SAM start time and the SAM end time. Finally, by confining the time to within 10.6 hr (one Saturn rotation) around the SAM start time ($|\text{SAM start time} \pm \text{LFE start or end time}| < 10.6 \text{ hr}$), 136 of 193 SAM events (ratio: $136/193 \sim 0.7$) are labeled as an event that is accompanied by LFE. Indeed, a total of 128 SAM events are observed to be preceded by the LFE emissions among these 136 cases. We perform a significance Z-test on the proportion of the SAM events accompanied by LFE (136/193) to test the relation between SAM and LFE. The SAM events are divided into two categories: SAMs that occurred with LFE, and SAMs that occurred without LFE. We could simply adopt a null hypothesis that the two categories are random processes with occurrence of the two groups $q_1 = q_2 = 50\%$. The Z value could be calculated through (Fleiss, 2003; Li & Yao, 2020): $Z = (p_1 - p_2) - (q_1 - q_2) / \sqrt{\frac{q_1(1-q_1)}{n_1} + \frac{q_2(1-q_2)}{n_2}}$ (where the $p_1 = 0.704$ and $p_2 = 0.295$ are the proportions of category 1 and category 2. q_1 and q_2 are the probabilities that are assumed to be equal ($q_1 = q_2 = 50\%$). $n_1 = 136$ and $n_2 = 57$ are the sample numbers of the two categories). The calculated Z value is 5.188, exceeding the critical Z test value (1.645) at a 95% confidence level, which implies a rather high proportion of SAM events associated with an LFE.

The statistical study of LFEs (Reed et al., 2018) based on data from 2006 suggests that short LFEs are a good proxy for tail reconnection and longer LFEs can be associated with the solar wind dynamics. We check the durations of the SAM-related LFEs as shown in Figure 3a. Note here for one SAM event, there could be several LFEs within the time range: $\text{SAM start time} \pm 10.6 \text{ hr}$. These events are all plotted in Figure 3a and 3b. The 10.6 hr (i.e., 1 Saturn rotation) threshold is used to separate the short and long LFEs, which is reasonable as suggested by the former studies (Bunce et al., 2005; Reed et al., 2018 and the references therein). Roughly 92% of LFEs (260/282, as shown in Figure 3a) have a duration shorter than 10.6 hr, suggesting these LFEs are possibly related to the tail reconnection (indicated by blue bins in Figure 3a). We stress, however, that tail reconnection may be driven internally (by the Vasyliunas cycle (Vasyliunas, 1983)) or externally (by the Dungey cycle (Dungey, 1961)). Seeing more short LFEs does not necessarily favor internal drivers over external ones (e.g., solar wind compression). Moreover, assessment of the duration of the LFEs is also influenced by the spacecraft location, because the observer local time relative to the beaming from the hollow cone of emission has a significant impact on the received radio power. It is possible that “short” LFEs are merely truncated due to the spacecraft moving into/out of the primary radio viewing region before the entire episode can be sampled. Thus it is likely that the duration of the shorter LFEs could be taken as a slight underestimate in some cases. There are 22 SAM events that are accompanied by these 22 long LFEs and 114 SAM events are accompanied by the rest 262 short LFEs. Indeed, the fact that 282 LFEs are observed near the 136 SAM events suggests that the SAM emissions are generated under active magnetospheric conditions.

The time delays between the labeled 136 SAM events and the labeled SAM-related LFEs (in total 282 events) are shown in Figure 3b. The approximate time delay is derived by subtracting the start time of SAM emission from the start time of SKR LFEs. The mean delay time between short LFE and SAM is about 4.3 hr (with median value 4.89 hr) as marked by the blue line in Figure 3b. The waiting time between the long LFEs and the SAM emission is approximately 16.4 hr (estimated from 22 cases, as marked by the red line in Figure 3b). For these 22 long LFEs, it is their stop-time which gets closer than 10.6 hr to the SAM start-time. Therefore, the long LFE

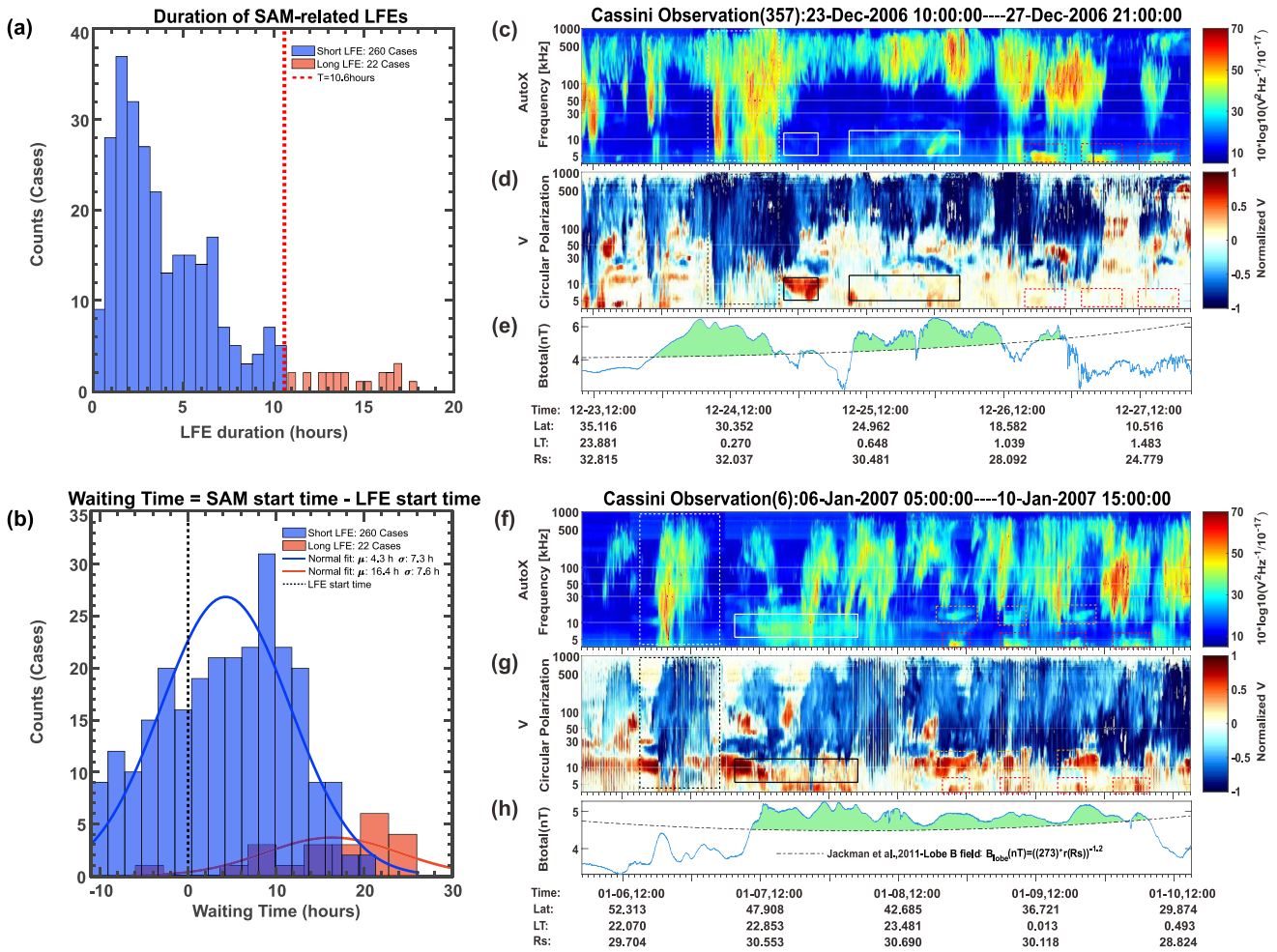


Figure 3. Saturn Anomalous Myriametric Radiation-low frequency extension (SAM-LFE) relation. Panel (a), the time duration of the SAM-related LFEs, separated to long/short LFEs using a threshold 10.6 hr. Panel (b), the waiting time histogram between the start time of SAM emissions and the start time of SAM-related LFEs. Panels (c and d) and (f and g) are in the same format as Figure 1. Panels (e and h) are the total magnetic field measured by the Cassini magnetometer instrument (Dougherty et al., 2004). The black dashed line marks the fitted averaged lobe field derived by Jackman et al. (2011). The green shaded area marks the region with magnetic field surpassing the averaged lobe field.

start-time can be much further away from the SAM start-time, explaining the very long delay times. Furthermore, it is possible that SAM would be there much closer to the start-time of a long LFE, but it is just not visible in the spectrum because the long LFE is superposing the weaker SAM emission entirely. These results suggest that the occurrence of SAM emissions is associated with the magnetospheric conditions that lead to SKR LFE. Note here that the derived waiting time is only approximate due to the uncertainty of the start time of the LFEs, which strongly relies on the spacecraft viewing geometry.

Even though the majority of the SAM emissions are observed after SKR LFE, according to previous studies (Jackman et al., 2009; Reed et al., 2018), most of the LFEs appeared without being followed by SAM. This can be attributed to several reasons, like tighter visibility constraints for SAM in comparison to SKR (especially with latitude and intensity), or additional requirements for the excitation of SAM on top of those for SKR LFEs. We show possible evidence of the connection between SAM and the solar wind compressions in Figures 3c, 3e, 3f, and 3h. The magnetic field data in Panels (e) and (h) are from the Cassini-MAG instrument (Dougherty et al., 2004). Cassini was in the northern tail lobe region during the two time intervals. Clear magnetotail compressions are observed (indicated by the green shaded region in Panels (e) and (h)) with an increase in the total magnetic field strength above what is typically observed in the lobe at that radial distance (Jackman & Arridge, 2011). The compression lasts for almost 3 days for the second case in Panel (h), until 2007 DOY 010

10:00 UT when the lobe magnetic field gradually decreased. The SAM emission in Panel (f) is almost synchronized with the start of the compression, which could imply that the excitation of the SAM emission is due to the compression of the magnetosphere.

Here we highlight the close relationship between SAM emissions and SKR LFEs that the LFE is always seen when there is a SAM. The examples in Figure 3 suggest that the SAM emission could be triggered by magnetospheric compression in favor of tail reconnection, which would also implied that the LFE seen simultaneously were also triggered by the magnetospheric compression.

5. Discussion and Summary

As reported in earlier studies (Bradley et al., 2020; Bunce et al., 2005; Cowley et al., 2005; Guo et al., 2018; Jackman et al., 2009; Mitchell et al., 2015; Reed et al., 2018; Thomsen et al., 2019), compressions of the Saturnian magnetosphere caused by interplanetary corotating interaction regions or Coronal Mass Ejections can trigger a series of magnetospheric responses including motion of the magnetospheric boundaries, dayside and nightside magnetic reconnection, magnetotail current sheet collapse, plasmoid release, hot plasma injection and the intensification of SKR. In the absence of an upstream probe at Saturn, studies have used magnetospheric boundary locations or propagated solar wind models (e.g., Tao et al., 2005; Zieger and Hansen., 2008) to infer the state of the upstream medium. There is also significant reason to use the radio emissions as a remote proxy for upstream conditions if the radio emissions can be cataloged and understood appropriately.

The SKR signals are usually used as an important tool to indicate large-scale disturbances such as auroral intensification, tail reconnection, and intensified field-aligned current (Bradley et al., 2020; Palmaerts et al., 2018). The SAM emissions could also be used as a remote indicator of the compression or the magnetic reconnections once the detailed relations between these phenomena are clarified in further studies. At present, the generation mechanism of SAM is uncertain due to the lack of observations. The SAM emissions show very similar features to the 20 kHz NB with respect to frequency range, polarization characteristics and the frequent occurrence of harmonic emissions. One may suspect that the SAM emissions are just a kind of anomalous 20 kHz NB but generated under special magnetospheric conditions. However, in some cases, both the SAM emissions and the 20 kHz NB can exist simultaneously, as shown in some cases in the Supporting Information S1 (e.g., Figures S24, S28, S37, S38, and S43 in Supporting Information S1). More detailed studies, for example, a direction-finding case study may answer this.

In this study, we proposed a new radio component called Saturn Anomalous Myriametric radiation and investigated the basic characteristics of SAM and the possible connection between SAM and the other magnetospheric processes. Our main findings are as follows:

1. The SAM emissions show variable frequency drifts and obvious differences in spectral morphology to narrow-band emissions, which are usually observed in the adjacent frequency range. Therefore, these emissions are distinguished in this study and named SAM.
2. The SAM emissions are L-O mode emissions usually occurring at around 13 kHz, and at high latitudes and sometimes accompanied by the R-X mode first harmonic.
3. The SAM emissions are often observed following an LFE of SKR and are possibly associated with the solar wind compression of the magnetosphere.

Data Availability Statement

The Cassini Radio and Plasma Wave Science data used in this work were downloaded from the LESIA/Kronos collection with n2 level data (Cecconi et al., 2017a) and n3d data (Cecconi et al., 2017b, goniopolarimetric data obtained using the method Cecconi & Zarka. 2005). The Cassini MAG data were downloaded from the Planetary Data System at (MAG: <https://doi.org/10.17189/1519602>). The SAM catalog is also available from the MASER service via a doi: <https://doi.org/10.25935/8may-4320>.

Acknowledgments

This work was supported by the Strategic Priority Research Program of the Chinese Academy of Sciences (grant No. XDB 41000000). GF and UT acknowledge support from their FWF-GACR international project (I 4559-N/20-06802L), financed by the Austrian Science Fund FWF and the Czech Science Foundation GACR. CMJ's and EOD's work is supported by the Science Foundation Ireland Grant 18/FRL/6199. SYW is also supported by China Scholarship Council.

References

- Bradley, T. J., Cowley, S. W. H., Bunce, E. J., Melin, H., Provan, G., Nichols, J. D., et al. (2020). Saturn's nightside dynamics during Cassini's F ring and proximal orbits: Response to solar wind and planetary period oscillation modulations. *Journal of Geophysical Research: Space Physics*, *125*(9), e2020JA027907. <https://doi.org/10.1029/2020JA027907>
- Bunce, E. J., Cowley, S. W. H., Wright, D. M., Coates, A. J., Dougherty, M. K., Krupp, N., et al. (2005). In situ observations of a solar wind compression-induced hot plasma injection in Saturn's tail. *Geophysical Research Letters*, *32*(20), L20S04. <https://doi.org/10.1029/2005GL022888>
- Cecconi, B., Lamy, L., & Zarka, P. (2017a). Cassini/RPWS/HFR LESIA/Kronos N2 data collection (Version 1.0). *PADC*. <https://doi.org/10.25935/xs9j-nd90>
- Cecconi, B., Lamy, L., & Zarka, P. (2017b). Cassini/RPWS/HFRLESIA/KronosN3ddatacollection(Version 1.0). *PADC*. <https://doi.org/10.25935/5jfx-dh49>
- Cecconi, B., & Zarka, P. (2005). Direction finding and antenna calibration through analytical inversion of radio measurements performed using a system of two or three electric dipole antennas on a three-axis stabilized spacecraft. *Radio Science*, *40*(3), 1–20. <https://doi.org/10.1029/2004RS003070>
- Cowley, S. W. H., Badman, S. V., Bunce, E. J., Clarke, J. T., Gérard, J.-C., Grodent, D., et al. (2005). Reconnection in a rotation-dominated magnetosphere and its relation to Saturn's auroral dynamics. *Journal of Geophysical Research*, *110*(A2), A02201. <https://doi.org/10.1029/2004JA010796>
- Desch, M. D. (1982). Evidence for solar wind control of Saturn radio emission. *Journal of Geophysical Research*, *87*(A6), 4549–4554. <https://doi.org/10.1029/JA087iA06p04549>
- Desch, M. D., & Rucker, H. O. (1983). The relationship between Saturn kilometric radiation and the solar wind. *Journal of Geophysical Research*, *88*(A11), 8999–9006. <https://doi.org/10.1029/JA088iA11p08999>
- Dougherty, M. K., Kellock, S., Southwood, D. J., Balogh, A., Smith, E. J., Tsurutani, B. T., et al. (2004). The Cassini magnetic field investigation. *Space Science Reviews*, *114*(1), 331–383. <https://doi.org/10.1007/s11214-004-1432-2>
- Dungey, J. W. (1961). Interplanetary magnetic field and the auroral zones. *Physical Review Letters*, *6*(2), 47–48. <https://doi.org/10.1103/PhysRevLett.6.47>
- Fischer, G., Cecconi, B., Lamy, L., Ye, S.-Y., Taubenschuss, U., Macher, W., et al. (2009). Elliptical polarization of Saturn Kilometric Radiation observed from high latitudes. *Journal of Geophysical Research*, *114*(A8), A08216. <https://doi.org/10.1029/2009JA014176>
- Fleiss, J. L., Levin, B., & Paik, M. C. (2003). The comparison of proportions from several independent samples. In *Statistical methods for rates and proportions* (pp. 187–233). John Wiley & Sons, Ltd. <https://doi.org/10.1002/0471445428.ch9>
- Guo, R. L., Yao, Z. H., Wei, Y., Ray, L. C., Rae, I. J., Arridge, C. S., et al. (2018). Rotationally driven magnetic reconnection in Saturn's dayside. *Nature Astronomy*, *2*(8), 640–645. <https://doi.org/10.1038/s41550-018-0461-9>
- Gurnett, D. A., Kurth, W. S., Kirchner, D. L., Hospodarsky, G. B., Averkamp, T. F., Zarka, P., et al. (2004). The Cassini radio and plasma wave investigation. *Space Science Reviews*, *114*(1), 395–463. <https://doi.org/10.1007/s11214-004-1434-0>
- Gurnett, D. A., Kurth, W. S., & Scarf, F. L. (1981). Narrowband electromagnetic emissions from Saturn's magnetosphere. *Nature*, *292*(5825), 733–737. <https://doi.org/10.1038/292733a0>
- Hill, T. W. (1976). Interchange stability of a rapidly rotating magnetosphere. *Planetary and Space Science*, *24*(12), 1151–1154. [https://doi.org/10.1016/0032-0633\(76\)90152-5](https://doi.org/10.1016/0032-0633(76)90152-5)
- Jackman, C. M., & Arridge, C. S. (2011). Statistical properties of the magnetic field in the Kronian magnetotail lobes and current sheet. *Journal of Geophysical Research*, *116*(A5), A05224. <https://doi.org/10.1029/2010JA015973>
- Jackman, C. M., Arridge, C. S., Slavin, J. A., Milan, S. E., Lamy, L., Dougherty, M. K., & Coates, A. J. (2010). In situ observations of the effect of a solar wind compression on Saturn's magnetotail. *Journal of Geophysical Research*, *115*(A10), A10240. <https://doi.org/10.1029/2010JA015312>
- Jackman, C. M., Lamy, L., Freeman, M. P., Zarka, P., Cecconi, B., Kurth, W. S., et al. (2009). On the character and distribution of lower-frequency radio emissions at Saturn and their relationship to substorm-like events. *Journal of Geophysical Research*, *114*(A8), A08211. <https://doi.org/10.1029/2008JA013997>
- Jackman, C. M., Thomsen, M. F., & Dougherty, M. K. (2019). Survey of Saturn's magnetopause and bow shock positions over the entire Cassini mission: Boundary statistical properties and exploration of associated upstream conditions. *Journal of Geophysical Research: Space Physics*, *124*(11), 8865–8883. <https://doi.org/10.1029/2019JA026628>
- Kaiser, M. L., Desch, M. D., Warwick, J. W., & Pearce, J. B. (1980). Voyager detection of nonthermal radio emission from Saturn. *Science*, *209*(4462), 1238–1240. <https://doi.org/10.1126/science.209.4462.1238>
- Kanani, S. J., Arridge, C. S., Jones, G. H., Fazakerley, A. N., McAndrews, H. J., Sergis, N., et al. (2010). A new form of Saturn's magnetopause using a dynamic pressure balance model, based on in situ, multi-instrument Cassini measurements. *Journal of Geophysical Research*, *115*(A6), A06207. <https://doi.org/10.1029/2009JA014262>
- Kraus, J. D. (1966). *Radio astronomy* (pp. 116–125). McGraw-Hill.
- Lamy, L., Cecconi, B., Zarka, P., Canu, P., Schippers, P., Kurth, W. S., et al. (2011). Emission and propagation of Saturn kilometric radiation: Magnetoionic modes, beaming pattern, and polarization state. *Journal of Geophysical Research*, *116*(A4), A04212. <https://doi.org/10.1029/2010JA016195>
- Lamy, L., Zarka, P., Cecconi, B., Prangé, R., Kurth, W. S., & Gurnett, D. A. (2008). Saturn kilometric radiation: Average and statistical properties. *Journal of Geophysical Research*, *113*(A7), A07201. <https://doi.org/10.1029/2007JA012900>
- Lamy, L., Zarka, P., Cecconi, B., Prangé, R., Kurth, W. S., Hospodarsky, G., et al. (2018). The low-frequency source of Saturn' kilometric radiation. *Science*, *362*(6410). <https://doi.org/10.1126/science.aat2027>
- Li, D., & Yao, S. (2020). Stronger southward magnetic field and geoeffectiveness of ICMEs containing prominence materials measured from 1998 to 2011. *The Astrophysical Journal*, *891*(1), 79. <https://doi.org/10.3847/1538-4357/ab7197>
- Louarn, P., Kurth, W. S., Gurnett, D. A., Hospodarsky, G. B., Persoon, A. M., Cecconi, B., et al. (2007). Observation of similar radio signatures at Saturn and Jupiter: Implications for the magnetospheric dynamics. *Geophysical Research Letters*, *34*(20), L20113. <https://doi.org/10.1029/2007GL030368>
- Louis, C. K., Jackman, C. M., Mangham, S. W., Smith, K. D., O'Dwyer, E. P., Empey, A., et al. (2022). SPACE labelling tool version 2.0.0 (v2.0.0). *Zenodo*. <https://doi.org/10.5281/zenodo.6886528>
- Menietti, J. D., Averkamp, T. F., Ye, S.-Y., Persoon, A. M., Morooka, M. W., Groene, J. B., & Kurth, W. S. (2018). Extended survey of Saturn Z-mode wave intensity through Cassini's final orbits. *Geophysical Research Letters*, *45*(15), 7330–7336. <https://doi.org/10.1029/2018GL079287>
- Menietti, J. D., Mutel, R. L., Schippers, P., Ye, S.-Y., Gurnett, D. A., & Lamy, L. (2011). Analysis of Saturn kilometric radiation near a source center. *Journal of Geophysical Research*, *116*(A12), A12222. <https://doi.org/10.1029/2011JA017056>

- Menietti, J. D., Ye, S.-Y., Yoon, P. H., Santolik, O., Rymer, A. M., Gurnett, D. A., & Coates, A. J. (2009). Analysis of narrowband emission observed in the Saturn magnetosphere. *Journal of Geophysical Research*, *114*(A6), A06206. <https://doi.org/10.1029/2008JA013982>
- Menietti, J. D., Yoon, P. H., Pfsa, D., Ye, S.-Y., Santolik, O., Arridge, C. S., et al. (2016). Source region and growth analysis of narrowband Z-mode emission at Saturn. *Journal of Geophysical Research: Space Physics*, *121*(12), 11–929. <https://doi.org/10.1002/2016JA022913>
- Menietti, J. D., Yoon, P. H., Ye, S.-Y., Cecconi, B., & Rymer, A. M. (2010). Source mechanism of Saturn narrowband emission. *Annales Geophysicae*, *28*(4), 1013–1021. <https://doi.org/10.5194/angeo-28-1013-2010>
- Mitchell, D. G., Brandt, P. C., Carbary, J. F., Kurth, W. S., Krimigis, S. M., Paranicas, C., et al. (2015). Injection, interchange, and reconnection. In *Magnetotails in the solar system* (pp. 327–343). American Geophysical Union (AGU). <https://doi.org/10.1002/9781118842324.ch19>
- Morioka, A., Miyoshi, Y., Kasaba, Y., Sato, N., Kadokura, A., Misawa, H., et al. (2014). Substorm onset process: Ignition of auroral acceleration and related substorm phases. *Journal of Geophysical Research: Space Physics*, *119*(2), 1044–1059. <https://doi.org/10.1002/2013JA019442>
- Morioka, A., Miyoshi, Y., Tsuchiya, F., Misawa, H., Sakanoi, T., Yumoto, K., et al. (2007). Dual structure of auroral acceleration regions at substorm onsets as derived from AKR spectra. *Journal of Geophysical Research*, *112*(A6), A06245. <https://doi.org/10.1029/2006JA012186>
- Palmaerts, B., Radioti, A., Grodent, D., Yao, Z. H., Bradley, T. J., Roussos, E., et al. (2018). Auroral storm and polar arcs at Saturn—Final Cassini/UVIS auroral observations. *Geophysical Research Letters*, *45*(14), 6832–6842. <https://doi.org/10.1029/2018GL078094>
- Reed, J. J., Jackman, C. M., Lamy, L., Kurth, W. S., & Whiter, D. K. (2018). Low-frequency extensions of the Saturn Kilometric Radiation as a proxy for magnetospheric dynamics. *Journal of Geophysical Research: Space Physics*, *123*(1), 443–463. <https://doi.org/10.1002/2017JA024499>
- Scarf, F. L., & Gurnett, D. A. (1977). A plasma wave investigation for the Voyager Mission. *Space Science Reviews*, *21*(3), 289–308. <https://doi.org/10.1007/BF00211543>
- Tao, C., Kataoka, R., Fukunishi, H., Takahashi, Y., & Yokoyama, T. (2005). Magnetic field variations in the Jovian magnetotail induced by solar wind dynamic pressure enhancements. *Journal of Geophysical Research*, *110*(A11), A11208. <https://doi.org/10.1029/2004JA010959>
- Taubenschuss, U., Rucker, H. O., Kurth, W. S., Cecconi, B., Zarka, P., Dougherty, M. K., & Steinberg, J. T. (2006). Linear prediction studies for the solar wind and Saturn kilometric radiation. *Annales Geophysicae*, *24*(11), 3139–3150. <https://doi.org/10.5194/angeo-24-3139-2006>
- Thomsen, M. F., Jackman, C. M., & Lamy, L. (2019). Solar wind dynamic pressure upstream from Saturn: Estimation from magnetosheath properties and comparison with SKR. *Journal of Geophysical Research: Space Physics*, *124*(10), 7799–7819. <https://doi.org/10.1029/2019JA026819>
- Vasyliunas, V. M. (1983). Plasma distribution and flow. In A. J. Dessler (Ed.), *Physics of the Jovian magnetosphere* (pp. 395–453). Cambridge University Press.
- Wang, Z., Gurnett, D. A., Fischer, G., Ye, S.-Y., Kurth, W. S., Mitchell, D. G., et al. (2010). Cassini observations of narrowband radio emissions in Saturn's magnetosphere. *Journal of Geophysical Research*, *115*(A6), A06213. <https://doi.org/10.1029/2009JA014847>
- Wing, S., Brandt, P. C., Mitchell, D. G., Johnson, J. R., Kurth, W. S., & Menietti, J. D. (2020). Periodic narrowband radio wave emissions and inward plasma transport at Saturn's magnetosphere. *The Astronomical Journal*, *159*(6), 249. <https://doi.org/10.3847/1538-3881/ab818d>
- Wu, C. S., & Lee, L. C. (1979). A theory of the terrestrial kilometric radiation. *The Astronomical Journal*, *230*, 621–626. <https://doi.org/10.1086/157120>
- Wu, S., Ye, S., Fischer, G., Wang, J., Long, M., Menietti, J. D., et al. (2021). Statistical study on spatial distribution and polarization of Saturn narrowband emissions. *The Astrophysical Journal*, *918*(2), 64. <https://doi.org/10.3847/1538-4357/ac0af1>
- Wu, S. Y., Ye, S. Y., Fischer, G., Jackman, C. M., Wang, J., Menietti, J. D., et al. (2022). Reflection and refraction of the L-O Mode 5 kHz Saturn narrowband emission by the magnetosheath. *Geophysical Research Letters*, *49*(5), e2021GL096990. <https://doi.org/10.1029/2021GL096990>
- Ye, S.-Y., Fischer, G., Menietti, J. D., Wang, Z., Gurnett, D. A., & Kurth, W. S. (2011). An overview of Saturn narrowband radio emissions observed by Cassini RPWS. In H. O. Rucker, W. S. Kurth, P. Louarn, & G. Fischer (Eds.), *Planetary, solar and heliospheric radio emissions (PRE VII)* (pp. 99–113).
- Ye, S.-Y., Gurnett, D. A., Fischer, G., Cecconi, B., Menietti, J. D., Kurth, W. S., et al. (2009). Source locations of narrowband radio emissions detected at Saturn. *Journal of Geophysical Research*, *114*(A6), A06219. <https://doi.org/10.1029/2008JA013855>
- Ye, S.-Y., Menietti, J. D., Fischer, G., Wang, Z., Cecconi, B., Gurnett, D. A., & Kurth, W. S. (2010). Z mode waves as the source of Saturn narrowband radio emissions. *Journal of Geophysical Research*, *115*(A8), A08228. <https://doi.org/10.1029/2009JA015167>
- Zarka, P. (1998). Auroral radio emissions at the outer planets: Observations and theories. *Journal of Geophysical Research*, *103*(E9), 20159–20194. <https://doi.org/10.1029/98JE01323>
- Zarka, P., Cecconi, B., & Kurth, W. S. (2004). Jupiter's low-frequency radio spectrum from Cassini/Radio and Plasma Wave Science (RPWS) absolute flux density measurements. *Journal of Geophysical Research*, *109*(A9), A09S15. <https://doi.org/10.1029/2003JA010260>
- Zieger, B., & Hansen, K. C. (2008). Statistical validation of a solar wind propagation model from 1 to 10 AU. *Journal of Geophysical Research*, *113*(A8), A08107. <https://doi.org/10.1029/2008JA013046>

0.6 Chapter V

This chapter consists of an article published in *Frontiers in Astronomy and Space Science* titled 'The "SPectrogram Analysis and Cataloguing Environment (SPACE) Labelling Tool'. I contributed to this article through testing the software and contributing to discussions regarding changes to the software to promote the best user experience.



OPEN ACCESS

EDITED BY

K.-Michael Aye,
Freie Universität Berlin, Germany

REVIEWED BY

Mario D'Amore,
German Aerospace Center (DLR), Germany
Reinaldo Roberto Rosa,
National Institute of Space Research (INPE),
Brazil

*CORRESPONDENCE

Corentin Louis,
corentin.louis@dias.ie

SPECIALTY SECTION

This article was submitted to Space Physics,
a section of the journal Frontiers in
Astronomy and Space Sciences

RECEIVED 22 July 2022

ACCEPTED 21 October 2022

PUBLISHED 14 November 2022

CITATION

Louis C, Jackman C, Mangham S, Smith K,
O'Dwyer E, Empey A, Ceconi B,
Boudouma A, Zarka P and Maloney S
(2022), The "SPectrogram Analysis and
Cataloguing Environment" (SPACE)
labelling tool.
Front. Astron. Space Sci. 9:1001166.
doi: 10.3389/fspas.2022.1001166

COPYRIGHT

© 2022 Louis, Jackman, Mangham, Smith,
O'Dwyer, Empey, Ceconi, Boudouma,
Zarka and Maloney. This is an open-access
article distributed under the terms of the
[Creative Commons Attribution License \(CC
BY\)](https://creativecommons.org/licenses/by/4.0/). The use, distribution or reproduction in
other forums is permitted, provided the
original author(s) and the copyright
owner(s) are credited and that the original
publication in this journal is cited, in
accordance with accepted academic
practice. No use, distribution or
reproduction is permitted which does not
comply with these terms.

The "SPectrogram Analysis and Cataloguing Environment" (SPACE) labelling tool

Corentin Louis ^{1*}, Caitriona Jackman ¹,
Sam Mangham ², Kevin Smith ¹, Elizabeth O'Dwyer ¹,
Aaron Empey ¹, Baptiste Ceconi ³,
Adam Boudouma ³, Philippe Zarka ³ and
Shane Maloney ¹

¹School of Cosmic Physics, DIAS Dunsink Observatory, Dublin Institute for Advanced Studies, Dublin, Ireland, ²Department of Electronics & Computer Science, University of Southampton, Southampton, United Kingdom, ³LESIA, Observatoire de Paris, CNRS, PSL Research University, Meudon, France

The SPectrogram Analysis and Cataloguing Environment (SPACE) tool is an interactive python tool designed to label radio emission features of interest in a time-frequency map (called "dynamic spectrum"). The program uses Matplotlib's Polygon Selector widget to allow a user to select and edit an undefined number of vertices on top of the dynamic spectrum before closing the shape (polygon). Multiple polygons may be drawn on any spectrum, and the feature name along with the coordinates for each polygon vertex are saved into a ".json" file as per the "Time-Frequency Catalogue" (TFCat) format along with other data such as the feature id, observer name, and data units. This paper describes the first official stable release (version 2.0) of the tool.

KEYWORDS

python tools, labelling tool, planetary radio emission, solar radio emission, jupiter, saturn, earth, sun

1 Introduction

Non-thermal planetary radio emissions are produced by out-of-equilibrium populations of charged particles in planetary magnetospheres, and are observed at almost all strongly magnetized planets in our Solar System: the Earth, Jupiter, Saturn, Uranus and Neptune. The radio emissions can be divided into different classes, such as plasma waves, electromagnetic radio waves or electrostatic radio waves. It is highly desirable to select these distinct classes, which can often have characteristic frequency ranges, morphologies, or polarizations. Once catalogues of different emission types have been built up, that can enable large statistical studies unveiling both the average and extreme behaviour of planetary radio emissions.

There have been many long-running planetary spacecraft which have returned huge volumes of radio data and we have only scratched the surface of its analysis.

For example, the Cassini mission at Saturn spent 13 years studying the kronian system, revealing several components to its radio spectrum (Lamy et al., 2008; Taubenschuss et al., 2011; Ye et al., 2011; Lamy, 2017). Furthermore, the Wind spacecraft has spent almost 2 decades observing terrestrial (and solar) radio emissions from a range of vantage points near Earth (Bonnin et al., 2008; Waters et al., 2021; Fogg et al., 2022).

Significant efforts have been made in recent years to classify radio emissions from Jupiter, where the non-thermal radio emission is composed of half a dozen components (Louis et al., 2021c). These components overlap themselves in time and frequency, making automatic detection non-trivial. Therefore, manually cataloguing them is mandatory to be able to study them independently. Previous catalogues have been using square boxes to define the time and frequency intervals containing the radio signal (such as Leblanc, 2020a; Leblanc, 2020b; Leblanc, 2020c; Leblanc, 2020d; Leblanc, 2020e), but to be able to automatically disentangle the emissions when using the catalogue, it is then needed to construct catalogues with polygon vertices and with distinct labels. This was done by a few authors, primarily using tools built in IDL to construct such catalogues of Jupiter radio emissions Marques et al. (2017); Zarka et al. (2021). Once catalogues are built they can comprise training sets which form the basis of supervised machine learning approaches to classify larger samples of unseen data.

Here we present a Python user interface tool to allow the drawing of polygons around features in dynamic spectra. Section 2 describes the package, and an example of the use of this package. Section 3 summarises the version history of the code. Section 4 gives examples of the application of the catalogues produced by the tool. Section 5 presents some future avenues to continue to improve the tool.

2 The SPACE package

The SPectrogram Analysis and Cataloguing Environment (SPACE) tool is an interactive python tool designed to label radio emission features of interest in a time-frequency map (called a “dynamic spectrum”). The program enables users to create and edit the vertices of a polygon on the dynamic spectrum plot, before naming and saving it as a ‘feature’ in a catalogue for future analysis. Full usage documentation is available on the GitHub repository of the code (Louis et al., 2022) and directly at <https://space-labelling-tool.readthedocs.io>.

2.1 Installation

The code is available on an open-source GitHub repository (Louis et al., 2022), with full installation instructions present on

the repository page and on the ReadTheDocs webpage, and packed with the tool. It can easily be downloaded using git and installed using pip, with all prerequisites included in the provided requirements.txt file:

```
1 git clone https://github.com/CorentinLouis/
  SPACE_labelling_tool.git
2 pip install -e SPACE_labelling_tool
```

Listing 1: Download and Install SPACE using git and pip.

Installing in editable mode (“-e”) will allow the scripts to read any new or modified versions of the configuration files.

The code is also available from PyPi¹ and can be directly install using pip:

```
1 pip install SPACE-labelling-tool
```

Listing 2: Download and Install SPACE with pip.

2.2 Usage

Once installed using pip, the space labelling tool is available as a system-wide command `spacelabel`. It can then be used to view and label spacecraft observational data, by providing an input file in HDF5 or NASA CDF format (see Section 2.2.3 for specifics), and a time window to view. An example use is shown in Figure 1.

```
2 spacelabel [-h] [-se SPACECRAFT] e FILE e DATE
  DATE [-options]
```

Listing 3: System-wide command to run the space labelling tool - see Section 2.2.2 for more details on the -options.

Users may select any number of the measurement types present in the file (e.g., polarisation, flux and/or power), and view them all tiled on the screen. For example, Figure 1A displays Cassini Flux and Polarization radio data, while Figure 1B only displays Juno Flux radio data. Users can then click to select polygonal regions of the observation to label as features (top panel of Figure 1A). To close the polygon, users should click on the first drawn vertex of the polygon. Once done, a window pops up and ask to name the drawn feature appropriately (see top panel of Figure 1A). Features labelled in one view (e.g., intensity) appear simultaneously on the other views once they have been named (see bottom panel of Figure 1A), allowing users to easily see how a feature presents in multiple measurement types.

Once a region has been labelled, a user can pan their viewing window back and forth through the time range within the dataset by clicking on the Prev or Next buttons (see Figure 1), with an overlap applied between each view in order to facilitate

¹ <https://pypi.org/project/SPACE-labelling-tool/>

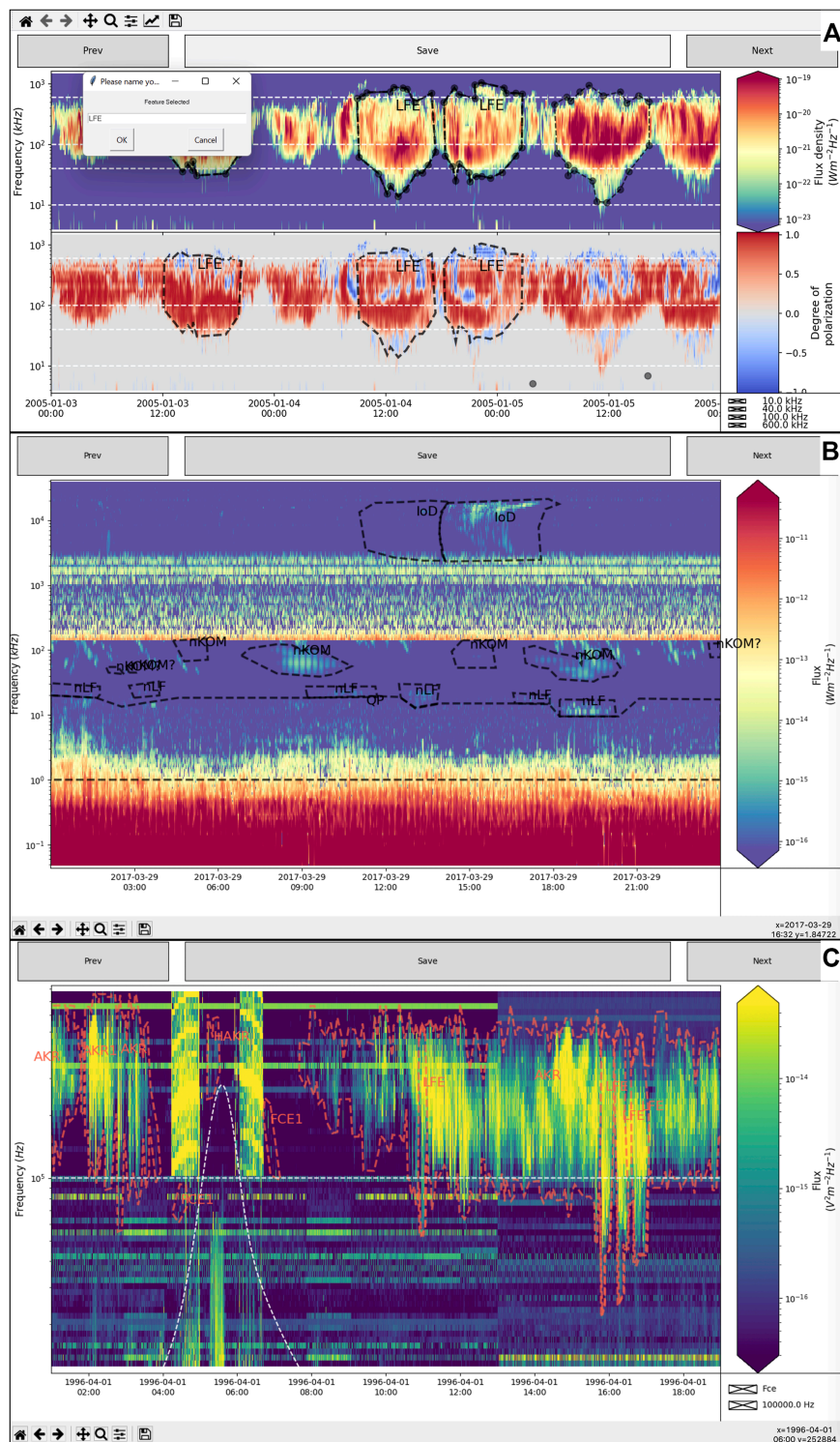


FIGURE 1

Examples of plots from the SPACE labelling Tool. Panel (A) displays Cassini/RPWS (Radio and Plasma Waves Science [Gurnett et al., 2004](#)) data ([Lamy et al., 2008, 2009](#)). The two panels show Intensity and Polarization data, respectively. At the top right of the top panel one can see a polygon that has just been drawn, with the window for naming the feature appearing at the top left of the graphics window. Other features have already been labelled, and appear in both intensity and polarisation views, with their names overlaid. The data displays in panel (B) are the estimated flux density ([Louis et al., 2021a,c](#)) from Juno/Waves measurements ([Kurth et al., 2017](#)), with the [Louis et al. \(2021b\)](#) catalogue overlaid. Panel (C) displays observations of Polar/PWI instrument ([Gurnett et al., 1995](#)) with the [Smith et al. \(2022\)](#) catalogue overlaid. The horizontal dashed-white line shows an example of the use of the -g [FREQUENCY GUIDE [FREQUENCY GUIDE ...]] option. The variable dashed-white line show that the tool is also able to read a 1D table from the CDF file (provided that this has been specified in the configuration file).

labelling features that lie on the edge of a window. Once finished, the labelled regions can be saved as a TFCat (Time-Frequency Catalogue) formatted JSON² file (Cecconi et al., 2022, this issue) by clicking on the Save button, and used later. If a user re-opens the same data file, or another data file with the same naming structure (e.g., observations_20180601_v02.cdf and observations_20180602_v02.cdf) saved features from previous sessions will be pre-loaded (see Figure 1).

Full usage documentation is available on the GitHub repository of the code (Louis et al., 2022) and directly at <https://space-labelling-tool.readthedocs.io>.

2.2.1 Procedure

When the code first opens a datafile, it compares the columns within to a selection of pre-made (and user-creatable) ‘configuration’ files for each type of input file (e.g., CDF, HDF5). Each describes a file in terms of the column names within it, and provides metadata for use in the tool - units and display names, and scaling factors that can be applied to change data stored in one unit into data viewed in another. If the data are in an unspecified format, the code will prompt the user to create a configuration file (see Section 2.2.3). Alternatively, if their data fit multiple configuration files, they will be prompted to select which they want to use (see Section 2.2.2).

Once a configuration has been determined, the code parses the observations and may re-bin the time into a coarser resolution in order to improve performance, taking the average of measurements in the new larger bins. It can also rescale the frequency data into evenly-spaced logarithmic bins between the minimum and maximum bins in the original data, as some data files have non-monotonic bin structures. When altering the frequency bins, measurements are logarithmically interpolated between the readings on the previous scale. Default adjustments can be defined in configuration files for file types, and may be over-ridden by command-line arguments to the tool. The parsed and adjusted data are then re-saved as a compressed HDF5 file, reducing both the size of the data and time to access.

The pre-processed data are then displayed to the screen using Matplotlib (Hunter, 2007), in a window the size of the user’s initial time range. The dynamic range of the data is constrained to improve visibility of features; displaying, by default, the 5th-95th quantiles of the signal for each measurement (to prevent anomalously low or high values overly-compressing the ranges of interest, reducing the ability to discern features). GUI buttons allow users to pan between time windows of equivalent size - with each window will overlap the previous window by 25% in the direction of travel. Features can then be defined by drawing polygons on the time window using the Matplotlib Polygon Selector widget. There are the detailed interactive components of the Matplotlib window:

- Measurements: Each panel displays a measurement, with name, scale and units on the right. Features can be drawn by clicking to add coordinates, and completed by clicking on the first coordinate added again. The vertices of the polygon can be modified before completed the polygon:
 - Hold the ctrl key and click and drag a vertex to reposition it before the polygon has been completed.
 - Hold the shift key and click and drag anywhere in the axes to move all vertices.
 - Press the esc key to start a new polygon.

Once selected, a feature can be named (see Figure 1A). Features can be selected on any pane, and will be mirrored on all other panes.

- Prev/Next buttons: These move through the data by an amount equal to the width of time range selected. This will also overlap 1/4 of the current window as ‘padding’.
- Save button: This will save any features to TFCat JSON format, as catalogue_OBSERVER_NAME.json.
- Check boxes: If the option -g [FREQUENCY_GUIDE [FREQUENCY_GUIDE ...]] has been enabled by the users (e.g., fixed frequency lines in Figures 1A,C), or if a 1D variable is contained in the input data and configuration files (e.g., Fce Figure 1C) check boxes will appear in the lower right hand corner of the figure to make the white dotted lines appear or disappear.

Once finished, you can save and then close the figure using the normal close button.

2.2.2 Options

The user must specify the path to the file they want to visualise (or ‘first’ file in a collection, e.g., of CDF files), along with the start and end dates of their initial viewing window, in ISO year-month-day hour:minute:second format (e.g., 2018-06-12 18:00:01). However, there are further options available:

- -f FREQUENCY_BINS: Rescales the data to this many evenly-spaced logarithmic bins. Overrides any default set in the configuration files.
- -t MINIMUM_TIME_BIN: Rebins the data to time bins of this size, if it is currently more finely binned. The bin size need to be given in second.
- -s SPACECRAFT: Specifies the name of the spacecraft configuration file to use, if multiple describe the datafile the user has provided.
- -fig_size FIGURE_SIZE FIGURE_SIZE: x and y dimension of the matplotlib figure (by default: 15 9).
- -frac_dyn_range FRAC_MIN FRAC_MAX: Defines the dynamic range of the colour bar in the visualisation, as a fraction of the distribution of values in the data file. This

² <https://www.json.org/>

must be numbers between 0 and 1. Default values are 0.05 and 0.95 (the 5th-95th quantiles of the displayed signal).

- `-cmap CMAP`: The name of the color map that will be used for the intensity plot (by default: viridis).
- `-cfeatures CFEATURES`: The name of the colour for the saved features of interest polygons (by default: tomato).
- `-thickness_features TFEATURES`: The thickness value for the saved features of interest polygons (by default: 2).
- `-size_features_name SFEATURESNAME`: The font size for the name of the saved features of interest polygons (by default: 14).
- `-g [FREQUENCY_GUIDE [FREQUENCY_GUIDE ...]]`: Draws horizontal line(s) on the visualisation at these specified frequencies to aid in interpretation of the plot. Values must be in the same units as the data. Lines can be toggled using check boxes.
- `-not_verbose`: If `not_verbose` is called, the debug log will not be printed. By default: verbose mode.

2.2.3 Input formats

The code is designed to cope with input files in a variety of file formats and column formats by use of configuration files, several of which are pre-provided. HDF5 input files require at least three datasets, corresponding to observation time (floats, in MJD), frequency range (floats, in any arbitrary unit) and at least one measurement, stored with frequency as the rows and observation as the columns. The names and units for each measurement (in LaTeX form) must be provided in a configuration file, in easily-editable JSON format. The appropriate configuration files are automatically-selected by the code from those available - making it easy to work with HDF5 files from a variety of collaborators with arbitrary naming schemes.

CDF files in NASA format are more structured, and can be read in either singly or as a collection, combining all files in the directory matching the naming scheme `[...]_YYYYMMDD[...].cdf` into a single pre-processed data file. As with the HDF5 files, CDF files must contain a frequency attribute (floats, in any arbitrary unit) and a time attribute (either in TT_2000 or CDF_EPOCH format, which is parsed using Astropy, Price-Whelan et al., 2018) and at least one measurement, stored with frequency as the rows and observation as the columns.

The code can easily be expanded to ingest other file formats (see Section 2.3.2).

2.3 Structure

2.3.1 'Model-View-Presenter' architecture

The code is designed using a standard object-oriented 'Model-View-Presenter' architecture, with strong separation between the data input and management, and the visualisation.

This allows for easy development of both new input file-types (see Section 2.3.2) and pre-processing options, and alternative GUI front-ends and settings (see Section 5 for suggested development building on top of this flexibility). A generic 'Presenter' controls the logic of the program, and feeds data from the data models to the selected GUI view, and requests from the GUI for changes to the data models. Either the 'View' or 'Model' can be easily interchanged as long as they conform to the API expected by the 'Presenter'.

Full development documentation is available on the GitHub repository of the code (Louis et al., 2022) and directly at <https://space-labelling-tool.readthedocs.io>.

2.3.2 Addition of new input formats

New input formats can be easily added by extending the base DataSet class included in the code. A developer only needs to define the routines for inputting the data from file; the code will then handle pre-processing and data access.

3 History of the code

The first version of the labelling code was developed in IDL by P. Zarka. It allowed users to read data from an IDL saveset (sav format), draw polygons around features of interest and label them. However, this IDL version had to be adapted to each new dataset. This code has been used to build many catalogues based on different observers (such as the Nançay Decameter Array (NDA) ground-based radio telescope (Marques et al., 2017), or the Cassini (Zarka et al., 2021) or Juno (Louis et al., 2021c,b) spacecraft).

The second version of the labelling tool was written in Python and was the first to be officially released (Empey et al., 2021). This version allowed to automatically read any dataset in sav or cdf format, based on the information requested from users from the terminal. The other main improvements compared to the previous version were the number of vertices in the polygons (unlimited) and the possibility to modify the vertices position during the polygon drawing (using the Matplotlib's Polygon Selector widget), as well as the production of the catalogue directly in TFCat format.

The current version (Louis et al., 2022) brings a large number of improvements, both in terms of architecture, usability and ergonomics, which are described in the previous sections.

The SPACE tool has also joined the MASER service (Ceconi et al., 2020).

4 Applications

Once a catalogue has been produced, it can also be displayed using the SPACE labelling Tool (see Figure 1 or the Autoplot

Software (Faden et al., 2010). For an example, the reader is invited to visit the web page <https://doi.org/10.25935/nhb2-wy29> where an autoplot template file is given to display the Juno data (Louis et al., 2021a) and the Louis et al. (2021b) catalogue overlaid in autoplot. See Cecconi et al. (2022, this issue) for more information about the display of a Catalogue using Autoplot. The catalogue can be used to study the different components of the radio emission spectrum, e.g. as done by Louis et al. (2021c), where the data can then be automatically selected using the catalogue *via* a mask or an inverse-mask. In the case presented in Figure 1, not every type of emission is labelled, but in each frequency range (kilometric or hectometric) only one radio component remains. We can then study the components one by one [e.g., their latitudinal distribution, as in Louis et al. (2021c), their distribution as a function of observer's or Sun's longitude, as in Zarka et al. (2021), or their distribution *versus* observer's longitude and satellite (Io) phase as in Marques et al. (2017)].

With the SPACE labelling Tool, we are also providing some useful routines to use the catalogue³.

These catalogues can also then be used to train machine learning algorithm to detect automatically the radio emissions in past (Cassini, NDA) or future observation (such as Juno, JUICE, NDA).

5 Limitations and future work

The code is ready for distribution and use, but has some technical limitations. Potential works to address those limitations, and avenues of future development, are:

- Performance: The Matplotlib-based front-end can struggle when provided with especially high resolutions of data, or over large time windows. Rebinning features exist to mitigate this, but an alternative rendering framework could be employed (e.g., datashader⁴), and/or the performance of the interactive front-end components could be improved if re-implemented in a more performant framework [e.g., Plotly Inc. (2015)].
- Scalability: The code loads all the data provided into memory at launch, limiting its applicability for large datasets. Whilst this can be mitigated by the feature to allow appending to TFCat files created by data files sharing filename formats, a 'deferred load' approach would be better. This would be best accomplished using the Dask and XArray libraries (Dask Development Team, 2016; Hoyer and Hamman, 2017).

- Configurations: The code depends heavily on pre-written configuration files, and can prompt users to create missing ones - but does not yet contain a 'wizard' or automatic walkthrough to aid users in creating them.
- Platform: Run the SPACE labelling tool in a notebook (launch on Binder).
- Catalogue integration: The modular format of the code would make it possible to create 'dataset' types that access and download data directly from online catalogues, maintaining local caches.

Data availability statement

The code of the SPACE labelling Tool is open-source and freely available on github (Louis et al., 2022). The Cassini/RPWS dataset displayed in Figure 1A, produced by Lamy et al. (2008) is available at <https://doi.org/10.25935/ZKXB-6C84> (Lamy et al., 2009). The Juno/Waves dataset displayed in Figure 1B, produced by Louis et al. (2021c), is accessible at <https://doi.org/10.25935/6jg4-mk86> (Louis et al., 2021a), and the catalogue can be download at <https://doi.org/10.25935/nhb2-wy29> (Louis et al., 2021b). The Polar/PWI dataset displayed in Figure 1C is accessible through the CDAWeb at <https://cdaweb.gsfc.nasa.gov/pub/data/polar/pwi/>.

Author contributions

CL and CJ led the development of the SPACE Labelling Tool. CL wrote the paper and worked on the development of the code. PZ developed the first IDL version of the code. AE developed the first python version of the code. SM worked on the development of the second version of the code. SWM developed the current version of the code. EO tested the different versions of the code, and gave inputs to the developers of the code. AB helped run the code on a virtual machine environment, and made changes on the plotting functions to the latest version of the code. AB helped run the code on a virtual machine environment, and made changes on the plotting functions to the latest version of the code. KS added features to the latest version of the code. EO, AB, and KS wrote useful routines to read, modify and use the output catalogue. BC led the TFCat format of the catalogues. All the co-authors have contributed to the writing of the paper.

Funding

CLs, CJ's, EO's, and AE's work at the Dublin Institute for Advanced Studies was funded by Science Foundation Ireland Grant 18/FRL/6199. SWM's work at the University of

³ <https://github.com/elodwyer/Functions-for-SPACE-Labelling-Tool>

⁴ datashader.org

Southampton Research Software Group was funded by a grant *via* the Alan Turing Institute. KS's work at the Dublin Institute for Advanced Studies was funded by a 2022 SCOSTEP/PRESTO Grant. The Europlanet 2024 Research Infrastructure project has received funding from the European Union's Horizon 2020 research and innovation programme under grant agreement No 871149.

Acknowledgments

CL thanks A. Loh and S. Lion for their very helpful comments on the development phase of the code. CL also gives special thanks to R. Prangée for finding errors that no one had seen.

References

- Bonnin, X., Hoang, S., and Maksimovic, M. (2008). The directivity of solar type III bursts at hectometer and kilometer wavelengths: Wind-Ulysses observations. *Astronomy Astrophys* 489, 419–427. doi:10.1051/0004-6361:200809777
- Cecconi, B., Loh, A., Sidaner, P. L., Savalle, R., Bonnin, X., Nguyen, Q. N., et al. (2020). Maser: A science ready toolbox for low frequency radio Astronomy. *Data Sci. J.* 19, 1062. doi:10.5334/dsj-2020-012
- Cecconi, B., Louis, C. K., Bonnin, X., Loh, A., and Taylor, M. B. (2022). *TFCat (Time-Frequency catalogue): JSON implementation and Python library*. *Frontiers in astronomy and space sciences*. This issue.
- Dask Development Team (2016). *Dask: Library for dynamic task scheduling*. <https://dask.org>
- Empey, A., Louis, C. K., and Jackman, C. M. (2021). *SPACE labelling tool*. version 1.1.0. [Code]. doi:10.5281/zenodo.5636922
- Faden, J. B., Weigel, R. S., and Merka, J., (2010). Autoplot: A browser for scientific data on the web. *Earth Sci. Inf.* 3, 41–49. doi:10.1007/s12145-010-0049-0
- Fogg, A. R., Jackman, C. M., Waters, J. E., Bonnin, X., Lamy, L., Cecconi, B., et al. (2022). Wind/WAVES observations of auroral kilometeric radiation: Automated burst detection and terrestrial solar Wind - magnetosphere coupling effects. *JGR. Space Phys.* 127, e30209. doi:10.1029/2021JA030209
- Gurnett, D. A., Kurth, W. S., Kirchner, D. L., Hospodarsky, G. B., Averkamp, T. F., Zarka, P., et al. (2004). The Cassini radio and plasma wave investigation. *Space Sci. Rev.* 114, 395–463. doi:10.1007/s11214-004-1434-0
- Gurnett, D. A., Persoon, A. M., Randall, R. F., Odem, D. L., Remington, S. L., Averkamp, T. F., et al. (1995). The polar plasma wave instrument. *Space Sci. Rev.* 71, 597–622. doi:10.1007/bf00751343
- Hoyer, S., and Hamman, J. (2017). xarray: N-D labeled arrays and datasets in Python. *J. Open Res. Softw.* 5, 10. doi:10.5334/jors.148
- Hunter, J. D. (2007). Matplotlib: A 2d graphics environment. *Comput. Sci. Eng.* 9, 90–95. doi:10.1109/MCSE.2007.55
- Kurth, W. S., Hospodarsky, G. B., Kirchner, D. L., Mokrzycki, B. T., Averkamp, T. F., Robison, W. T., et al. (2017). The Juno waves investigation. *Space Sci. Rev.* 213, 347–392. doi:10.1007/s11214-017-0396-y
- Lamy, L., Cecconi, B., and Zarka, P. (2009). *Cassini/RPWS/HFR LESIA/kronos SKR data collection*. Version 1.0. [Data set]. doi:10.25935/ZKXB-6C84
- Lamy, L. (2017). "The saturnian kilometeric radiation before the Cassini grand finale," in *Planetary radio emissions (PRE-VIII)*. Editors G. Fischer, G. Mann, and M. Panchenko, (Vienna: Austrian Academy of Sciences Press). 455–466. doi:10.1553/PRE8s455
- Lamy, L., Zarka, P., Cecconi, B., Prangé, R., Kurth, W. S., and Gurnett, D. A. (2008). Saturn kilometeric radiation: Average and statistical properties. *J. Geophys. Res.* 113, A07201. doi:10.1029/2007JA012900
- Leblanc, Y. (2020a). *A catalogue of Jovian decametric radio observations from January 1978 to December 1979*. Digitised version. [Data set]. doi:10.25935/GXZF-ZT33
- Leblanc, Y. (2020b). *A catalogue of Jovian decametric radio observations from January 1982 to December 1984*. Digitised version. Data set. doi:10.25935/403B-VA51
- Leblanc, Y. (2020c). *A catalogue of Jovian decametric radio observations from January 1985 to December 1987*. Digitised version. [Data set]. doi:10.25935/gh59-py87
- Leblanc, Y. (2020d). *A catalogue of Jovian decametric radio observations from January 1988 to December 1990*. Digitised version. [Data set]. doi:10.25935/cmqb-ij10
- Leblanc, Y. (2020e). *A catalogue of Jovian radio observations from January 1980 to December 1981*. Digitised version. [Data set]. doi:10.25935/RAS0-ER93
- Louis, C. K., Jackman, C. M., Mangham, S. W., Smith, K. D., O'Dwyer, E., Empey, A., et al. (2022). *SPACE labelling tool*. Version 2.0.0. [Code]. doi:10.5281/zenodo.6886528
- Louis, C. K., Zarka, P., and Cecconi, B. (2021a). *Juno/Waves estimated flux density Collection*. Version 1.0. doi:10.25935/6jg4-mk86
- Louis, C. K., Zarka, P., Cecconi, B., and Kurth, W. S. (2021b). *Catalogue of Jupiter radio emissions identified in the Juno/Waves observations*. Version 1.0. doi:10.25935/nhb2-wy29
- Louis, C. K., Zarka, P., Dabidin, K., Lampson, P. A., Magalhães, F. P., Boudouma, A., et al. (2021c). Latitudinal beaming of jupiter's radio emissions from juno/waves flux density measurements. *JGR. Space Phys.* 126, e29435. doi:10.1029/2021JA029435
- Marques, M. S., Zarka, P., Echer, E., Ryabov, V. B., Alves, M. V., Denis, L., et al. (2017). Statistical analysis of 26 yr of observations of decametric radio emissions from Jupiter. *Astron. Astrophys.* 604, A17. doi:10.1051/0004-6361/201630025
- Plotly Inc (2015). *Collaborative data science*. <https://plot.ly>
- Price-Whelan, A. M., Sipőcz, B., Günther, H., Lim, P., Crawford, S., Conseil, S., et al. (2018). The astropy project: Building an open-science project and status of the v2.0 core package. *Astronomical J.* 156, 123. doi:10.3847/1538-3881/aabc4f
- Smith, K. D., Louis, C. K., Jackman, C. M., Fogg, A. R., O'Dwyer, E., Waters, J. E., et al. (2022). Catalogue of Auroral Kilometeric Radiations (AKR) observed by the Polar spacecraft (1.1). *Zenodo*. doi:10.5281/zenodo.7235986

Conflict of interest

The authors declare that the research was conducted in the absence of any commercial or financial relationships that could be construed as a potential conflict of interest.

Publisher's note

All claims expressed in this article are solely those of the authors and do not necessarily represent those of their affiliated organizations, or those of the publisher, the editors and the reviewers. Any product that may be evaluated in this article, or claim that may be made by its manufacturer, is not guaranteed or endorsed by the publisher.

Taubenschuss, U., Leisner, J. S., Fischer, G., Gurnett, D. A., and Nemeč, F. (2011). "Saturnian low-frequency drifting radio bursts: Statistical properties and polarization," in *Planetary, solar and heliospheric radio emissions (PRE VII)*. Editors H. O. Rucker, W. S. Kurth, P. Louarn, and G. Fischer (Vienna: Austrian Academy of Sciences Press), 115–123.

Waters, J. E., Jackman, C. M., Lamy, L., Cecconi, B., Whiter, D. K., Bonnin, X., et al. (2021). Empirical selection of auroral kilometric radiation during a multipoint remote observation with Wind and Cassini. *JGR. Space Phys.* 126, e29425. doi:10.1029/2021JA029425

Ye, S. Y., Fischer, G., Menietti, J. D., Wang, Z., Gurnett, D. A., and Kurth, W. S. (2011). "An overview of Saturn narrowband radio emissions observed by Cassini RPWS," in *Planetary, solar and heliospheric radio emissions (PRE VII)*. Editors H. O. Rucker, W. S. Kurth, P. Louarn, and G. Fischer. (Vienna: Austrian Academy of Sciences Press), 99–113.

Zarka, P., Magalhães, F. P., Marques, M. S., Louis, C. K., Echer, E., Lamy, L., et al. (2021). Jupiter's auroral radio emissions observed by Cassini: Rotational versus solar Wind control, and components identification. *JGR. Space Phys.* 126, e29780. doi:10.1029/2021JA029780

0.7 Code

In this work, we have produced a number of github repositories to accompany the studies described in chapter I and chapter II. These repositories can be found at O'Dwyer et al. (2023b) and O'Dwyer et al. (2023d). In figure 1. a screen-grab of the webpages for these repositories is displayed.

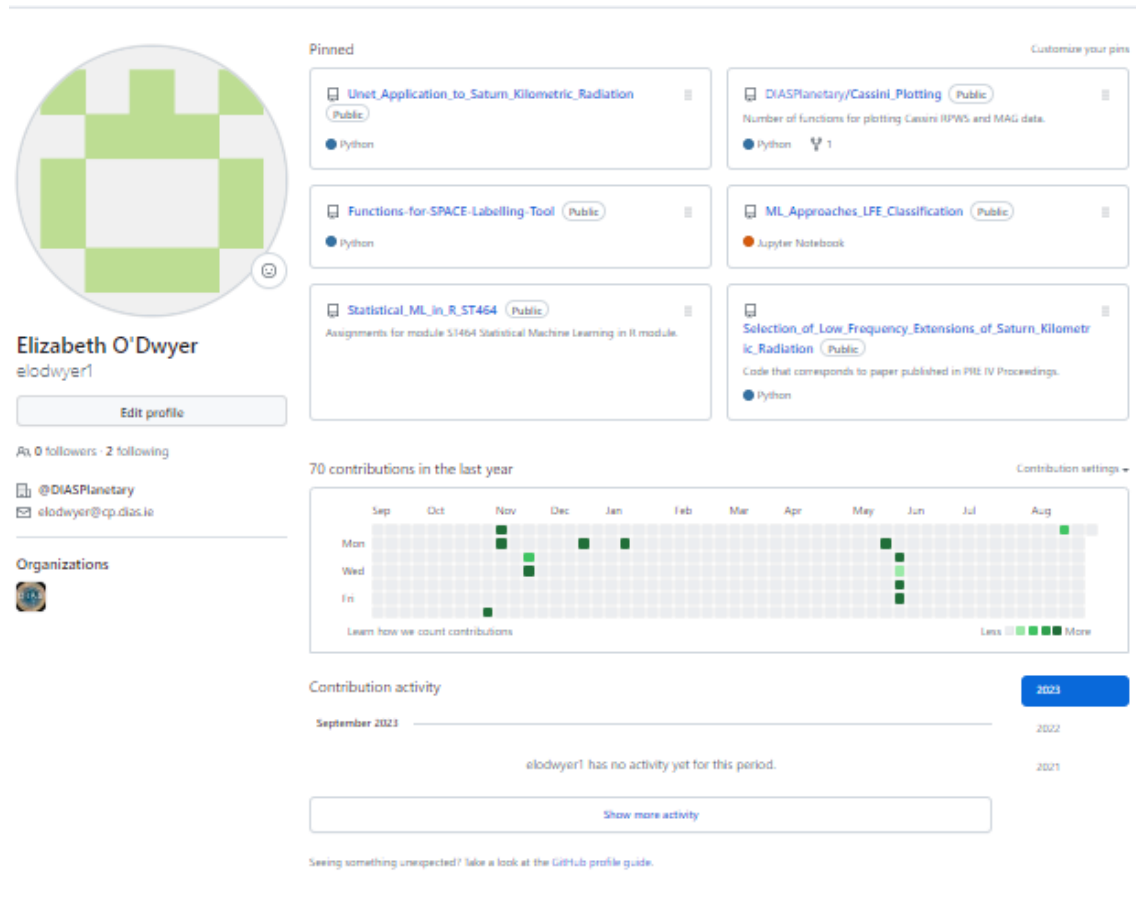


FIGURE 1: Screen-grab of Github showing repositories accompanying work described in chapters I and II.

0.8 Datasets

In this work, we have produced two datasets that can be found at O'Dwyer et al. (2023a) and O'Dwyer et al. (2023c). In figures 2 and 3, we show screen-grabs of the zenodo web pages corresponding to these datasets.



FIGURE 2: Screen-grab from Zenodo page showing the dataset found at O'Dwyer et al. (2023a)

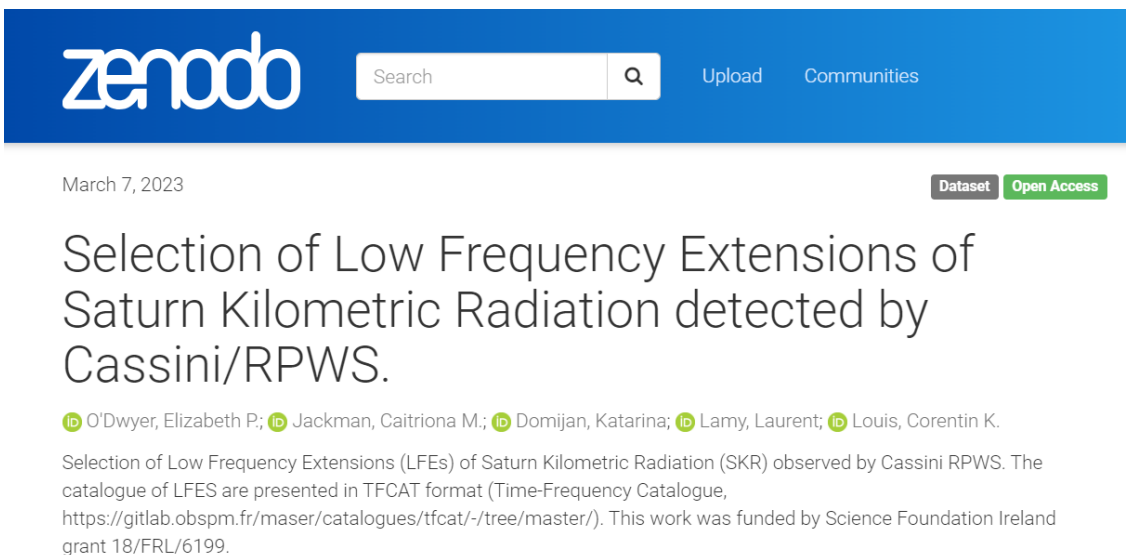


FIGURE 3: Screen-grab from Zenodo page showing the dataset found at O'Dwyer et al. (2023c)

0.9 Conclusion

In summary, this thesis details the generation of a manually selected list of LFEs of SKR, which are subsequently used in the training of a ML model for semantic segmentation.

In chapter I, the visual criteria for the manual LFE selection is described as well as the six subclasses of LFE defined in this catalogue. 984 LFEs were selected and the subclasses are listed as follows ‘LFE’, ‘LFE_{sm}’, ‘LFE_{sp}’, ‘LFE_{ext}’, ‘LFE_m’ and ‘LFE_{dg}’. The selection of LFEs was mainly carried out in 2006 and 2008, along with the inclusion of a small sample from other years of the mission. We refer to previous studies as a basis for the physical interpretation of the classes ‘LFE’ and ‘LFE_m’, which consist of typical LFEs and LFEs with a duration longer than ~ 11 hrs respectively. Reed et al. (2018) used a semi-automated method for selection of LFEs detected by Cassini in 2006 based on intensity thresholds in the 40-100 kHz frequency band and the 100-600 kHz frequency band. The LFEs found were separated into long (>20 hours) and short (<20 hours). Reed et al. (2018) suggested that long LFEs result from solar wind compressions of the magnetosphere and short LFEs from internally-driven tail reconnection, this affirms the work by Jackman et al. (2009) who used SKR LFEs at Saturn to diagnose tail reconnection. ‘LFE_{ext}’ class describes an LFE with an extinction in emission in some or all of the main band frequencies, studies by Lamy et al. (2008b) and Lamy et al. (2008a) investigate this visibility effect. Lamy et al. (2008a) quantitatively found there to be an extinction in main band frequencies for observers at latitudes $> 60^\circ$ in both hemispheres.

We used this catalogue of LFEs to find periods of ‘NoLFE’ during the Cassini mission. This ‘NoLFE’ label is taken to mean periods of time where we observe normal SKR, narrowband emission or in fact no emission at all. As discussed, LFEs have been linked to internally driven tail reconnection and solar wind compressions of the magnetosphere (Jackman et al., 2009; Reed et al., 2018), ‘NoLFE’ periods with normal SKR can be interpreted as periods of time where the SKR sources are not extended to higher altitudes as a result of said internally driven tail reconnection or solar wind compressions of the magnetosphere. ‘NoLFE’ periods with no emission may be the result of visibility effects where Cassini hasn’t been in the position to detect SKR. They may also simply represent more quiescent intervals of magnetospheric dynamics.

In figure 3 of chapter I, we see a 5-panel plot with panels (c-d) showing counts vs Range (RS), Latitude ($^{\circ}$) and Local Time (hours) for Cassini's trajectory (grey dotted), total LFEs labelled (blue) and non-LFEs labelled (orange). In panel (d), for the LFEs, we see a peak in the early morning local time, a wide peak between 10-15 hours LT, and a deep trough at 18 hours, followed by an increase again. The non-LFE curve has two peaks at approximately 11 and 24 hours. We see significantly lower values in between these peaks. The non-LFE curve suggests that the non-LFE population is more sensitive to LT, with more severe peaks and troughs than the LFE curve. This could be due to the fact that non-LFE events consist of both periods with SKR and periods with no emission, making it more difficult to interpret. SKR visibility is strongly impacted by the position of the observer, this could be a contributing factor to the non-uniform distribution observed for the LFE and non-LFE events. Lamy et al. (2009) found that the intensity of SKR varies with LT, with a full width half maximum occurring at approximately 08:00 hrs LT.

In chapter II, the implementation of this catalogue as a training set for a Unet based approach for semantic segmentation of LFEs in the Cassini/RPWS dataset is described. The model was trained on a set of 1533 images (996 training and 537 validation) which consisted of images with an LFE and without, along with augmented images. We found median IoU values of 0.97 and 0.98 for the testing and training set respectively after implementing a post-processing step. The model made predictions on the entire Cassini/RPWS dataset by inputting images with overlapping start and end times and computing the average of the model prediction for the overlapping segments. 4874 LFEs were found in total using this method. Of these 4874, 3166 are of type 'LFE', 839 are of type 'LFE_m' and 869 of type 'LFE_{sm}'. Following analysis of the predictions over time, LFEs are predicted at all stages of the mission, with a higher occurrence rate from 2004 to mid-2009. The reasoning for this higher occurrence rate is unclear. It may be partly due to the fact the histogram displays occurrences of LFEs, i.e. number of LFEs that occurred in a given time range. It does not account for the duration of the LFEs, perhaps later in the mission we see higher counts of the LFE_m class (long duration LFEs) and so this impacts the distribution of the data shown. It is well known that SKR visibility is strongly impacted by the position of the observer, this may also be a contributing factor to the counts of LFEs observed after 2010.

In figure 4, we have plotted the output of the Unet model in the same style as chapter 1, figure 3 (d, e). In panels (a, b), we have plotted counts vs latitude ($^{\circ}$) and LT (Hrs) for the total Cassini trajectory (gray dotted) and the LFEs detected by the Unet model (blue). The panels (c, d) show the same plot but with the training LFEs in blue and No-LFE periods in orange. In panels (a) and (b), we can see that the distribution of both latitude and LT for the Unet output follows that of Cassini's total trajectory quite closely. As mentioned previously, the distribution of counts vs LT for the training LFEs does not follow the distribution of Cassini's total trajectory. This is indicative that the LT distribution of training LFEs is not an artefact of the selection method, but rather a result of the sampling. LFEs were labelled from most of 2006, three months from 2008 and a smaller sample from almost all other years of the mission. The aim was to sample data from a diverse range of spacecraft locations to permit the model to detect LFEs that are subject to visibility effects. From panels (a, b) of figure 4, this appears to have been done successfully.

The catalogue in the format of frequency-time coordinates for each LFE is available for use amongst the scientific community, The intended purpose is for a large statistical study in order to further explore the characteristics of LFEs and the role of internal and external drivers in LFE generation.

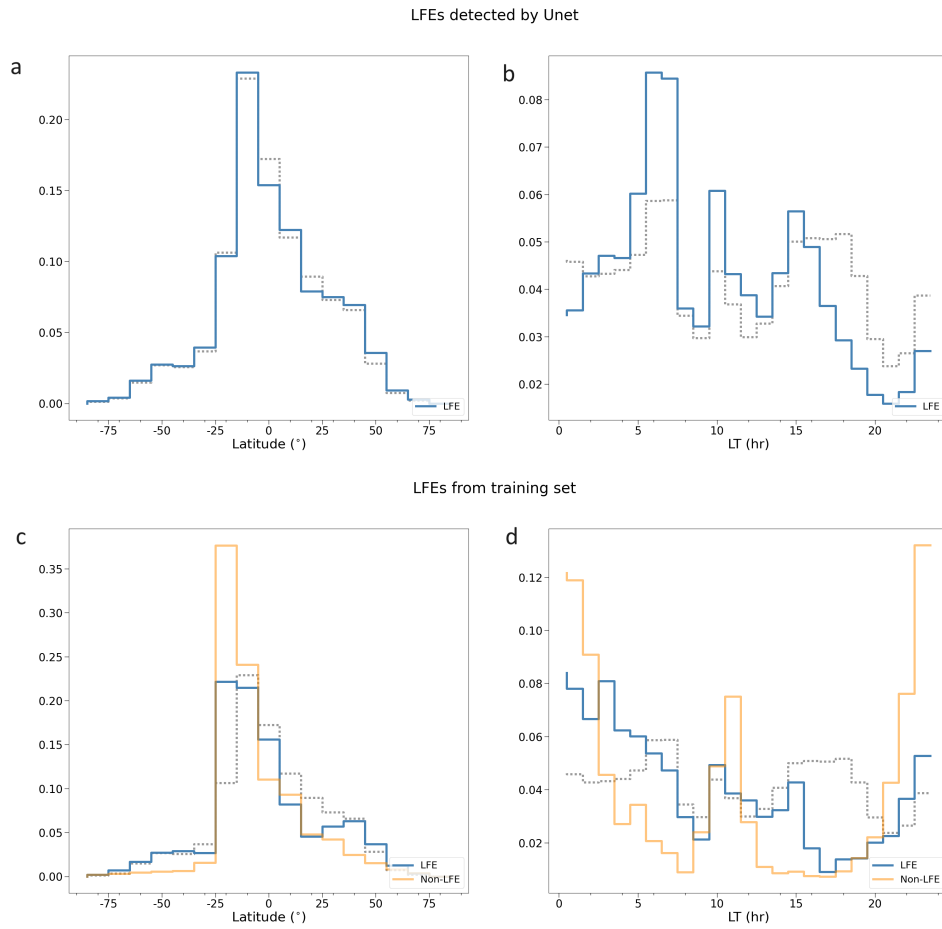


FIGURE 4: 4-panel plot showing histograms of counts vs Latitude ($^{\circ}$) (a, c) and Local Time (hours) (b, d). In panels (a, b) Cassini's trajectory (grey dotted) and the LFEs detected by the Unet (blue) are plotted, and panels (c, d) Cassini's trajectory (grey dotted), the training LFEs (blue) and non-LFE periods (orange) are plotted.

Bibliography

- Bunce, E. J. et al. (2005). "In situ observations of a solar wind compression-induced hot plasma injection in Saturn's tail". In: *Geophysical Research Letters* 32.20. DOI: <https://doi.org/10.1029/2005GL022888>. eprint: <https://agupubs.onlinelibrary.wiley.com/doi/pdf/10.1029/2005GL022888>. URL: <https://agupubs.onlinelibrary.wiley.com/doi/abs/10.1029/2005GL022888>.
- Cecconi, B. and P. Zarka (May 2005). "Direction finding and antenna calibration through analytical inversion of radio measurements performed using a system of two or three electric dipole antennas on a three-axis stabilized spacecraft". In: *Radio Science* 40.3, RS3003, RS3003. DOI: [10.1029/2004RS003070](https://doi.org/10.1029/2004RS003070).
- Galopeau, Patrick H. M. and Alain Lecacheux (2000). "Variations of Saturn's radio rotation period measured at kilometer wavelengths". In: *Journal of Geophysical Research: Space Physics* 105.A6, pp. 13089–13101. DOI: <https://doi.org/10.1029/1999JA005089>. eprint: <https://agupubs.onlinelibrary.wiley.com/doi/pdf/10.1029/1999JA005089>. URL: <https://agupubs.onlinelibrary.wiley.com/doi/abs/10.1029/1999JA005089>.
- He, Kaiming et al. (2017). "Mask r-cnn". In: *Proceedings of the IEEE international conference on computer vision*, pp. 2961–2969.
- Jackman, C. M. et al. (2009). "On the character and distribution of lower-frequency radio emissions at Saturn and their relationship to substorm-like events". In: *Journal of Geophysical Research: Space Physics* 114.A8. DOI: <https://doi.org/10.1029/2008JA013997>. eprint: <https://agupubs.onlinelibrary.wiley.com/doi/pdf/10.1029/2008JA013997>. URL: <https://agupubs.onlinelibrary.wiley.com/doi/abs/10.1029/2008JA013997>.
- Kaiser, M. L. and M. D. Desch (1984). "Radio emissions from the planets Earth, Jupiter, and Saturn". In: *Reviews of Geophysics* 22.4, pp. 373–384. DOI: <https://doi.org/10.1029/RG022i004p00373>. eprint: <https://agupubs.onlinelibrary.wiley.com/doi/>

-
- [pdf/10.1029/RG022i004p00373](https://doi.org/10.1029/RG022i004p00373). URL: <https://agupubs.onlinelibrary.wiley.com/doi/abs/10.1029/RG022i004p00373>.
- Kaiser, M L et al. (1980). "Voyager Detection of Nonthermal Radio Emission from Saturn". In: *Science* 209, pp. 1238–1240.
- Lamy, L. (Jan. 2017). "The Saturnian kilometric radiation before the Cassini Grand Finale". In: *Planetary Radio Emissions VIII*. Ed. by G. Fischer et al., pp. 171–190. DOI: [10.1553/PRE8s171](https://doi.org/10.1553/PRE8s171).
- Lamy, L., B. Cecconi, and P. Zarka (2009). *Cassini/RPWS/HFR LESIA/Kronos SKR Data Collection*. DOI: [10.25935/zkxb-6c84](https://doi.org/10.25935/zkxb-6c84). URL: <https://doi.org/10.25935/zkxb-6c84>.
- Lamy, L., J. Waters, and C. Louis (2023). "Comparative visibility of planetary auroral radio emissions and implications for the search for exoplanets". In: *Planetary, Solar and Heliospheric Radio Emissions IX*. Ed. by G. Fischer et al., in press.
- Lamy, L. et al. (2008a). "Modeling of Saturn kilometric radiation arcs and equatorial shadow zone". In: *Journal of Geophysical Research: Space Physics* 113.A10. DOI: <https://doi.org/10.1029/2008JA013464>. eprint: <https://agupubs.onlinelibrary.wiley.com/doi/pdf/10.1029/2008JA013464>. URL: <https://agupubs.onlinelibrary.wiley.com/doi/abs/10.1029/2008JA013464>.
- Lamy, L. et al. (2008b). "Saturn kilometric radiation: Average and statistical properties". In: *Journal of Geophysical Research: Space Physics* 113.A7. DOI: <https://doi.org/10.1029/2007JA012900>. eprint: <https://agupubs.onlinelibrary.wiley.com/doi/pdf/10.1029/2007JA012900>. URL: <https://agupubs.onlinelibrary.wiley.com/doi/abs/10.1029/2007JA012900>.
- Lamy, L et al. (2009). "An auroral oval at the footprint of Saturn's radiosources, collocated with the UV aurorae". In: *J. Geophys. Res.* 114, A10212.
- Long, Jonathan, Evan Shelhamer, and Trevor Darrell (2015). "Fully convolutional networks for semantic segmentation". In: *2015 IEEE Conference on Computer Vision and Pattern Recognition (CVPR)*, pp. 3431–3440. DOI: [10.1109/CVPR.2015.7298965](https://doi.org/10.1109/CVPR.2015.7298965).
- Morioka, A. et al. (Sept. 2008). "AKR breakup and auroral particle acceleration at substorm onset". In: *Journal of Geophysical Research (Space Physics)* 113.A9, A09213, A09213. DOI: [10.1029/2008JA013322](https://doi.org/10.1029/2008JA013322).

-
- O'Dwyer, E. P. et al. (2023a). *Image-based Classification of Intense Radio Bursts from Spectrograms: An Application to Saturn Kilometric Radiation*. Version 1.0.0. DOI: [10.5281/zenodo.8075625](https://doi.org/10.5281/zenodo.8075625). URL: <https://doi.org/10.5281/zenodo.8075625>.
- O'Dwyer, E. P. et al. (2023b). *Selection of Low Frequency Extensions of Saturn Kilometric Radiation*. URL: https://github.com/elodwyer1/Selection_of_Low_Frequency_Extensions_of_Saturn_Kilometric_Radiation.
- O'Dwyer, E. P. et al. (2023c). *Selection of Low Frequency Extensions of Saturn Kilometric Radiation detected by Cassini/RPWS*. Version 2.0.0. DOI: [10.5281/zenodo.7895766](https://doi.org/10.5281/zenodo.7895766). URL: <https://doi.org/10.5281/zenodo.7895766>.
- O'Dwyer, E. P. et al. (2023d). *Unet Application to Saturn Kilometric Radiation*. URL: https://github.com/elodwyer1/Unet_Application_to_Saturn_Kilometric_Radiation.
- Reed, J. J. et al. (Jan. 2018). "Low-Frequency Extensions of the Saturn Kilometric Radiation as a Proxy for Magnetospheric Dynamics". In: *Journal of Geophysical Research (Space Physics)* 123.1, pp. 443–463. DOI: [10.1002/2017JA024499](https://doi.org/10.1002/2017JA024499).
- Ren, Shaoqing et al. (2015). "Faster r-cnn: Towards real-time object detection with region proposal networks". In: *Advances in neural information processing systems* 28.
- Ronneberger, O., P. Fischer, and T. Brox (May 2015). "U-Net: Convolutional Networks for Biomedical Image Segmentation". In: *arXiv e-prints*, arXiv:1505.04597, arXiv:1505.04597. arXiv: [1505.04597](https://arxiv.org/abs/1505.04597) [cs.CV].
- Wu, CS and LC Lee (1979). "A theory of the terrestrial kilometric radiation". In: *Astrophys. J.* 230, pp. 621–626.